

ผลของเหล็ก วานาเดียม และ ทังสเตน เจือลงในไทเทเนียมต่อการสลายสาร BTEX  
ด้วยปฏิกิริยาโฟโตแคทาไลซิส



นางลักษณา เหล่าเกียรติ

ศูนย์วิทยทรัพยากร  
จุฬาลงกรณ์มหาวิทยาลัย

วิทยานิพนธ์นี้เป็นส่วนหนึ่งของการศึกษาตามหลักสูตรปริญญาวิทยาศาสตรดุษฎีบัณฑิต

สาขาวิชาการจัดการสิ่งแวดล้อม (สหสาขาวิชา)

บัณฑิตวิทยาลัย จุฬาลงกรณ์มหาวิทยาลัย

ปีการศึกษา 2553

ลิขสิทธิ์ของจุฬาลงกรณ์มหาวิทยาลัย

EFFECT OF IRON, VANADIUM, AND TUNGSTEN DOPED TITANIA ON BTEX  
PHOTOCATALYTIC DECOMPOSITION



Mrs. Laksana Laokiat

ศูนย์วิทยทรัพยากร  
จุฬาลงกรณ์มหาวิทยาลัย  
A Dissertation Submitted in Partial Fulfillment of the Requirements  
for the Degree of Doctor of Philosophy Program in Environmental Management

(Interdisciplinary Program)

Graduate School

Chulalongkorn University

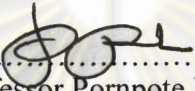
Academic Year 2010

Copyright of Chulalongkorn University

Thesis Title EFFECT OF IRON, VANADIUM, AND TUNGSTEN  
DOPED TITANIA ON BTEX PHOTOCATALYTIC  
DECOMPOSITION  
By Mrs. Laksana Laokiat  
Field of Study Environmental Management  
Thesis Advisor Associate Professor Nurak Grisdanurak, Ph.D.

---


Accepted by the Graduate School, Chulalongkorn University in Partial  
Fulfillment of the Requirements for the Doctoral Degree

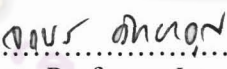
  
..... Dean of the Graduate School  
(Associate Professor Pornpote Piumsomboon, Ph.D.)

THESIS COMMITTEE


  
..... Chairman  
(Assistant Professor Manaskorn Rachakornkij, Ph.D.)

  
..... Thesis Advisor  
(Associate Professor Nurak Grisdanurak, Ph.D.)

  
..... Examiner  
(Associate Professor Jin Anotai, Ph.D.)

  
..... Examiner  
(Associate Professor Jatuporn Wittayakun, Ph.D.)

  
..... Examiner  
(Assistant Professor Pisut Painmanakul, Ph.D.)

  
..... External Examiner  
(Pongtanawat Khemthong, Ph.D.)

ลักษณะ เหล่าเกียรติ: ผลของเหล็ก วานาเดียม และ ทังสเตน เจือลงในไทเทเนียมต่อ  
การสลายสาร BTEX ด้วยปฏิกิริยาโฟโตแคทาไลซิส. (EFFECT OF IRON,  
VANADIUM, AND TUNGSTEN DOPED TITANIA ON BTEX PHOTOCATALYTIC  
DECOMPOSITION) อ. ที่ปรึกษาวิทยานิพนธ์หลัก: รศ.ดร. นุรักษ์ กฤษดานุรักษ์,  
110 หน้า

ไทเทเนียมเจือด้วยเหล็ก วานาเดียม และ ทังสเตน เตรียมด้วยวิธีโซลโกลเจลและ  
เชื่อมลงบนผ้าใยแก้ว เพื่อการสลายสารประกอบอินทรีย์ระเหยง่าย เบนซีน โทลูอิน เอทิลเบน  
ซีน และไซลีน (BTEX) ภายใต้แสงขาว เปรียบเทียบผลการศึกษากับไทเทเนียมทางการค้า (P25)  
พบว่าตัวอย่างที่เตรียมได้ทั้งหมดมีความสามารถในการทำปฏิกิริยาภายใต้แสงขาวได้สูงกว่า  
ไทเทเนียมทางการค้า โดยไทเทเนียมที่เจือด้วยวานาเดียม มีความสามารถสูงสุด ตามด้วยทังสเตน  
และเหล็ก ไทเทเนียมที่เจือด้วยวานาเดียมสามารถสลายไอระเหยของโทลูอินที่ความเข้มข้น  
1163±12 พีพีเอ็ม ได้ถึงร้อยละ 69 และสลายสารผสม BTEX ที่ความเข้มข้น 228±48 พีพีเอ็ม  
ได้สูงสุดร้อยละ 15, 68, 81 และ 84 ตามลำดับ ซึ่งสอดคล้องกับสเปกตรัมของ UV-Vis DRS  
แสดงให้เห็นว่าไทเทเนียมที่เจือด้วยวานาเดียมสามารถดูดซับแสงขาวได้สูงที่สุด ตามด้วย  
ทังสเตน และเหล็ก XRD สเปกตรัมของตัวอย่างทั้งหมด แสดงองค์ประกอบของเฟสอนาเทส  
และรูไทล์ โดยองค์ประกอบส่วนใหญ่ (> 80 %) เป็นเฟสอนาเทส โลหะทรานซิชันถูกผสมอย่าง  
ดีเข้าไปในโครงสร้างของไทเทเนียม XANES สเปกตรัมของ Ti K-edge แสดงว่า ไอออนส่วนมาก  
ของ Ti เป็น  $Ti^{4+}$  มีโครงสร้างเป็นแบบทรงแปดหน้า มีการบิดเบี้ยวของโครงผลึกเพิ่มขึ้นใน  
ตัวอย่างไทเทเนียมที่เจือด้วยเหล็ก วานาเดียม และทังสเตน ผลการศึกษาแสดงให้เห็นว่า ไท  
เทเนียมเจือด้วยเหล็ก วานาเดียม และทังสเตน ประสบความสำเร็จในการสังเคราะห์และวาง  
ลงบนผ้าใยแก้ว มีความเหมาะสมต่อการสลายแก๊สมลพิษอินทรีย์ภายใต้แสงขาว

สาขาวิชา... การจัดการสิ่งแวดล้อม

ปีการศึกษา... 2553

ลายมือชื่อนิสิต

ลายมือชื่อ อ.ที่ปรึกษาวิทยานิพนธ์หลัก

*กฤษดานุรักษ์*

*นุรักษ์*

จุฬาลงกรณ์มหาวิทยาลัย



## 5087813720 : MAJOR ENVIRONMENTAL MANAGEMENT

KEYWORDS : TRANSITION METALS / DOPED  $\text{TiO}_2$  / BTEX / PHOTOCATALYTIC DECOMPOSITION

LAKSANA LAOKIAT: EFFECT OF IRON, VANADIUM, AND TUNGSTEN DOPED TITANIA ON BTEX PHOTOCATALYTIC DECOMPOSITION. ADVISOR: ASSOC. PROF. NURAK GRISDANURAK, Ph.D., 110 pp.

Iron, vanadium, and tungsten doped  $\text{TiO}_2$  were synthesized via the solvothermal technique and immobilized onto fiberglass cloth (FGC). They were used in the photocatalytic decomposition of gaseous volatile organic compounds: benzene, toluene, ethylbenzene and xylene (BTEX) under visible light. The results were compared to that of the commercial pure  $\text{TiO}_2$  (P25). All doped samples exhibited higher visible light catalytic activity than the P25. The V- $\text{TiO}_2$  showed the highest photocatalytic activity followed by the W and Fe doped samples with the highest conversion of 69% for 1163±12 ppm of gaseous toluene and 15, 68, 81, and 84% for 228±48 ppm of mixed BTEX, respectively. The results corresponded to the UV-Vis diffuse reflectance spectra (UV-Vis DRS) revealing that V- $\text{TiO}_2$  had the highest visible light absorption followed by the W and Fe doped samples. The X-ray diffraction (XRD) patterns indicated all doped samples to contain both anatase and rutile phases with majority (> 80%) being anatase. The transition metal (TM) dopants were well mixed into  $\text{TiO}_2$  lattice. The X-ray absorption near-edge structure (XANES) spectra of the Ti K-edge transition indicated that most Ti ions were in the  $\text{Ti}^{4+}$  with octahedral coordination but with increased lattice distortion from TM doped samples. Our results showed that the TM doped  $\text{TiO}_2$  were successfully synthesized and immobilized onto flexible fiberglass cloth suitable for treatment of gaseous organic pollutants under visible light.

Field of Study: Environmental Management

Student's Signature



Academic Year: 2010

Advisor's Signature



## ACKNOWLEDGEMENTS

I would like to thank my thesis advisor, Assoc. Prof. Dr. Nurak Grisdanurak, for his tremendous support and guidance throughout the duration of my graduate studies. His patience and thoughtfulness are remarkable. Without him I would never have made it this far.

Special gratitude goes to all committee members for providing valuable advices and their insightful suggestions. I would like to express my deepest gratitude to Dr. Paiboon Sreearunothai for his time and effort in guiding, editing and giving valuable comments on my manuscript.

The financial support of the Office of the Higher Education Commission, Thailand, and a grant from the National Center of Excellence for Environmental and Hazardous Waste Management (NCE-EHWM) Program, Thailand, are gratefully acknowledged. I wish to thank the Faculty of Public Health, Thammasat University, for granting me the study leave. I also thank Synchrotron Light Research Institute, Thailand, for their assistances of X-ray absorption spectroscopic experiments.

My gratitude goes to all members in Catalysis Laboratory at Department of Chemical Engineering, Thammasat University (Boy, Ple, Tou, Joy, Job, Eddy, Tum, Rat, Som-O, Donut, Puii, Ploy, Kob, Mai, Pond, Prai, Pui, Mathee, and many whose names are too numerous to mention) for their warming relationship, kindness, encouragement, contribution, and for having so much fun together all the time that I was there. I would like to express my sincere gratitude to a special group of graduate student friends (Ake, Champ, Jang, Jeab, Nong, O-por, Year, and Yui) for their friendship and supporting each other. I wish to thank NCE-EHWM program's officers (Jew, Koa, and Pop) for offering the convenience through my graduate studies.

Last, a special thanks to my Mom and Dad, my oldest sister, my husband and beloved daughter for their unconditional love and support, without whom none of this would have been possible.

# CONTENTS

	<b>Page</b>
ABSTRACT (THAI).....	iv
ABSTRACT (ENGLISH).....	v
ACKNOWLEDGEMENTS.....	vi
CONTENTS.....	vii
LIST OF TABLES.....	xii
LIST OF FIGURES.....	xiv
CHAPTER I INTRODUCTION.....	1
1.1 Research rationale.....	1
1.2 Objective.....	3
1.3 Hypotheses.....	3
1.4 Scope of the study.....	3
1.5 Obtained results.....	4
CHAPTER II LITERATURE REVIEW.....	5
2.1 Volatile organic compounds .....	5
2.1.1 Benzene, Toluene, Ethylbenzene, and Xylene (BTEX)....	6
2.1.1.1 Properties of BTEX.....	6
2.1.1.2 Source of BTEX and health risk.....	8
2.1.1.3 BTEX exposure limits.....	10
2.2 Treatment of BTEX gases.....	11
2.3 Heterogeneous photocatalysis.....	12
2.3.1 Basic Principles of Heterogeneous Photocatalysis.....	13

	<b>Page</b>
2.3.2 Titanium Dioxide as Photocatalyst.....	15
2.4 Transition metal-doped TiO <sub>2</sub> .....	16
2.4.1 Synthesis of transition metal-doped TiO <sub>2</sub> .....	17
2.4.2 Properties of transition metal-doped TiO <sub>2</sub> .....	18
2.4.2.1 Optical property.....	18
2.4.2.2 Electronic property.....	21
2.5 Photocatalysis of gas-phase BTEX using TiO <sub>2</sub> .....	23
2.6 Photocatalysis of gas-phase BTEX using transition metals-doped TiO <sub>2</sub> .....	24
2.7 Influence factors in gaseous photocatalysis.....	25
2.7.1 Relative humidity.....	25
2.7.2 Initial concentration.....	26
2.7.3 Flow rate.....	27
CHAPTER III METHODOLOGY.....	29
3.1 Materials and chemicals.....	29
3.1.1 Chemicals and reagents.....	29
3.1.2 Experimental set up.....	29
3.2 Catalyst preparation.....	30
3.3 Catalyst characterization.....	32
3.3.1 Thermal gravimetric analysis and differential thermal analysis (TGA-DTA).....	32
3.3.2 Transmission electron microscope (TEM).....	32
3.3.3 Scanning electron microscope (SEM).....	32



	<b>Page</b>
3.3.4 X-Ray diffraction (XRD).....	33
3.3.5 X-ray absorption near edge structure (XANES).....	33
3.3.6 UV–vis diffuse reflectance spectroscopy (UV- DRS) and Band Gap Measurement.....	34
3.3.7 Photoluminescence spectrometer (PL).....	34
3.4 Photocatalytic testing.....	35
3.4.1 BTEX calibration.....	36
3.4.2 Reliability testing.....	37
CHAPTER IV RESULTS AND DISCUSSION.....	39
4.1 Catalyst characterization.....	39
4.1.1 Fe-TiO <sub>2</sub> (Fe/Ti mole ratio = 1).....	39
4.1.1.1 TGA-DTA.....	39
4.1.1.2 XRD.....	40
4.1.1.3 Surface area by N <sub>2</sub> adsorption-desorption isotherms.....	43
4.1.1.4 SEM.....	44
4.1.1.5 UV-DR spectra.....	46
4.1.2 Fe, V, and W-doped TiO <sub>2</sub> (M/Ti mole ratio = 0.1).....	48
4.1.2.1 TEM.....	48
4.1.2.2 SEM.....	50
4.1.2.3 X-Ray Diffraction.....	51
4.1.2.4 XANES.....	53
4.1.2.5 UV–DRS and band gap measurement.....	57

	<b>Page</b>
4.1.2.6 PL.....	59
4.2 Photocatalytic testing.....	60
4.2.1 Catalyst screening.....	60
4.2.2 Effect of W dopant on photodegradation of BTEX.....	61
4.2.2.1 Effect of flow rate.....	63
4.2.2.2 Effect of catalyst loading.....	64
4.2.2.3 Effect of initial concentration.....	66
4.2.2.4 Effect on relative humidity.....	67
4.2.3 Effect of V dopant on photodegradation of BTEX.....	68
4.2.3.1 Degradation of BTEX single compound.....	68
4.2.3.2 Degradation of mixed BTEX .....	69
4.2.3.3 Effect of initial concentration.....	72
4.2.3.4 Effect of relative humidity.....	73
4.2.3.5 Reliability of V-TiO <sub>2</sub> .....	76
4.3 Current.....	81
CHAPTER V CONCLUSSION AND RECOMMEDATIONS.....	84
5.1 Conclusions.....	84
5.2 Recommendations for future study.....	85
REFERENCES.....	87
APPENDICES.....	98
APPENDIX A.....	99

	<b>Page</b>
APPENDIX B.....	101
APPENDIX C.....	103
APPENDIX D.....	106
BIOGRAPHY.....	110



ศูนย์วิทยทรัพยากร  
จุฬาลงกรณ์มหาวิทยาลัย

## LIST OF TABLES

<b>Table</b>		<b>Page</b>
2.1	Physio-chemical properties of BTEX.....	8
2.2	Toxicity values of BTEX.....	10
2.3	Atomic and ionic radius of Fe, V, and W.....	17
2.4	Standard reduction potential of Fe <sup>3+</sup> , V <sup>5+</sup> , and W <sup>6+</sup> .....	20
3.1	GC retention time of BTEX.....	35
3.2	Liner equation and R <sup>2</sup> of each BTEX.....	37
4.1	Structure characteristics obtained by XRD, BET and SEM analyses..	43
4.2	Band edge wavelength and energy bandgap of materials.....	48
4.3	Crystallite sizes and the anatase and rutile percentage of the catalysts.....	52
4.4	Relative composition of A <sub>1</sub> , A <sub>2</sub> , and A <sub>3</sub> for TiO <sub>2</sub> (P25), Fe-TiO <sub>2</sub> , V-TiO <sub>2</sub> , and W-TiO <sub>2</sub> .....	56
4.5	Band-gap energy and absorption edge wavelength of the catalysts....	57
4.6	Comparison on efficiency rate of BTEX removal over W-TiO <sub>2</sub> and TiO <sub>2</sub> (P25) immobilized on FGC.....	62
4.7	Effect of flow rate on the reaction rate of BTEX removal over W-TiO <sub>2</sub> immobilized on FGC.....	64
4.8	Effect of flow rate on the reaction rate of BTEX removal over W-TiO <sub>2</sub> immobilized on FGC.....	65
4.9	Effect of relative humidity on the reaction rate of BTEX removal over W-TiO <sub>2</sub> immobilized on FGC.....	68
4.10	BTEX degradation on various photocatalytic oxidation processes.....	71
4.11	Percent removal efficiency of mixed BTEX gases using V-TiO <sub>2</sub> under different condition.....	72

<b>Table</b>	<b>Page</b>	
4.12	Percent removal of mixed BTEX gases using the regenerated V-TiO <sub>2</sub> and percent variation of each cycle.....	79
4.13	Electrical energy per orde rreported for the current.....	83
D.1	Degradation of gaseous toluene for each catalyst-coated FGC after 120 minutes of visible light irradiation.....	106
D.2	Degradation of each BTEX gas by the V-doped TiO <sub>2</sub> after 120 minutes of visible light irradiation.....	106
D.3	Degradation of mixed BTEX gases by V-TiO <sub>2</sub> , TiO <sub>2</sub> (P25) and uncoated FGC.....	107
D.4	Degradation of mixed BTEX gases by V-TiO <sub>2</sub> under 30-40% RH...	108
D.5	Degradation of mixed BTEX gases by V-TiO <sub>2</sub> under 70-80% RH...	109



## LIST OF FIGURES

Figure		Page
2.1	Structure of BTEX.....	7
2.2	Schematic photocatalytic processes over photon activated semiconductor cluster (p) photogeneration of electron/hole pair, (q) surface recombination, (r) recombination in the bulk, (s) diffusion of acceptor and reduction on the surface of SC, and (t) oxidation of donor on the surface of SC particle.....	15
2.3	Energy difference reduced due to metal ion dopants: $h\nu_1$ : pure $\text{TiO}_2$ ; $h\nu_2$ : metal-doped $\text{TiO}_2$ .....	19
2.4	Energy levels for various semiconductors.....	21
2.5	Molecular orbital energy level diagram of the lowest unoccupied of $\text{TiO}_6$ with $O_h$ , $D_{2d}$ and $D_{2h}$ .....	22
3.1	Schematic diagram of the set up used for photocatalytic degradation test of the BTEX gases by the prepared catalyst-coated FGC.....	30
3.2	Preparation of M-Ti molar ratio by solvothermal method.....	31
3.3	Calibration graph of peak area versus concentration for BTEX..	37
3.4	Reliability set up test.....	38
4.1	TGA - DTA curves of the as-synthesized (dried) $\text{Fe-TiO}_2$ sample.....	40
4.2	XRD pattern of $\text{TiO}_2$ P25 and $\text{Fe-TiO}_2$ prepared by the solvothermal method calcined at temperatures between 300-700°C.....	41
4.3	Effect of calcination temperature on average crystalline size of $\text{Fe-TiO}_2$ prepared by solvothermal technique and calcined for 3 hours.....	42

<b>Figure</b>	<b>Page</b>
4.4 Effect of calcination time on nanocrystalline anatase phase of Fe-TiO <sub>2</sub> calcined at 3 and 8 hours.....	42
4.5 N <sub>2</sub> adsorption and desorption isotherm of commercial TiO <sub>2</sub> P25 and Fe-TiO <sub>2</sub> calcined at 500°C and 650°C.....	44
4.6 SEM images of Fe-TiO <sub>2</sub> calcined at (a) 500°C, (b) 650°C and (c) 700°C.....	45
4.7 SEM and elemental mapping of Fe-TiO <sub>2</sub> calcined at 500°C.....	46
4.8 UV-DR spectra of TiO <sub>2</sub> P25 and Fe-TiO <sub>2</sub> at different calcination temperatures.....	47
4.9 TEM images of catalysts: (a) Fe-TiO <sub>2</sub> , (b) V-TiO <sub>2</sub> and (c) W-TiO <sub>2</sub> .....	49
4.10 SEM image of pristine fiberglass cloth.....	50
4.11 SEM images of catalysts immobilized onto FGC: (a) TiO <sub>2</sub> P25, (b) Fe-TiO <sub>2</sub> , (c) V-TiO <sub>2</sub> and (d) W-TiO <sub>2</sub> .....	50
4.12 XRD patterns (from bottom to top) of the FGC substrate, W-doped, V-doped, Fe-doped and pure TiO <sub>2</sub> (P25) immobilized on FGC. Peaks corresponding to the anatase and rutile phases of TiO <sub>2</sub> are marked by the solid diamond and open circle respectively. The top insert plots the dominant anatase and rutile peaks from all samples on the same scale showing the V- and W-doped sample peaks to shift slightly to higher angles, while the Fe-doped sample peaks shift minimally to lower angles with respect to their corresponding peak positions in the pure TiO <sub>2</sub> (P25) sample.....	52

<b>Figure</b>	<b>Page</b>
4.13 (a) XANES spectra of the Ti <i>K</i> -edge in the prepared catalysts compared to those of the reference rutile and anatase TiO <sub>2</sub> , (b) Close-up of the pre-edge region in (a) overlaid on the same scale to depict changes in the pre-edge intensity. From top to bottom (indicated also by a guiding arrow): W-doped, V-doped, P25, Fe-doped, anatase and rutile TiO <sub>2</sub> .....	54
4.14 The pre-edge XANES spectra of Ti species in the photocatalyst samples (a) V-TiO <sub>2</sub> and (b) TiO <sub>2</sub> (P25). The insert plots Gaussian–Lorentzian curve fitting of (a) and (b).....	56
4.15 (a) UV-Vis DRS spectra of the prepared catalyst-coated FGC samples and (b) the Kubelka-Munk transformation of (a) in order to obtain band-gap energies of the prepared catalyst.....	58
4.16 Photoluminance spectra of pureTiO <sub>2</sub> and V-TiO <sub>2</sub> .....	59
4.17 Percent removal efficiency of gaseous toluene for each catalyst-coated FGC. After 120 minutes of visible light irradiation, the V-doped TiO <sub>2</sub> displayed the highest removal efficiency followed by the W-, Fe- and pure TiO <sub>2</sub> .....	60
4.18 Variation of the % BTEX removal with irradiation time using TiO <sub>2</sub> (P25) and W-TiO <sub>2</sub> . Conditions: 30% RH, flow rate 60 ml/min, catalysts loading 0.1 mg/cm <sup>2</sup> , day light lamp fluorescent 18 watt.....	62
4.19 Effect of flow rate on the % BTEX removal with irradiation time using W-TiO <sub>2</sub> immobilized on FCG. Conditions: 30% RH, catalysts loading 0.1 mg/cm <sup>2</sup> , day light lamp fluorescent 18 watt. Initial concentration: benzene = 86 ppm , toluene = 156 ppm, ethylbenzene = 168 ppm, <i>o</i> -xylene = 212 ppm.....	63

<b>Figure</b>	<b>Page</b>	
4.20	Effect of catalyst loading on % BTEX removal with irradiation time over W-TiO <sub>2</sub> . Conditions: 30% RH, flow rate 60 ml/min, day light lamp fluorescent 18 watt. Initial concentration: benzene = 76 ppm , toluene = 156 ppm, ethylbenzene = 175 ppm, <i>o</i> -xylene = 220 ppm.....	65
4.21	Effect of initial concentration on the % BTEX removal with irradiation time over W-TiO <sub>2</sub> catalyst. Conditions: 30% RH, flow rate 90 ml/min, catalysts loading 0.1 mg/cm <sup>2</sup> , day light lamp fluorescent 18 watt.....	66
4.22	Variation of the % BTEX removal with irradiation time using TiO <sub>2</sub> (P25) and W-TiO <sub>2</sub> . Conditions: Flow rate 90 ml/min, catalysts loading 0.1 mg/cm <sup>2</sup> , day light lamp fluorescent 18 watt. Initial concentration: benzene = 500 ppm , toluene = 760 ppm, ethylbenzene = 755 ppm, <i>o</i> -xylene = 900 ppm.....	67
4.23	Percent removal efficiency of each BTEX gas by the V-doped TiO <sub>2</sub> . From the lowest removal efficiency to the highest: benzene, toluene, ethylbenzene, and <i>o</i> -xylene.....	69
4.24	Percent removal efficiency of mixed BTEX gases by V-TiO <sub>2</sub> , TiO <sub>2</sub> (P25) and uncoated FGC.....	70
4.25	Percent removal efficiency of low and high concentration mixed BTEX by the V-TiO <sub>2</sub> under (a) 30-40 %RH and (b) 70-80 %RH. ....	74
4.26	Proposed mechanism of BTEX decomposition over V-TiO <sub>2</sub> photocatalyst under visible light irradiation.....	75
4.27	Performance of reused catalysts for single BTEX in feed.....	77
4.28	Performance of reused catalysts for mixed BTEX in feed.....	78
4.29	Fresh and spent catalyst supports.....	80

Figure		Page
4.30	Involved current under different chemicals.....	82
B.1	K-edge XANES spectra of Fe-TiO <sub>2</sub> .....	102
B.2	K-edge XANES spectra of V-TiO <sub>2</sub> .....	102
C.1	Drawing of reactor vessel.....	103
C.2	Reactor set up in laboratory.....	104
C.3	Saturators for preparation of BTEX vapor.....	104
C.4	Gas chromatograph (GC 14A, Shimadzu Co. Ltd.).....	105
C.5	Chromatogram of mixed BTEX; B: benzene, T: toluene, E: ethylbenzene, X: <i>o</i> -xylene.....	105



ศูนย์วิทยทรัพยากร  
จุฬาลงกรณ์มหาวิทยาลัย



# CHAPTER I

## INTRODUCTION

### 1.1 Research rationale

Normally, people spend most of their time indoor such as home, office, car and shopping center. This makes the indoor environment important when addressing health risks and exposures to air pollution. Volatile organic compounds (VOCs) are well-known as one of the major components of indoor air contaminants. Many VOCs are toxic, and some are considered carcinogenic, mutagenic, or teratogenic. BTEX (benzene, toluene, ethylbenzene and xylene) are the major group of VOCs found in indoor environments in different countries. It emitted from different sources such as combustion by-products, cooking, construction materials, office equipment, and consumer products. Exposure to BTEX can result in both acute and chronic health effects. Moreover, the most significant problem related to the emission of these pollutants through environment is the possible production of photochemical oxidants as ozone.

Hence, BTEX can threaten human health and cause environmental problems; it has stimulated interests worldwide to treat BTEX especially at points of generation prior to its emission into environment. Various methods have been investigated for controlling BTEX such as adsorption, condensation, thermal decomposition, catalytic incineration, biofiltration and photocatalytic oxidation (Collins, Laturus, and Nepovim, 2002). Among these methods, photocatalytic oxidation using  $\text{TiO}_2$  seems to have the greatest potential especially in the field of air treatment at low temperature. It is rapid, energy efficient and effective for destruction of wide range of organic air pollutants (Anchez et al., 2006; Dong et al., 2007). However,  $\text{TiO}_2$  exhibits high catalytic activity only under UV light with energy larger than the  $\text{TiO}_2$  band-gap energy (~3.0-3.2 eV) and thus renders it less useful for air treatment under natural light (Fujishima and Zhang, 2006).

In order to improve the photocatalytic activity and the response to the visible region, doping of  $\text{TiO}_2$  with metal and non-metal were proposed (Chatterjee and Dasgupta, 2005; Ohno et al., 2004). Transition metals (TM) such as Cr, Mn, Fe, Co,

Cu and Ni have been employed as dopants (Carp, Huisman, and Reller, 2004). Among numerous transition metals Fe, V, and W are chosen for this study because of their similar ionic radii to that of the Ti cation and are thus likely to be well dispersed into TiO<sub>2</sub> matrix without phase segregation. This should result in more effective enhancement of visible light absorption and photocatalytic activity than when metal dopant oxides are phase separated from the TiO<sub>2</sub>. However, the photocatalytic activity of TM-doped TiO<sub>2</sub> depends on several factors such as dopant concentration, location and distribution of dopants and their electronic configurations (Anpo et al., 2005).

TiO<sub>2</sub> in powder form is perhaps, the most common form of TiO<sub>2</sub> catalysts. However, its utilization can be quite cumbersome unless the catalysts are immobilized onto suitable substrates so that they can be easily handled and recovered after pollutant treatment. Various types of materials including activated carbon filter (Ao and Lee, 2003) nonwoven textile (Ku, Ma, and Shen, 2001) as well as cotton fabrics (Dong et al., 2006) have been developed for the immobilization of TiO<sub>2</sub> photocatalysts since substrate materials have been shown to influence activity of catalysts (Soriano et al., 2000). Fiberglass cloth (FGC) is a promising material for use as a support of catalysts especially for treatment of gaseous pollutants because of its resistance to photocatalytic decomposition by the TiO<sub>2</sub>, high mechanical strength, good flexibility, environmentally friendly, high temperature and fire resistance suitable for industrial processes. Currently, few literatures have reported the use of the flexible, fire-resistant FGC as substrate material for TiO<sub>2</sub> (Horikoshi et al., 2002) especially for photocatalytic treatment of air pollutants under visible light.

The present study aims to investigate the feasibility of applying Fe, V, and W-doped TiO<sub>2</sub> to treat gaseous BTEX under visible light. The Fe, V, and W were introduced into TiO<sub>2</sub> using solvothermal method. The resulting powders were then immobilized onto FGC. Samples were characterized using Thermal gravimetric analysis and Differential Thermal analysis (TGA-DTA), X-ray diffractometer (XRD), transmission electron microscope (TEM), scanning electron microscope (SEM), UV-vis diffuse reflectance spectroscope (UV-DRS), photoluminescence spectrometer (PL), and X-ray absorption near-edge structure (XANES) to obtain information on phase components, particle and crystallite sizes, optical absorption, and oxidation state and local geometry of the Ti atoms, respectively. The tests on the prepared catalyst-coated FGC using a home-made reactor equipped with daylight fluorescent

bulb showed successfully a high removal efficiency of gaseous BTEX, results of which were discussed.

## 1.2 Objective

This study aims to investigate the effect of transition metals doped TiO<sub>2</sub> based catalysts on the degradation of BTEX contaminated in air. Studied transition metals of Fe, V, and W are focused. The specific objectives of this study are:

1. To understand the relevance of transition metals on physico-chemical properties of obtained Fe, V, and W doped TiO<sub>2</sub> based catalysts via a solvothermal method.
2. To determine a suitable catalyst for the degradation of BTEX contaminated in air. The study is based on the highest degradation rate under following considerations; contaminated air concentration and relative humidity.
3. To test the reliability of selected catalyst.

## 1.3 Hypotheses

The hypotheses of this study are that Fe, V, and W can be used to enhance the light adsorption property of titanium dioxide. In addition, the photocatalytic activity of transition metal-doped TiO<sub>2</sub> can effectively decompose volatile organic compounds with a higher activity compared to commercial TiO<sub>2</sub>.

## 1.4 Scope of the study

All experiments in this research were conducted in the laboratory scale. The scopes of research are as follows:

1. Fe, V and W doped TiO<sub>2</sub> were prepared in the form of powder using the solvothermal method and then immobilized onto glass fiber cloth.
2. Various techniques include TGA-DTA, TEM, SEM, XRD, UV-DRS, PL, and XANES were used for the characterization of catalysts.
3. Photocatalytic degradation of gas-phase BTEX were carried out using Day light lamp with peak wavelength greater than 400 nm, under atmospheric pressure and at room temperature.

4. The degradation were set up and simulated by fiber glass cloth immobilized catalysts with studied parameters of relative humidity, initial contaminated air concentration, and flow rate.

### 1.5 Obtained results

This research provides valuable information on the synthesis of Fe, V and W doped  $\text{TiO}_2$  and its application. The synthesized catalysts could be activated by visible light. These visible light activated  $\text{TiO}_2$  are very useful photocatalyst. It can be immobilized onto flexible fiber glass cloth suitable for treatment of gaseous organic pollutants (BTEX). In addition, the knowledge on physico-chemical properties of synthesized catalysts can serve as a concrete suggestion for further improvement.



## CHAPTER II

### LITERATURE REVIEW

The applications to environmental cleanup have been one of the most active areas in heterogeneous photocatalysis, especially for the destruction of organic compounds in polluted air and wastewater. However, studies involving gas-phase heterogeneous photocatalysis are relatively few in number compared with the literature on photocatalytic water treatment. In this chapter, the development of TiO<sub>2</sub> used as photocatalyst in the abatement of air pollution will be presented, starting from the last ten year research on heterogeneous photocatalysis using TiO<sub>2</sub> to the current research conducted in the area. The review emphasize on the Volatile Organic compounds (VOCs) involved, the form of the catalyst (pure TiO<sub>2</sub> and transition metal doped-TiO<sub>2</sub>) used in the heterogeneous photocatalysis, the important properties of metal doped-TiO<sub>2</sub>, and the influence of operational conditions.

#### 2.1 Volatile organic compounds

VOCs include a wide range of substances which evaporate rapidly or are gases at room temperature and pressure. In a given environment, the concentration of individual VOCs will be very variable and depend upon the presence or absence of potential emission source. Emission of VOCs also contributed to localized pollution problems of toxicity and odour. The most significant problem related to VOCs is the production of photochemical oxidants, for example, ozone and peroxyacetyl nitrate (PANs).

Thailand is facing serious air pollution problem related to VOCs due to industrialization. Map Ta Phut Industrial Estate is the origin of Thailand's petrochemical industries. It serves as the upstream industrial estate for many petrochemical-related industries. In 1997, this area was a well known environmental problem related to VOCs. There are various reports and claims regarding occurrence of fruit like smell around the estate. According to the record of Pollution Control Department (PCD) 40% of environmental complains are considered to be related to VOCs. There are some preliminary studies of VOC from the emissions at Map Ta



Phut to detect VOC species and assess ambient concentration levels. Fourteen species of VOCs were detected, and benzene, toluene and xylene were reported in range of 1.4-3.5, 0-22 and 0.8-20  $\mu\text{g m}^{-3}$ , respectively (New Energy and Industrial Development Organization, 1999). In 2009, the Office of Natural Resources and Environment Policy and Planning reported that forty species of VOCs were detected in this area. Twenty of them were classified as carcinogenic substances and nineteen of this group their concentrations were greater than standard.

The presence of VOCs in ambient and indoor air is widely recognized as precursors of serious risk to human health. Many studies have shown that printing processes lead to indoor emissions of VOCs (Zuraimi, Tham, and Sekhar, 2003). The concentration of four VOCs namely BTEX in a large printing facility located in Bangkok, Thailand were collected and analyzed at the working place (Thanacharoenchanaphas et al., 2007). The concentration ranges of BTEX were 10-200 ppm which is exceeded the recommended maximum level of 5 ppm set by the American Conference of Governmental Industrial Hygienists (ACGIH) as well as the Ministry of Interior, Thailand.

All VOCs are important because of their impact on human health and the environment but BTEX compounds are seen as the most harmful of these species. The most common source of exposure to BTEX is from breathing contaminated air, particularly in area of heavy traffic because BTEX can be released from vehicle. Therefore, people can expose to BTEX compounds in the ambient (outdoor) air, at work and in the home. People live in urban areas (cities) or by major roads and highways will likely be exposed to more BTEX than someone who lives in a rural area.

### **2.1.1 Benzene, Toluene, Ethylbenzene, and Xylene**

BTEX is an acronym for benzene, toluene, ethylbenzene, and xylene. This group of VOCs may come from both biogenic and anthropogenic sources. Anthropogenic sources include wastewater treatment plants, vehicle emissions and fuel production and consumption. The BTEX compounds are important family of organo-pollutants which are components of gasoline and aviation fuels and are widely used in industrial processes. Therefore, in this research the VOCs concerned are

benzene, toluene, ethylbenzene and xylene (*o*-xylene is representative). As these substances pose very serious health effects, the Environmental Protection Agency (EPA) of most countries considers all of these compounds priority pollutants.

### 2.1.1.1 Properties of BTEX

The monoaromatic hydrocarbons, abbreviated BTEX, are aromatic hydrocarbons containing one unsubstituted or methyl-substituted benzene ring, their structure as shown in Figure 2.1

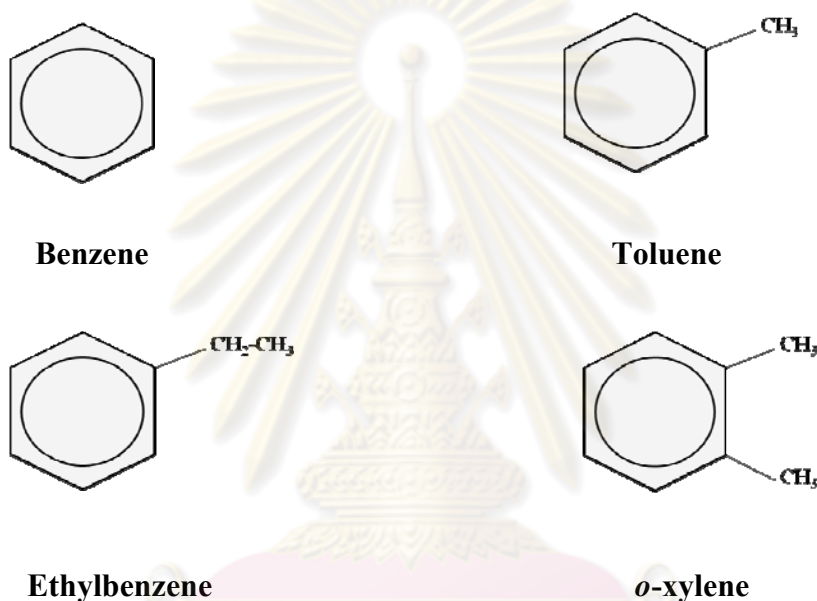


**Figure 2.1** Structure of BTEX.

Once released to the environment, BTEX can volatilize, dissolve, attach to soil particles or degrade. Volatilization occurs when chemicals evaporate, allowing them to move from a liquid into the air. Due to their physio-chemical properties as shown in Table 2.1, BTEX can evaporate into air very quickly and result in widespread emissions to the environment. Exposure to BTEX from water contributes only a small percentage of the total daily intake, compared with inhaled air and dietary sources (WHO, 2008).

**Table 2.1** Physio-chemical properties of BTEX (NIST, 2010: online).

property	Compound			
	Benzene	Toluene	Ethylbenzene	<i>o</i> -xylene
Mole weight (g mole <sup>-1</sup> )	78	92	106	106
Density (g ml <sup>-1</sup> )	0.88	0.87	0.87	0.88
Boiling point (°C)	80.1	110.8	136.2	144.4
Water solubility (mg l <sup>-1</sup> )	1780	535	152	175
Vapor pressure (mmHg)	76	22	7	5
Ionization Potential (eV)	9.24 ± 0.00007	8.82 ± 0.001	8.77 ± 0.01	8.56 ± 0.04

### 2.1.1.2 Source of BTEX and health risk

Benzene is a clear, colorless liquid with a sweet aromatic odor. It is the parent compound of all aromatic substances. Benzene is classified as a "known" human carcinogen (Category A) for all routes of exposure based upon convincing human evidence as well as supporting evidence from animal studies. Exposure to benzene can cause acute nonlymphocytic leukemia, acute myeloid leukemia, and also may cause chronic nonlymphocytic and chronic lymphocytic leukemia. (ATSDR, 2007; IRIS, 2010). Exposure to benzene over a period of 14 days can cause acute health effects, such as headache, dizziness and skin, eye and lung irritation; over a period longer than 365 days, the effects are chronic, and these include cancer, leukaemia, aplitic anaemia and reproductive problems in women (Zhang, Eastmond, and Stmith, 2002). Although, there is no specific air quality goal for benzene it is widely accepted that exposed to benzene should be minimized.

Toluene is a clear, colorless liquid with a sweet benzene-like odor. Toluene occurs naturally in crude oil. It is used in aviation gasoline, solvent for

paints, fingernail polish, adhesive, lacquer, and in some printing and leather tanning processes. Although the primary sources of toluene emissions are crude petroleum and natural gas extraction, petroleum refining and household furniture manufacturing facilities, it is also emitted from tobacco smoke. Toluene cannot be classified as a carcinogen because of inadequate evidence (Class D) (EPA 2005b). Toluene affects the nervous system and high levels of toluene may affect the kidneys. The US EPA has established a reference concentration of 162 ppb for toluene based on neurological effects in humans and has set a limit of  $3 \times 10^{-4}$  ppm in drinking water (ATSDR, 2000). The inhalation of this concentration or less, over a lifetime, would not likely result in the occurrence of chronic non-cancer effects.

Ethylbenzene is naturally found in coal tar and petroleum and is also found in manufactured products such as inks, pesticides, and paints. It is used as a precursor in the manufacture of styrene. Solvent grade xylene is nearly always contaminated with a few percent of ethylbenzene. EPA has determined that ethylbenzene is not classifiable as human carcinogen (Class D), while the International Agency for Research on Cancer (IARC) has classified ethylbenzene as possibly carcinogenic to humans, based on sufficient evidence in animal studies (IARC, 2000). An increased incidence of lung adenomas in males and of liver adenomas in females was observed in an inhalation study on mice. The Occupational Health and Safety Administration (OSHA) has set the exposure limit to an average of 100 ppm for an 8-hour workday, or 40-hour workweek.

Xylene has three different isomers, meta-, ortho- and para-xylene. The combination of these forms is called xylenes. Xylene occurs naturally in petroleum and coal tar and is formed during forest fires. Chemical industries produce xylene from petroleum. It is used as solvent in the printing, rubber and leather industries. It is also used as a cleaning agent, a thinner for paint, and in paint and varnishes. Xylenes have not been classified as carcinogens because of inadequate evidence (Class D) (ATSDR, 2007c), while the International Agency for Research on Cancer (IARC) has classified xylene as possibly carcinogenic to humans, based on sufficient evidence in animal studies (IARC, 2000). Xylene affects the brain, however, human and animal studies have not shown xylene to be carcinogenic, but these studies are not conclusive. The US EPA has set a limit of 10 ppm of xylene in drinking water and an

exposure limit of 100 ppm in the workplace air. An exposure of 900 ppm of xylene can cause permanent health problems or death (ATSDR, 2007).

In conclusion, People can expose to BTEX by inhalation, ingestion, and dermal contact. However, significant exposure to these compounds emitted into the air only occurs through the inhalation pathway (Cal/EPA, 2003). Chronic exposure or acute exposure can produce long-term effects, cognitive, and neurobehavioral effects. The toxicity of BTEX is summarized in Table 2.2.

**Table 2.2** Toxicity values of BTEX (Cal/EPA, 2005).

<b>Compound</b>	<b>RELs (<math>\mu\text{g}/\text{m}^3</math>)</b>	<b>Cancer Unit Risk Factors (<math>\mu\text{g}/\text{m}^3</math>)<sup>-1</sup></b>	<b>USEPA Class</b>
Benzene	60	$2.9 \times 10^{-5}$	A
Toluene	300	-	D
Ethylbenzene	2000	-	D
Xylene	700	-	D

RELs = Chronic Inhalation Reference Exposure Levels

### 2.1.1.3 BTEX exposure limits

The Occupational Health and Safety Act for Thailand, has set occupational exposure limits for benzene, toluene, ethylbenzene and xylene in the workplace (Ministry of Interior Notification, No.103, March 16, 1972). The effects of hazardous chemicals on human health due to exposure differ depending on the nature of the substance and exposure period. Therefore, there are different categories of threshold limit values (TLVs). TLV-TWA, the long-term exposure limit (8-hour time weighted average) is intended to control and restrict the total intake by inhalation over one or more working shifts. TLV-STEL, the short-term exposure limit (over 10-15 minutes) may be applied to substances where effects may be seen after brief exposure which has occurred once or repeatedly. TLV-C, the ceiling limit is the amount of chemical that should not be exceeded at any time



The ceiling limits and the short-term exposure limits are set only for benzene and toluene. TLV-C is 25 ppm for benzene and 300 ppm for toluene. TLV-STEL is 50 and 500 ppm for benzene and toluene, respectively. TLV-TWA for benzene, toluene, and xylene are 10, 200 and 100 ppm, respectively. Xylene only has a long-term control limit and there is no exposure limit for ethylbenzene.

## **2.2 Treatment of BTEX gases**

In general, there are three technologies that are most commonly used to treat VOCs in air emissions including BTEX. These technologies are thermal oxidation, carbon adsorption, and catalytic oxidation.

Thermal oxidation equipment is used for destroying contaminants in the exhaust gas from air strippers. Thermal oxidation units are typically single chamber, refractory-lined oxidizers equipped with a propane or natural gas burner and a stack. Lightweight ceramic blanket refractory is used because many of these units are mounted on skids or trailers. Thermal oxidizers are often equipped with heat exchangers where combustion gas is used to preheat the incoming contaminated gas. Operating temperatures range from 760 to 900 °C, and gas residence times are typically 1 second or less. Like catalytic oxidation, thermal oxidation of halogenated VOCs produces acid vapor. Off gas scrubbing may be needed to control the acid vapor.

Carbon adsorption is a remediation technology in which pollutants are removed from air by physical adsorption onto the carbon grain. Carbon is "activated" for this purpose by processing the carbon to create porous particles with a large internal surface area that attracts and adsorbs organic molecules as well as certain metal and other inorganic molecules. Commercial grades of activated carbon are available for specific use in vapor-phase applications. The granular form of activated carbon is typically used in packed beds through which the contaminated air flows until the concentration of contaminants in the effluent from the carbon bed exceeds an acceptable level. Granular activated carbon systems typically consist of one or more vessels filled with carbon connected in series and/or parallel operating under atmospheric, negative, or positive pressure. The carbon can then be regenerated in



place, regenerated at an off-site regeneration facility, or disposed of, depending upon economic considerations.

Catalytic oxidation is a relatively new alternative for the treatment of VOCs. They are effectively controlling VOCs emissions in a wide range of industries. The systems have been applied to both continuous and batch processes and to small and large operations. As its name suggests catalytic oxidation uses a catalyst, a substance that accelerates the rate of a chemical reaction without itself being consumed. Catalytic systems used to oxidize VOCs typically use metal oxides such as nickel oxide, copper oxide, manganese dioxide, or chromium oxide. Noble metals such as platinum and palladium may also be used. Catalysts that resist damage from halogenated VOC combustion are available, but cost more than catalysts that are suitable for nonhalogenated VOC combustion.

In summary, traditional pollution control methods such as adsorption by activated carbon merely transfer pollutants from the gaseous phase to the solid phase; thermally catalytic oxidation requires high temperatures for efficient operation and hence is expensive. These technologies are commonly used for controlling VOCs but they cannot be applied for some situations such as small size treatment and the low heat irradiation control area. Since indoor air quality (IAQ) has become an important community concern due to the increased amount of personal time spent in indoor environments, the method that is the most feasible option to improve indoor air quality has to be proposed. Photocatalytic oxidation (Zhao and Yang, 2003; Carp et al., 2004) is a promising technology for air purification. Photodegradation usually occurs at room temperature and pressure for air purification and may be more cost effective than other conventional techniques. The details of this technology for the removal of BTEX are presented in section 2.3.

### **2.3 Heterogeneous photocatalysis**

Heterogeneous photocatalysis is an emerging technique valuable for water and air purification and remediation. The starting point of a new era in heterogeneous photocatalysis was discovered by Fujishima and Honda in the early 1970's. After that it was soon applied for environmental remediation. Heterogeneous photocatalysis

technique is photocatalysis using semiconductors such as titanium dioxide and ultraviolet light. A sequence of events can lead to oxidation of organic (or inorganic) compounds present in water or air that is in contact with the catalyst.

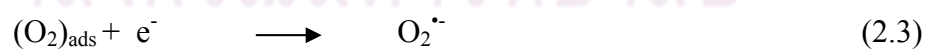
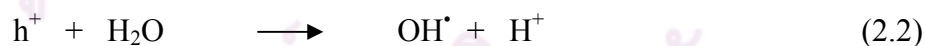
### 2.3.1 Basic principles of heterogeneous photocatalysis

The basis of heterogeneous photocatalysis is the photo-excitation of a semiconductor (SC) solid as a result of absorption of electromagnetic radiation, often, but not exclusively, in the near ultraviolet spectrum. The excess energy that is greater than the band gap energy of this excited electron promoted the electron to the conduction band of semiconductor therefore creating the negative-electron ( $e^-$ ) and positive-hole ( $h^+$ ) pair. This stage is referred as the semiconductor's "photo-excitation" state (Equation 2.1).

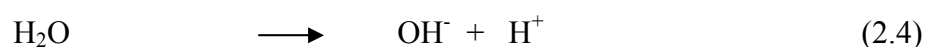


Thus, electron and hole pair ( $e^-h^+$ ) are generated and migrate to semiconductor surface. The following chain reactions have been widely postulated (Gaya and Abdullah, 2008).

The formation of hydroxyl radicals and superoxide ions: the holes in Equation 2.1 can oxidize water molecule resulting in the formation of hydroxyl radicals. The molecular oxygen acts as an acceptor species in the electron-transfer reaction.



Ionization of water: the given water dissociate into ions.



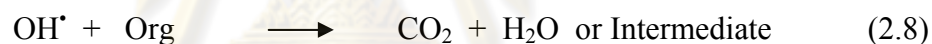
Protonation of superoxides: super-oxide anions (Equation 2.3) can subsequently be involved in the following reaction.



The hydroperoxy radical formed in Equation 2.5 also has scavenging property as  $\text{O}_2$  thus, doubly prolonging the lifetime of photohole:



Photodecomposition of adsorbed molecules on semiconductor's surface: hydroxyl radicals can easily oxidize any organic species (Org) into carbon dioxide and water or other mineral acids.



The recombination between electron and hole occurs unless oxygen is available to scavenge the electrons to form superoxides ( $\text{O}_2^{\cdot-}$ ), its protonated form the hydroperoxyl radical ( $\text{HOO}^{\cdot}$ ) and subsequently  $\text{H}_2\text{O}_2$ . The reaction both oxidation and reduction can take place at the surface of the semiconductor photocatalyst as shown in Figure 2.2.

ศูนย์วิทยทรัพยากร  
จุฬาลงกรณ์มหาวิทยาลัย

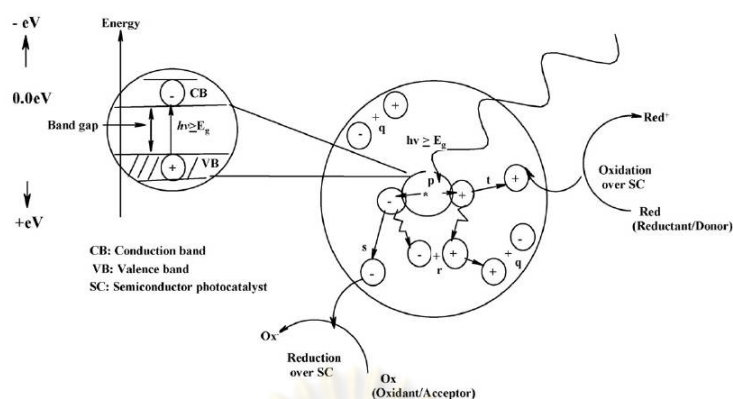


**Figure 2.2** Schematic photocatalytic processes over photon activated semiconductor cluster (p) photogeneration of electron/hole pair, (q) surface recombination, (r) recombination in the bulk, (s) diffusion of acceptor and reduction on the surface of SC, and (t) oxidation of donor on the surface of SC particle (Gaya and Abdullah, 2008).

### 2.3.2 Titanium dioxide as photocatalyst

Titanium dioxide ( $TiO_2$ ) is a white powder and widely used as catalyst because of its stability towards photocorrosion, its low toxicity and low costs. In addition, it is relatively inexpensive, stable chemically, and the photogenerated holes are highly oxidizing (Fujishima and Zhang, 2006).  $TiO_2$  occurs in three different crystal forms known as rutile, brookite and anatase. It also consists of valence band (VB), the highest occupied band full of electron, and conduction band (CB), the lowest unoccupied band. These bands are separated by different energy level which is called “band gap energy.” The multiple crystallographic phases of  $TiO_2$ , rutile is excited by visible light, but has a fast charge recombination rate, leading to low efficiency and anatase is excited by near-UV light and has a slower rate of charge recombination, resulting in higher efficiency.

When a particle of  $TiO_2$  is illuminated with light of sufficient energy which is required due to the 3.2 eV band gap energy of anatase and 3.0 eV of rutile, an electron from the VB is excited across the band gap to the CB, leaving a positively-charged hole behind. These charges may participate in redox reactions at the surface of the particle. The hole has the potential to oxidize water that may be on the surface of the material resulting in the formation of hydroxyl radicals. Hydroxyl radicals are

themselves very powerful oxidizers, and can easily oxidize any organic species that happens to be nearby, ultimately to carbon dioxide and water. Meanwhile, in the conduction band, the electron has no hole to recombine with, since it has oxidized surface bound water. It rapidly reduces oxygen to form the superoxide anion. This can subsequently react with water to form, again, the hydroxyl radical. The processes are summarized below (Bahnemann, 2004).



Heterogeneous photocatalytic using  $\text{TiO}_2$  has several attractions.  $\text{TiO}_2$  shows efficient destruction of toxic contaminants and reacts with organic pollutant at ambient temperature and pressure. The commercial catalyst, Degussa P25, mixed phase catalysts with a high degree of rutile-anatase interfaces are highly efficient photocatalysts (Hurum, Agrios, and Gray, 2003). Although,  $\text{TiO}_2$  has several attractions the process has the limitation of the efficiency due to the recombination phenomenon. These can be improved by depositing noble metals, doping transition metal ions, combining with semiconductors and modifying with other substances (Yang et al., 2002). The benefits of modifications are inhibiting electron-hole recombination by increasing the charge separation, increasing the wavelength response range and changing the selectivity or yield of a particular product. However, the photoactivity of the catalysts depends on several factors as for example the chemical and physical properties of catalyst, the relative recombination rate of photoexcited electrons and holes.

#### 2.4 Transition metal-doped $\text{TiO}_2$

It can be seen that the essence of a photocatalytic mechanism is the production of photogenerated electron and hole. The ease of production and separation of these species will consequently increase the photocatalytic activity of  $\text{TiO}_2$ . Therefore the smaller the band gap, the higher the production of the electron and hole. The transition energy of an electron from the VB to CB can change with the existence of



impurities or dopant in the semiconductor. Doping implies incorporation of a foreign cation into the catalyst matrix of the parent metal oxide (Karakitsou and Verykios, 1993). In this study, iron (Fe), vanadium (V), and tungsten (W) have been used as dopants in the effort to increase the photocatalytic reactivity of  $\text{TiO}_2$  because there are similar ionic radii as shown in Table 2.3.

**Table 2.3** Atomic and ionic radius of Fe, V, and W (Shannon, 1976).

Radius	Fe	V	W
Atomic	140	134	139
Ionic			60 (+6)
		54 (+5)	62 (+5)
	58 (+4)	58(+4)	66 (+4)
	64 (+3)	64 (+3)	
	78 (+2)	79 (+2)	

Different metals have been doped into  $\text{TiO}_2$  in order to alter the material's optical properties. It is desirable to maintain the integrity of the crystal structure of the host material and to produce favorable changes in electronic structure. It appears easier to substitute the  $\text{Ti}^{4+}$  cation in  $\text{TiO}_2$  with other transition metals due to the similar in charge states and ionic radii. The small size of the nanoparticle is beneficial for the modification of the chemical composition of  $\text{TiO}_2$  due to the higher tolerance of the structural distortion (Chen et al., 2003). Therefore, the preparation methods have to be considered in order to obtain the desired photocatalyst.

#### 2.4.1 Synthesis of transition metal-doped $\text{TiO}_2$

The preparation methods of transition metal-doped  $\text{TiO}_2$  can be divided into three types: wet chemistry, high temperature treatment, and ion implantation on  $\text{TiO}_2$  materials. Wet chemistry methods usually involve hydrolysis of a titanium precursor in a mixture of water and other reagents, followed by heating. Choi and co-workers



performed a systematic study of TiO<sub>2</sub> nanoparticles doped with 21 metal ions by the sol-gel method and found the presence of metal ion dopants significantly influenced the photoreactivity, charge carrier recombination rates, and interfacial electrontransfer rates (Choi, Termin, and Hoffmann, 1994). Nagaveni and colleagues prepared W, V, Ce, Zr, Fe, and Cu ion-doped anatase TiO<sub>2</sub> nanoparticles by a solution combustion method and found that the solid solution formation was limited to a narrow range of concentrations of the dopant ions (Nagaveni, Hegde, and Madras, 2004).

Gracia and co-workers synthesized M<sup>n+</sup> (Cr, V, Fe, Co)-doped TiO<sub>2</sub> by ion beam induced CVD and found that TiO<sub>2</sub> crystallized into the anatase or rutile structures depending on the type and amount of cations present (Garcia et al., 2004). Wang and co-workers synthesized Fe(III)-doped TiO<sub>2</sub> nanoparticles using oxidative pyrolysis of liquid-feed organometallic precursors in a radiation frequency (RF) thermal plasma (Wang et al., 2005). In this study, the solvothermal method is utilized for the development of metal-doped TiO<sub>2</sub> catalysts since it is a low-cost, convenient, and robust method. It has evidence that this method normally has better control than hydrothermal methods of the size and shape distributions and the crystallinity of the TiO<sub>2</sub> nanoparticles. In addition, it has been found to be a versatile method for the synthesis of a variety of nanoparticles with narrow size distribution and dispersity (Chen and Mao, 2007).

## **2.4.2 Properties of transition metal-doped TiO<sub>2</sub>**

It has been well documented that the core of a photocatalytic mechanism is the production of photogenerated electron and hole. The ease of production and separation of these reactive species will consequently increase the photocatalytic activity of TiO<sub>2</sub>. Herein, we summarize our work concerning Fe, V, and W-doped TiO<sub>2</sub> based materials, aiming to establish a structure-photo-activity link able to interpret their physio-chemical properties in the photodegradation of BTEX.

### **2.4.2.1 Optical property**

Many applications of TiO<sub>2</sub> are closely related to its optical property. One of the goals for improvement of the performance of TiO<sub>2</sub> materials is to increase their optical activity by shifting the onset of the response from the UV to the visible

region. A wide range of metal ions in particular transition metal ions, have been used as dopants in order to achieve this goal. A red shift in the band gap transition or a visible light absorption was observed in metal-doped  $\text{TiO}_2$ . Doping with transition metal implies incorporation of a foreign cation into the catalyst matrix of the parent metal oxide (Karakitsou and Verykios, 1993).

This red shift was attributed to the charge-transfer transition between the d electrons of the dopant and the CB (or VB) of  $\text{TiO}_2$ . The transition energy of an electron from the VB to CB can change with the existence of impurities or dopants in the semiconductor. In the bulk of crystalline material, translational symmetry leads to the formation of electronic energy bands. Dopants break the periodicity of the lattice and perturbed the band structure locally. The perturbation usually can be characterized by a discrete energy level that lies within the band gap. Therefore, new energy levels in the band gap are created when dopants are introduced into the semiconductor. If the new level lies between the VB and CB, the photocatalytic activity of the semiconductor is enhanced, as lower transition energy is required. Thus the smaller the band gap, the higher the production of the electron and hole.

The visible light photoactivity of metal-doped  $\text{TiO}_2$  can be explained by a new energy level produced in the band gap of  $\text{TiO}_2$  by the dispersion of metal particles in the  $\text{TiO}_2$  matrix. As shown in Figure 2.3, electron can be excited from the defect state to the  $\text{TiO}_2$  conduction band by photon with energy equals  $h\nu_2$ . Additional benefit of transition metal doping is the improved trapping of electrons to inhibit electron-hole recombination during irradiation. Decrease of charge carriers recombination results in enhanced photoactivity (Zaleska, 2008).

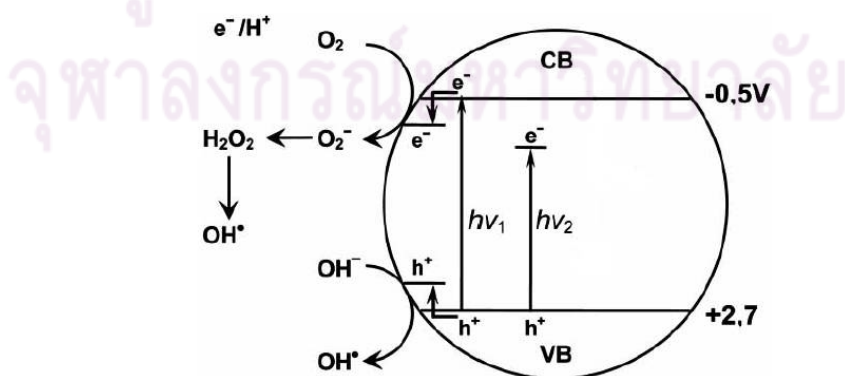
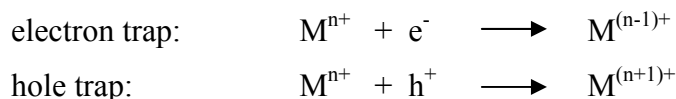


**Figure 2.3** Energy difference reduced due to metal ion dopants:  $h\nu_1$ : pure  $\text{TiO}_2$ ;  $h\nu_2$ : metal-doped  $\text{TiO}_2$  (Zaleska, 2008).

Besides lowering the transition energy of electron, metal ion dopants influence the photocatalytic activity of TiO<sub>2</sub> by acting as electron (or hole) traps and by altering the e<sup>-</sup>/h<sup>+</sup> pair recombination rate through the following process.



Where the energy level for M<sup>n+</sup>/M<sup>(n-1)+</sup> lies below the conduction band edge and the energy level for M<sup>n+</sup>/M<sup>(n+1)+</sup> above the valence band edge with respect to the reduction potential (E<sub>0</sub>) of each dopant. Each dopant species has its own intrinsic reduction potential; the more positive the potential, the greater the species' affinity for electrons and tendency to be reduced. The standard reduction potential of Fe<sup>3+</sup>, V<sup>5+</sup>, and W<sup>6+</sup> are shown in Table 2.4.

**Table 2.4** Standard reduction potential of Fe<sup>3+</sup>, V<sup>5+</sup>, and W<sup>6+</sup>.

Reaction	E <sub>0</sub> (V)	Reference
Fe <sup>3+</sup> + e <sup>-</sup> → Fe <sup>2+</sup>	0.77	Wang, Liu, and Cai, 2008.
V <sup>5+</sup> + e <sup>-</sup> → V <sup>4+</sup>	1.00	Ferrigno et al., 2002
W <sup>6+</sup> + e <sup>-</sup> → W <sup>5+</sup>	0.45	Kwon et al., 2000.

The introduction of such energy levels in the band gap will induce a red shift in the band gap transition and the visible light absorption through a charge transfer between a dopant and CB (or VB) or a d-d transition in the crystal field (Choi et al., 1994). The incorporation of metal ions into TiO<sub>2</sub> crystal lattice, therefore, can significantly extend the absorption by the photocatalysts into the visible region. Available energy levels and band gap position for various semiconductors are shown in Figure 2.4.

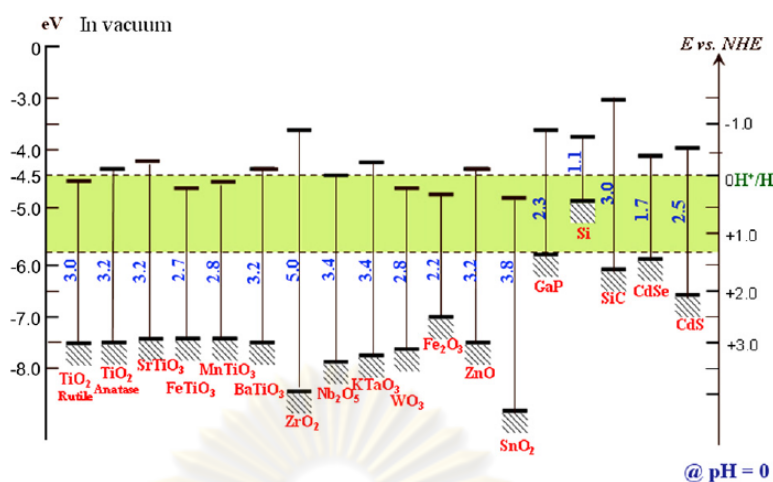


**Figure 2.4** Energy levels for various semiconductors (Jing et al., 2010).

#### 2.4.2.2 Electronic property

The electronic property of a material are closely related to its chemical composition (chemical nature of the bonds between the atoms or ions), its atomic arrangement, and its physical dimension (confinement of carriers) for nanometer-sized materials (Chen and Mao, 2007). The electronic structure of TiO<sub>2</sub> has been studied with various experimental techniques. The fine electronic structure of TiO<sub>2</sub> can be directly probed by X-ray-absorption near-edge structure (XANES). The XANES analysis can give details about the electronic structure and the local arrangement of atoms around the absorbing atom. The pre-edge and XANES regions of the absorption spectrum supply electronic information on the immediate environment of the absorbing atom which in principle can be translated into geometrical information.

XANES spectra of anatase and rutile are quite different although these two compounds have the same composition. The typical titanium atoms of anatase and rutile have a tetrahedral crystal structure (Ti<sup>4+</sup>) and surrounded by six oxygen atoms resulting in an octahedral coordination (TiO<sub>6</sub>) while oxygen anions have a coordination number of three, thereby, forming a trigonal planar. Moreover, there are some distortions in the octahedral structure (O<sub>h</sub>) of both that cause a longer bond length along the axial Ti-O bonds than those in horizontal plane. This distortion is slightly larger for anatase (Mo and Ching, 1991). This phenomenon results in anatase

and rutile point groups at  $D_{2d}$  and  $D_{2h}$ , respectively. The spectra are also different in the pre-edge region and white line positions because if the octahedral metal is distorted, then more p character will be mixed into the 3d band resulting in an increased intensity of the pre-edge.

The pre-edge of Ti atom is related to the transition in 3d bands possible resulting from the direct transition of 1s to 3d quadrupole and the dipole transition to 4p character hybridized with the 3d band. The contributions of quadrupole and dipole transitions are equivalent in intensity results of  $TiO_2$  producing the three pre-edge peaks. This character is caused by two effects: the core hole effect on the quadrupole peaks and the crystal field splitting between the  $t_{2g}$  and  $e_g$  orbital (De Groot, 2001). The electronic state of the absorber Ti atom reflects the chemical bond with oxygen atoms. Even if the Ti atom for these titania has the same coordination and valence electrons in the  $TiO_6$  octahedron, the oxygen atoms around Ti have different electronic state and orbitals, thus, the XANES spectra show the different electronic states of the Ti-O bonds in each compound. The transition of Ti pre-edge and  $K$ -edge in both rutile and anatase were illustrated in Figure 2.5.

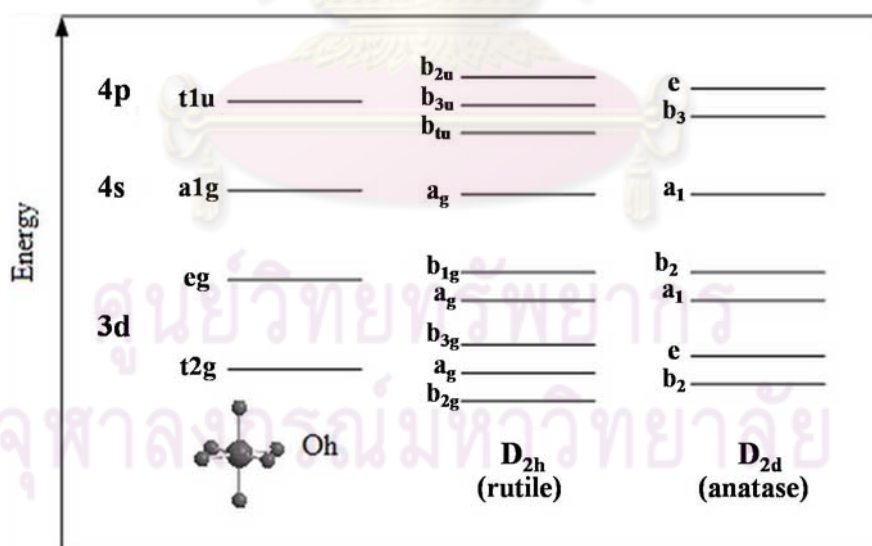


**Figure 2.5** Molecular orbital energy level diagram of the lowest unoccupied of  $TiO_6$  with  $O_h$ ,  $D_{2d}$  and  $D_{2h}$ .



Moreover, speciation (coordination number and oxidation state) of select elements can be determined by XANES. Nano  $\text{TiO}_2$  photocatalysts active for the degradation of  $\text{CHCl}_3$  have been shown by XANES to exist in a range of species (Hsiung, Wang, and Wang, 2006). By XANES and extended X-ray absorption fine structural (EXAFS) spectroscopies, Huang and co-workers found that copper oxide clusters involved in the catalytic oxidation of chlorophenols. These molecular-scale data turn out to be very useful in revealing nature of catalytic active species and reaction mechanisms involved (Huang, Wang, and Lee, 2003).

## **2.5 Photocatalysis of gas-phase BTEX using $\text{TiO}_2$**

Photocatalysis oxidation of VOCs using  $\text{TiO}_2$  has shown great potential in the field of air treatment. It gives a rapid and efficient destruction of a wide spectrum of low-level air pollutants (Herrmann, 2005). Several research groups had studied extensively the photooxidations of BTEX single compound using  $\text{TiO}_2$ . The oxidation rate of toluene at sub-ppm concentrations was found to increase with decreasing humidity (Obee and Brown, 1995). At steady state, benzene at 116-130 ppm in air containing 980-1000 ppm water vapor, approximately 4% of the benzene was removed (Jacoby et al., 1996). By removing water vapors, the conversion of toluene to benzaldehyde was almost completely inhibited (Martra et al., 1999). The reaction rate of toluene increase with toluene concentration feed up to 1200 ppm (Maira et al., 2001). 80% of benzene at 20 ppm was decomposed in the optical fiber photoreactor after 4 hours of ultraviolet irradiation with the presence of 5% RH (Wang and Ku, 2003). The toluene conversion was up to 90–100% with a slight influence of inlet concentration and RH (Sleiman et al., 2009).

Although the study of BTEX mixture compounds was also studied, there were still few studies in this area. Examples include the photocatalysis of benzene, toluene and xylene (BTX) (Pichat et al., 2000), the heterogeneous photocatalytic oxidation of benzene, toluene, cyclohexene and cyclohexane in humidified air (Einaga, Futamura, and Ibusuki, 2002), the removal of five target VOCs, benzene, ethyl benzene, and o-, m-, p-xylenes, at ppb level in vehicle air (Jo, Park, and Chun, 2002), the removal of nitrogen oxide (NO) and VOCs at typical indoor air level (Ao et al., 2003), the



photodegradation of benzene, toluene, ethylbenzene and o-xylene at ppb level and 50% RH (Strini, Cassese, and Schiavi, 2005).

Furthermore, the utilization of photocatalysts was studied using various supportive materials. The TiO<sub>2</sub>/AC filter was installed in an air cleaner available in the commercial market and tested inside an environmental chamber for photodegradation of indoor BTEX (Ao and Lee, 2005). TiO<sub>2</sub> as a photocatalyst in building materials, i.e. roofing tiles and corrugated sheets was used for removal of toluene from air (Demeestere et al., 2008).

In summary, as mentioned above, TiO<sub>2</sub> is the most commonly used material in various photocatalytic oxidation reactors. Most studies have been performed with powder TiO<sub>2</sub> particularly in anatase form. Consequently, “shadowing effect” has also been observed. In order to lighten these problems, several approaches have been taken by researchers. One of the most widely used techniques is to immobilize the TiO<sub>2</sub> as thin film on various supports including glass, stainless steel, quartz, silica gel and glass beads. Some experimental evidence indicates that different reaction conditions (i.e. pollutant concentration, water vapor concentration) affect the photocatalytic activity but some ignore its influence. The effect of photocatalytic oxidation is also not understood clearly when mixed VOCs are present.

## **2.6 Photocatalysis of gas-phase BTEX using transition metals-doped TiO<sub>2</sub>**

The improving of photocatalytic activity of TiO<sub>2</sub> by metal doping is widely studied but still limit in amount for the degradation of VOCs. For instance; the different Pd/TiO<sub>2</sub> samples were prepared for the degradation of toluene (Belver et al., 2003), the mesoporous anatase TiO<sub>2</sub> supported WO<sub>3</sub> photocatalysts was studied for the removal of concentrated toluene (110 ppm) in the gas phase (Bosc et al., 2006), the transition metal modified TiO<sub>2</sub> photocatalysts (Fe<sup>3+</sup>/TiO<sub>2</sub> and WO<sub>3</sub>/TiO<sub>2</sub>) were prepared by sol-gel method and examined upon photocatalytic degradation of benzene (Zuo et al., 2006), transition metal (Ni<sup>2+</sup>, Cr<sup>3+</sup>, Fe<sup>3+</sup>, Nb<sup>3+</sup>, and V<sup>5+</sup>) doped TiO<sub>2</sub> were synthesized by hydrothermal method for gas-phase benzene degradation (Lee et al., 2006).

The photocatalytic degradation of toluene in gas phase was studied using different porous manganese oxide doped TiO<sub>2</sub> prepared in aqueous and non-aqueous

medium and coated onto plastic nylon sheet (Jothiramalingam and Wang, 2007). The Sn and Zr doped TiO<sub>2</sub> (TiSn and TiZr, 8% of metal ions), and coupled TiO<sub>2</sub>/SnO<sub>2</sub> and TiO<sub>2</sub>/ZrO<sub>2</sub> catalysts coating on the external surface of the inner glass cylinder was also studied for the photocatalytic oxidation of toluene (Fresno et al., 2008). The preparation of Ni-doped TiO<sub>2</sub> photocatalyst by polyol method was studied and evaluated for the degradation of xylene vapor in air under UV light illumination in an annular photoreactor (Tseng et al., 2009).

In conclusion, work has been done to extend the absorption spectrum of TiO<sub>2</sub> into the visible region by metal doping. However, almost all studies still used UV light as a light source. A wide range of metal ions in particular transition metal ions, have been used as dopants and many controversial results are reported. A comparison and unifying conclusions among results reported for transition metal doped TiO<sub>2</sub> is difficult due to widely varying experimental conditions, sample preparation and the determination of photoreactivity. Although the amount of research using doped TiO<sub>2</sub> has increased, research on transition metal doped TiO<sub>2</sub> for photocatalytic oxidation of gas-phase VOCs especially for mixed BTEX under visible light is still very few.

## **2.7 Influence factors in gaseous photocatalysis**

The performance of photocatalysis in a typical indoor air environment is not fully understood although there are numerous developments in the field of photocatalysis. There are also technical issues that still need to be resolved. The parameters such as catalyst loading, flow rate, initial concentration, and light intensity were studied by many researchers but it is noted that not all the influencing factors were introduced clearly in some papers (Mo et al., 2009). In this study, the operational conditions that influence the reaction are focus on the relative humidity (RH), initial concentration, and flow rate.

### **2.7.1 Relative humidity**

The optimum relative humidity for utilizing photocatalytic process in indoor air cleaning must be determined. The competitive adsorption between water and trace contaminants had a significant effect on the photocatalytic oxidation rate (Obee and Brown, 1995). The water molecule adsorbed on the photocatalyst will react with the

hole and generate hydroxyl radical which in turn oxidized pollutants. In the absence of humidity the photocatalytic degradation of toluene is seriously retarded (Kim and Hong, 2002). However, excessive water vapor on the catalyst surface will inhibit the reaction rate because of the competitive adsorption between water vapor and pollutant. The presence of water vapor will compete with pollutants for absorption sites on the photocatalyst, hence reducing the removal rate (Obee and Hay, 1997).

Three ranges (10-20, 50-60, and 80-90 %RH) covering dry and humid environments, were tested for degradation of BTEX with TiO<sub>2</sub>. The degradation efficiency increased as RH decreased. For ethylbenzene and xylene the degradation efficiency was above 90 % for two RH ranges of between 10-20 % and 50-60 % (Jo and Kim, 2009). Toluene removal efficiency 86 % was obtained with TiO<sub>2</sub> cementitious material at 35-40 %RH (Ramirez et al., 2010). At parameter study of 1-77 %RH and toluene concentration of 465 ppm, photocatalytic removal of toluene on building material enriched with TiO<sub>2</sub> decreased at higher humidity (Demeestere et al., 2007). The conversion of toluene increased with increasing relative humidity, reaching a peak at 40–50% humidity and then remaining constant from 40–50% to 80–90%. At all relative humidity levels, the conversion was higher in the presence of TiO<sub>2</sub> than in its absence (Jeong et al., 2005).

It seems that the influence of water vapor in the gas-phase degradation reaction depends on the species of pollutants, as well as on the concentrations of both VOCs and humidity (Boulamanti and Philippopoulos, 2009). With respect to the nature of the pollutant, both enhancement and inhibition of the degradation rate can be caused by water vapor.

### 2.7.2 Initial concentration

Typically, pollutant concentrations found in an indoor environment range from ppb to sub-ppm levels and do not involve just a single pollutant but mixtures of compounds as reported in literature (Wong, Sin, and Yeung, 2002; Li et al., 2009). Based on our knowledge, almost all studies were conducted on laboratory settings under relatively high concentrations of pollutants. At a high concentration of pollutant all catalytic sites become occupied so that a further increase in the pollutant concentration does not affect the actual catalyst surface concentration. Usually, there

is an optimal pollutant concentration that will maximize the photocatalytic reaction rate when the other conditions are stable (Mo et al., 2009).

The degradation efficiency of benzene was quite closely correlated with the adsorption characteristics of benzene. At low initial concentrations of benzene, the amount of benzene molecules may be less than the number of reactive sites of the catalyst film, and therefore, the degradation efficiency is very high, while at high initial concentrations of benzene, the amount of benzene molecules may be more than the number of reactive sites on the catalyst film and only a fraction of them will be adsorbed onto the surface of catalyst, and therefore, the degradation efficiency is decreased with increasing initial concentration of benzene (Geng et al., 2008).

### 2.7.3 Flow rate

In heterogeneous catalytic reactions, the apparent oxidation rate depends on gas-phase mass transfer rate, or a rate limiting surface reaction rate, or both of them. In the region of lower gas flow rate (200–800 ml/min), the apparent toluene oxidation rate was dependent upon the gas-phase mass transfer rate which increased with the gas flow rate. When the gas flow rate was higher than 1000 ml/min, the rate determining step became the surface reaction (Yu and Lee, 2007). Where the toluene concentration was set at  $845 \pm 5 \text{ mg/m}^3$  and the relative humidity was adjusted to 30% the reaction rate increased with the gas flow rate from 0 to 1200 ml/min and then levels off as the gas flow rate increased from 1200 to 2400 ml/min. In heterogeneous catalysis, the factors that determine the rate-controlling step are mass transfer and surface reaction. The mass-transfer effect from the bulk phase to the surface of the catalyst is dominant at low flow rate; the reaction rate levels off when the flow rate is more than 1200 ml/min, indicating that the rate-controlling step has changed to surface reaction (Dezhi et al., 2005).

At toluene initial concentrations of 0.6 and 10 ppmv, in the presence of  $\text{TiO}_2$ , the conversion dropped as the flow rate was reduced from 1.0 to 3.0 l/min, the conversion did not decrease any further at flow rates higher than 3 l/min. These phenomena were probably due not only to the reduction of contact time in the gas phase but also to the limited diffusion mass transfer to the  $\text{TiO}_2$  (Jeong et al., 2005). The degradation conversion of the  $\text{TiO}_2$  film catalyst gradually decreased with

increasing gas flow rates from 0.02–0.10 l/min over 20–80 min, while increased gas flow rates resulted in a slight decline in the degradation conversion value of the TiO<sub>2</sub> film catalyst after illumination for 2 h (Geng et al., 2008).

The flow rate is an important factor that affects photocatalytic reaction by changing the convection mass transfer and diffusion between pollutant and photocatalyst. The mass transfer resistance from the gas bulk phase to the solid photocatalyst surface would reduce the reaction rate. However, the mass transfer resistance would decrease with increasing the gas flow rate. As the flow rate increases, the reaction rate should become independent of the fluid velocity, and the observed reaction kinetics are released of mass transport limitations. Therefore, at high flow rates, the observed kinetics are controlled by the surface reactions only. Several authors have noted this effect in gas-phase photocatalytic reactors using immobilized TiO<sub>2</sub> (Jacoby et al., 1995; Wang, Tsai, and Hsieh, 1998).



ศูนย์วิจัยทรัพยากร  
จุฬาลงกรณ์มหาวิทยาลัย



# CHAPTER III

## METHODOLOGY

### 3.1 Materials and chemicals

#### 3.1.1 Chemicals and reagents

The catalysts used in this study were prepared by doping iron, vanadium and tungsten (Fe, V and W) onto TiO<sub>2</sub>. Titanium-tetraisopropoxide (TTIP) and isopropyl alcohol were used as the TiO<sub>2</sub> precursor and solvent, respectively. Iron (III) nitrate nonahydrate (Fe(NO<sub>3</sub>)<sub>3</sub>·9H<sub>2</sub>O), Ammonium metavanadate (NH<sub>4</sub>VO<sub>3</sub>) and sodium tungstate (Na<sub>2</sub>WO<sub>4</sub>·2H<sub>2</sub>O) were used as the Fe, V and W source, respectively. Polyethylene glycol (PEG, average molecular weight: 20000) was selected as the directing reagent. Diglycidyl ether of bisphenol A (DGEBA) was used as adhesive. All chemicals were analytical grade and were used without further treatment.

#### 3.1.2 Experimental set up

The photocatalytic oxidation of BTEX was carried out in a gas phase batch reactor as shown in Figure 3.1. There are three main parts of the reactors: the BTEX saturators (A), the humidifier (B) and the catalytic reaction vessel. The reaction vessel contained three concentric cylinders made of borosilicate glass. Each layer was sealed from each other. The outermost layer was for controlling the temperature by means of water circulation, or vacuum pumping. The innermost layer, or the central core, situated the light source (Toshiba, FL18W/T8/EX-D fluorescent daylight lamp,  $\lambda_{\text{max}} \sim 425$  nm). The middle layer was the section where the gas flowed and catalytic reaction took place. The flexible catalyst-coated FGC was inserted into this section by wrapping around the outside surface of the central core and was thus, in direct contact with the gas in the middle layer. The light intensity at the surface of the FGC was 58 W/m<sup>2</sup> as determined by a power meter (Kimo Solarimeter SL100). The BTEX vapours were generated from the saturators by bubbling helium gas through a series of three glass saturators containing BTEX liquid. Its concentration can be controlled



by adjusting temperature of the saturators and the flow rate of dilution gas (pure oxygen).

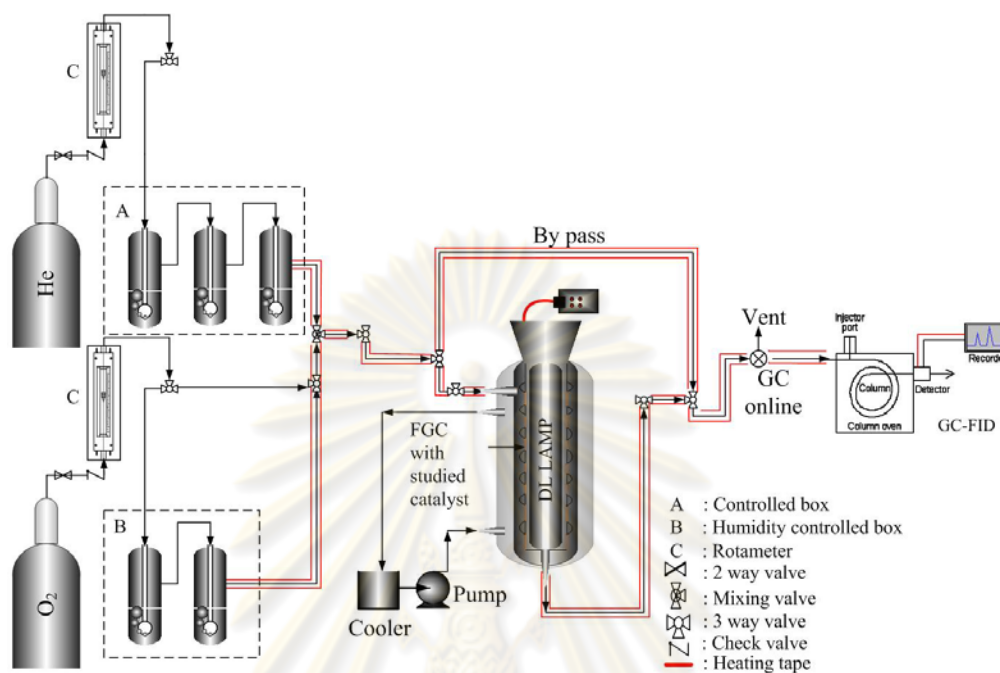


**Figure 3.1** Schematic diagram of the set up used for photocatalytic degradation test of the BTEX gases by the prepared catalyst-coated FGC.

### 3.2 Catalyst preparation

Transition metals (Fe, V, and W)-doped TiO<sub>2</sub> catalysts were prepared by the solvothermal method (Misook, 2007) using Fe(NO<sub>3</sub>)<sub>3</sub>·9H<sub>2</sub>O, NH<sub>4</sub>VO<sub>3</sub> and Na<sub>2</sub>WO<sub>4</sub>·2H<sub>2</sub>O as metal sources at a concentration of 0.1 molar ratio to the TTIP. The synthesized catalysts were denoted as M-TiO<sub>2</sub>, where M represents each metal dopant. The synthesis was started by solvolysis of the TTIP and metal ions with isopropyl alcohol (IPA) in the presence of polyethylene glycol (PEG) and followed by the thermal crystallization at 100°C. In Figure 3.2, the preparation of M-Ti molar ratio is shown. First, solution (a) was prepared by mixing metal ion, PEG and IPA and allowed to stir at 40°C for 4 hours. Second, solution (b) was prepared by diluting TTIP with IPA. Then solution (b) was dropped into solution (a) with vigorous stirring condition for 2 hours at 60°C. In the typical procedure, the reaction was carried out in

molar ratio as follows: TTIP: PEG: IPA = 55.6:1:216 and the weight ratio of PEG to IPA is 10 %. In the solvothermal route, the mother liquor was transferred to Teflon-lined autoclave 80 % filled and tightly closed for solvothermal reaction. The solvothermal treatment was carried out at 100°C for 1 day and then the slurry with different color depending on metal ions will be obtained. After being dried at 80°C overnight, the powder will be calcined for 3 hours at 600°C, crushed into fine particles and maintained in desiccators until the time of immobilization.

Pristine fibreglass cloth was heat-treated in an electric furnace at 500°C (5°C/min.) for 2 hours before immobilization of the catalysts to ensure complete removal of any organic residuals and then cut into pieces of equal size. The immobilization was done by dispersing 1 g of the prepared catalysts in acetone followed by addition of an equal amount of epoxy resin under constant agitation until uniformly mixed and then coated onto the FGC by spray coating. The coated FGC was then calcined at 450°C for one hour with the heating rate of 2°C/min. The amount of coated catalysts on FGC was controlled to be the same at around 0.3 mg/cm<sup>2</sup> for all prepared samples.

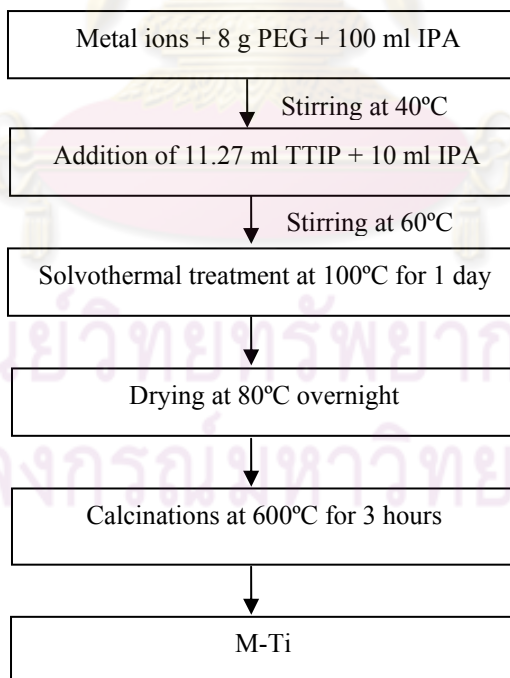


**Figure 3.2** Preparation of M-Ti molar ratio by solvothermal method.

### **3.3 Catalyst characterization**

The information obtained from the characterization process can help in understanding the relationship between the catalytic behavior and the composition and structure of the catalyst. However, although various techniques can provide valuable results on the catalyst properties, the meaningful information always comes from a combination of several characterization techniques.

#### **3.3.1 Thermal gravimetric analysis and differential thermal analysis (TGA-DTA)**

Simultaneous thermal gravimetric and differential thermal analysis measurements were performed on NETZSCH STA 449C. The temperature ranged from 30 °C to 800 °C with a heating rate of 5 ° C/min in order to obtain crystallization and phase transformation data. All analyses were performed in a following nitrogen atmosphere. For each experiment, 35 mg of sample was used and using alumina as a reference.

#### **3.3.2 Transmission electron microscope (TEM)**

Imaging and analytical characterization of nanoparticles by TEM is commonly performed to assess nanoparticles shape, size, morphology, and element distribution. In this study, the morphology of all doped samples was studied by transmission electron microscope (JEOL, JEM-2010).

#### **3.3.3 Scanning electron microscope (SEM)**

Scanning electron microscope was used to examine objects on a very fine scale. It can yield information on the topography of samples (surface feature) and morphology the sample (shape and size). The morphology of samples after immobilized onto fiberglass cloth and the pristine fiberglass cloth were observed by the scanning electron microscope (JEOL, JSM-640) equipped with Sony video graphic printer (UP-897 MD).

### 3.3.4 X-Ray diffraction (XRD)

X-ray diffraction was used for identifying the crystallographic phases present in solid materials and powders and for analyzing structural properties of the phase such as crystallite size, phase composition, and defects, etc. The crystal phases and structures of the synthesized samples were performed by using a powder X-ray diffractometer, Bruker D8, equipped with a Cu K $\alpha$  radiation source (wavelength 1.5406Å). All of the immobilized samples were run at an angle of 2 $\theta$  from 20° to 80° with a step size of 0.02° and a time step of 2.0 sec to assess the structure of the matrix. The crystallite sizes of all samples were determined from the broadening of corresponding X-ray spectral peaks by the Scherrer formula as shown in equation (3.1).

$$D = \frac{K\lambda}{\beta \cos \theta} \quad (3.1)$$

Where D is the crystallite size, K is a constant usually taken 0.9,  $\lambda$  is the wavelength corresponding to the Cu K $\alpha$  radiation,  $\beta$  is the full width at half maximum (FWHM) of the diffraction peak of anatase (101), and  $\theta$  is the diffraction angle. In addition, the anatase and rutile content is also present in this study by using equation (3.2) (Yang, Li, and Wang, 2005).

$$C_A = \frac{A_A}{A_A + 1.265 \cdot A_R} \cdot 100\% \quad (3.2)$$

where  $C_A$  is the anatase TiO<sub>2</sub> content in the deposit, and  $A_A$  and  $A_R$  are the areas covered by the anatase (101) peak and the rutile (110) peak, respectively.

### 3.3.5 X-ray absorption near edge structure (XANES)

The oxidation state and local geometry of samples were studied by XANES at beamline 8 of the Synchrotron Light Research Institute (Public Organization), Thailand. Details of the set-up were described elsewhere (Klysubun et al., 2007; Khemthong et al., 2010). In brief, XANES spectra were taken at room temperature in

fluorescent mode using a 13-element Ge detector with double Ge (220) crystal monochromators for selection of photon energy. Incident photon intensity was monitored by an ion chamber filled with argon gas. Titanium metallic foil was used for calibration of photon energy at its *K*-edge transition. The absorbances at the edge jump of all samples were in the range of 1-2 in order to ensure good signal-to-noise ratio. The obtained spectra were processed and corrected for background absorptions using Athena program (Ravel and Newville, 2005). Spectra were normalized following the procedure of Farges and co-workers (Farges, Brown, and Rehr, 1997) by dividing the pre-edge intensity with the atomic absorption in the post-edge region in order to make comparison between the Ti local coordination and geometry in our results to those extensively classified in their work.

### **3.3.6 UV–vis diffuse reflectance spectroscopy (UV- DRS) and band gap measurement**

The UV–VIS diffuse reflectance spectroscopy measurement (DRS-UV) was carried out using a Hitachi U-3010 (Japan) spectrophotometer with an integrating sphere to determine the absorption property of the photocatalysts. The range of wavelengths employed is 200-800 nm and the pure powder BaSO<sub>4</sub> was used as a reference. In order to determine the band-gap energy more accurately than that inferred from an absorption edge, the UV-DRS spectra were transformed using Kubelka-Munk method.

### **3.3.7 Photoluminescence spectrometer (PL)**

The PL spectra were obtained by the photoluminescence spectrometer at room temperature (Perkin Elmer LS-55) with the excitation and emission slit widths 5 and 7.5 nm, respectively. The samples were excited with monochromic light from a xenon lamp using an excitation wavelength of 315 nm and the emission spectra recorded from 350 to 450 nm.



### 3.4 Photocatalytic testing

The reactor was flushed and filled with pure oxygen prior to introduction of BTEX vapour. The controlled amount of BTEX vapour was allowed to mix with the oxygen gas that had 30% and 70% relative humidity and the mixture flow through the reactor for 2 hours in the dark to attain equilibrium adsorption. Once the polluted air concentration stabilized, the inlet valve to the vessel was closed and the lamp was turned on. The BTEX concentrations were recorded against the illumination time throughout the test. All BTEX concentrations at the sampling points were monitored by a gas chromatograph (GC 14A, Shimadzu Co. Ltd.) equipped with a flame ionization detector (FID) with a DB1 capillary column. The GC uses Helium as a carrier gas with a column temperature of 50°C, an oven temperature of 200°C and the detector temperature of 200°C. Table 3.1 shows the gas chromatography retention time (RT) of BTEX studied.

**Table 3.1** GC retention time of BTEX.

Organic Compound	RT (minutes)
Benzene	2.3
Toluene	4.5
Ethylbenzene	6.8
<i>o</i> -xylene	7.3

The percentage removal of BTEX can be calculated from the following equations (3.3).

$$\text{Removal}_i (\%) = \frac{[BTEX]_{inlet_i} - [BTEX]_{outlet_i}}{[BTEX]_{inlet_i}} \times 100 \quad (3.3)$$

where  $[BTEX]_{inlet_i}$  is the initial concentration of each BTEX inside the reactor at 0 minute and  $[BTEX]_{outlet_i}$  is the concentration of each BTEX inside the reactor at 120 minute.



The reference blank tests were carried out in two conditions at room temperature under atmospheric pressure using toluene as representative BTEX gas: one illuminated without catalyst and the other with P25-coated FGC catalyst but without irradiation. In all experiments, the BTEX concentration was controlled in the range of 1000-1200 ppm with catalysts loaded on FGC at  $0.30 \pm 0.06 \text{ mg/cm}^2$ . Samples were collected at time intervals of 0, 30, 60, 90 and 120 minutes. The blank-test results showed that the toluene concentration after 120 minutes was similar to the initial toluene concentration, indicating that the toluene was not lost due to reactor leakage or adsorption.

### 3.4.1 BTEX calibration

Prior to the photodegradation tests, experiments to obtain the calibration graph for BTEX were conducted. A 1000 mL glass container attached with an injection port and gas tap at each end was used. In a typical experiment the glass container was first vacuumed to discard any contaminants and equalized the pressures between inside and outside the container. Then a certain amount of each BTEX was injected into the container. After complete evaporation of the BTEX (typically after 15 minutes), 0.5 mL of the gas was injected out and analyzed using the GC-FID. The same procedure was followed for different volumes of BTEX. The volume of each BTEX was converted to concentration in ppm (detailed in Appendix A) and calibration graph was obtained by plotting the peak area versus the BTEX concentration in ppm. The calibration graphs of BTEX show excellent straight lines which intercept on the origin as shown in Figure 3.3 and the  $R^2$  of the lines are closed to 1 as shown in Table 3.2.

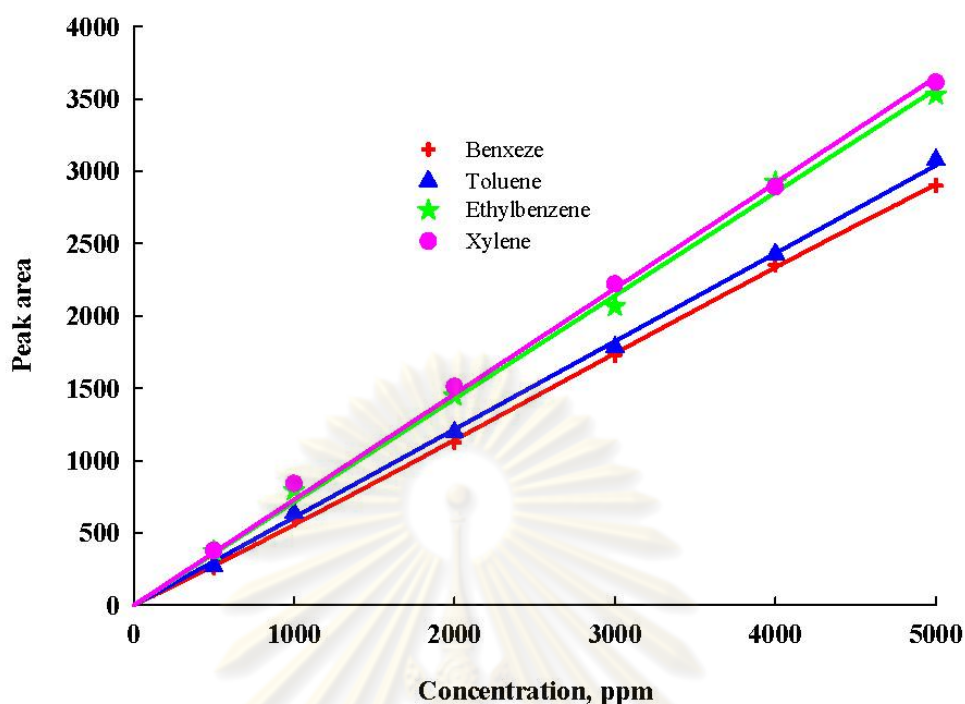


**Figure 3.3** Calibration graph of peak area versus concentration for BTEX.

**Table 3.2** Liner equation and  $R^2$  of each BTEX.

Organic Compound	Equation	$R^2$
Benzene	$Y=0.580x$	0.999
Toluene	$Y=0.608x$	0.998
Ethylbenzene	$Y=0.713x$	0.996
O-xylene	$Y=0.730x$	0.996

### 3.4.2 Reliability testing

In order to test the reliability of catalyst, the used V-TiO<sub>2</sub> on FGC was reused twice. Before the reuse, it was regenerated by the calcination at 450°C for an hour and 100 hours with the heating rate of 2°C/min, respectively. For comparing the regenerated catalyst ability, the regenerated catalysts were used to treat BTEX under the same conditions, except the testing time. The cycles of regeneration were presented in a diagram as shown in Figure 3.4. The calcinations temperature was set

in longer period of time in order to prove the severe condition. As well as the reaction time was set longer to 10 hours. The severe test was carried out in order to reduce the time consuming for a long period of time. The reliability was evaluated from comparing percent variation of each cycle to fresh catalyst.

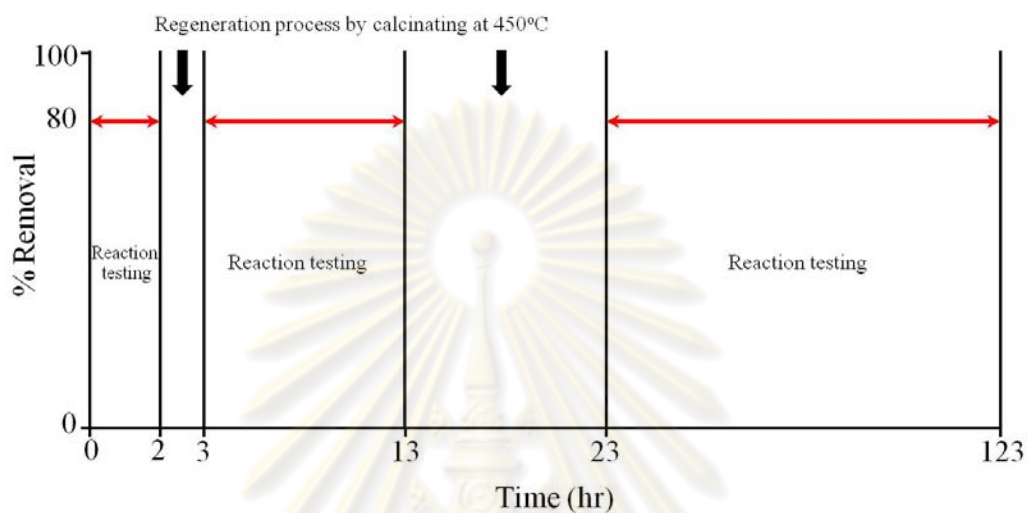


Figure 3.4 Reliability set up test.

ศูนย์วิทยทรัพยากร  
จุฬาลงกรณ์มหาวิทยาลัย

## CHAPTER IV

### RESULTS AND DISCUSSION

In this chapter, the results are presented and discussed into 2 parts; the catalyst characterization and the photocatalytic testing. The characterization elaborating on surface morphology in powder form (TEM) and morphology after immobilized onto fiberglass cloth (SEM), the identification of the phase structure (XRD), absorption properties (UV-Vis), band gap energy (Kubelka Monk Method), the change in recombination (PL) and oxidation state and local geometry of the Ti atoms (XANES) of the prepared catalysts will be discussed first. Data on the photocatalytic oxidation of the BTEX will be discussed next. The effect of dopants on the photocatalytic activity of TiO<sub>2</sub> will be detailed out, highlighting on the role of dopants. The photocatalytic degradation of mixed BTEX will be discussed in the final part of this chapter. All degradation data are stated in terms of percentage removal efficiency.

#### 4.1 Catalyst characterization

The Fe, V and W doped-TiO<sub>2</sub> were successfully synthesized via solvothermal method at a concentration of 0.1 molar ratio and immobilized onto fibreglass cloth (FGC) for use in photocatalytic decomposition of gaseous volatile organic compounds (BTEX). In order to understand the relevance of transition metals on physico-chemical properties of transition metals doped TiO<sub>2</sub> based catalysts, the obtained catalysts were systematically characterized as the following:

##### 4.1.1 Fe-TiO<sub>2</sub> (Fe/Ti mole ratio = 1)

###### 4.1.1.1 TGA-DTA

TGA–DTA analysis was applied to study the thermal decomposition behavior of the synthesized sample. In this study, the thermal decomposition of as-synthesized material was evaluated, as shown in Figure 4.1. The results contributed an appropriate range of calcination temperature which will be used in the further work. The TGA curve could be classified into three stages of weight loss. The first range

occurred from room temperature to 200°C with approximately 5% weight loss, while the DTA curve displayed a broad endothermic peak centering at 84°C. This presented the removal of residual acetone, isopropyl alcohol, and dry gel powder (Wang et al., 2008; Hung et al., 2008). The second region with approximately 55% weight loss between 200–500°C attributed to the combustion of organic templates, and nitrate ion, as confirmed by the exothermic peak of 336°C. The weight loss in the temperature range of 180–500°C is due to burnout of the organic PEG-20,000 surfactant species situated inside mesopore of the sample. It is evident that the exothermic reaction of the surfactant molecules through oxidation is responsible for the release. Thus, this peak can be assigned to the oxidative decomposition of the organic PEG-20,000 surfactant template and the exothermic peaks is mainly resulted from not only burn out of small portion of organic residues but also involved with the crystallization process.

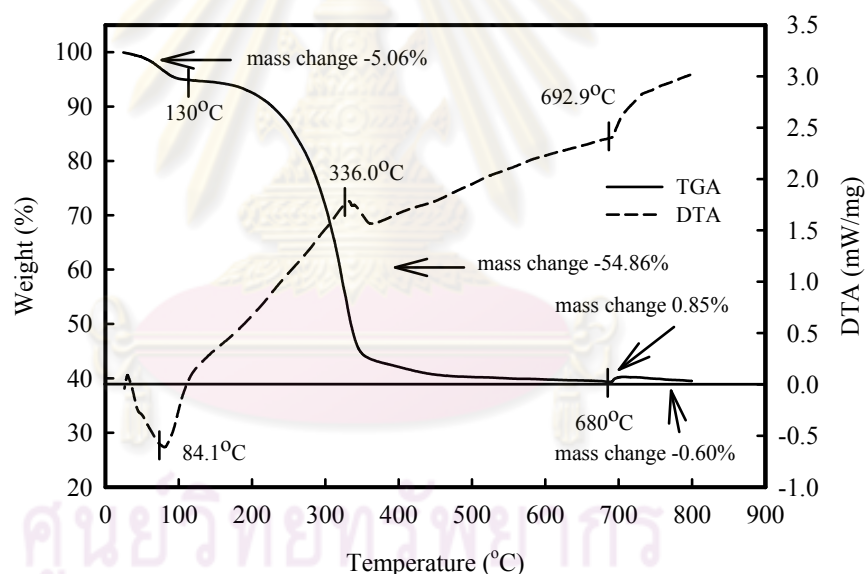


**Figure 4.1** TGA - DTA curves of the as-synthesized (dried) Fe-TiO<sub>2</sub> sample.

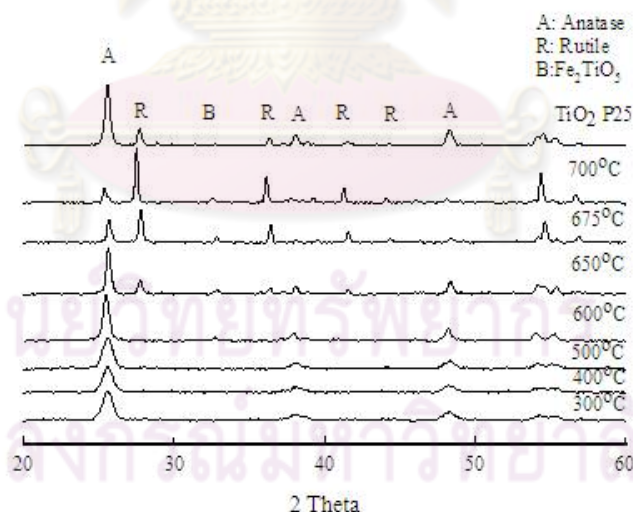
#### 4.1.1.2 XRD

Normally, X-ray diffraction patterns of TiO<sub>2</sub> nanoparticles obviously correspond to crystalline phase of anatase ( $2\theta$  : 25.6) and rutile ( $2\theta$  : 26.7). Average particle size of crystalline TiO<sub>2</sub> was obtained by using Scherrer equation which has been used to roughly estimate the size of the nanocrystalline photocatalyst.



Figure 4.2 shows the XRD patterns of commercial TiO<sub>2</sub> P25 and Fe-TiO<sub>2</sub> prepared by the solvothermal method calcined at temperatures from 300 to 700°C. It was found that phase-pure anatase existed in all samples calcined at 300–500°C, and the anatase phase changed to rutile phase at temperature higher than 500°C. Although the Fe<sup>3+</sup> could not be observed from XRD the XRF analysis showed the mole ratio of Fe/Ti equal to 0.09. This is mainly due to the fact that Fe<sup>3+</sup> were inserted into structure of titania and located at interstices or occupied some of Ti<sup>4+</sup> lattice site because of the diffusion and transfer of the ions.

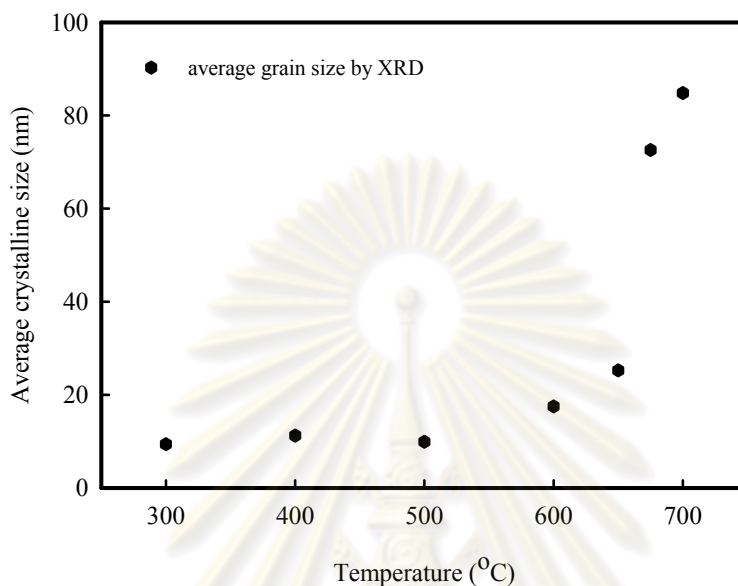
Interestingly, calcination temperature as low as 300°C is possible obtained a nanocrystalline product. The ability to process nanocrystalline anatase at such a low temperature is advantageous because it requires less energy for manufacturing. The increases in calcination temperature at lower than 500°C gave no effect with increasing in nanocrystalline anatase. The crystalline anatase sizes were about 9.4 – 11.2 nm as shown in Figure 4.3. There is appear to be very little different between crystal size versus calcination temperature. However, calcination temperature increased to 600°C, there was increased nanocrystalline anatase and average grain size.



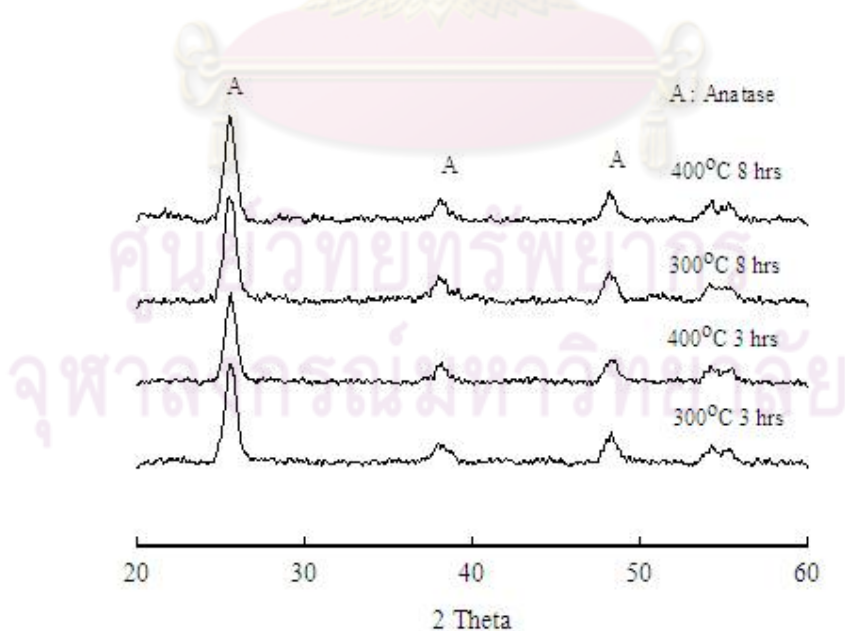
**Figure 4.2** XRD pattern of TiO<sub>2</sub> P25 and Fe-TiO<sub>2</sub> prepared by the solvothermal method calcined at temperatures between 300-700°C.

Figure 4.4 shows the XRD patterns of Fe-TiO<sub>2</sub> calcined at 300 and 400°C with different calcination time of 3 and 8 hours. The results showed that calcination time had no effect on the anatase phase. Thus, calcination for 3 hours was

sufficient to completely remove the template. The mass fraction of anatase to rutile was calculated using equation 3.2. The results are shown in Table 4.1.



**Figure 4.3** Effect of calcination temperature on average crystalline size of Fe-TiO<sub>2</sub> prepared by solvothermal technique and calcined for 3 hours.



**Figure 4.4** Effect of calcination time on nanocrystalline anatase phase of Fe-TiO<sub>2</sub> calcined at 3 and 8 hours.

**Table 4.1** Structure characteristics obtained by XRD, BET and SEM analyses.

Nominal composition	$S_{\text{BET}}$ ( $\text{m}^2/\text{g}$ )	Crystallite size (nm) (XRD)	Crystalline phase (%)	
			Anatase	Rutile
Commercial $\text{TiO}_2$ P25 (particle size 21 nm)	50	20.2	87	13
Fe- $\text{TiO}_2$ 300°C 3 hrs	90	9.4	100	0
Fe- $\text{TiO}_2$ 400°C 3 hrs	92	10.0	100	0
Fe- $\text{TiO}_2$ 500°C 3 hrs	52	9.9	100	0
Fe- $\text{TiO}_2$ 600°C 3 hrs	10	17.5	100	0
Fe- $\text{TiO}_2$ 650°C 3 hrs	6	25.2	72	28
Fe- $\text{TiO}_2$ 675°C 3 hrs	6	75.7	36	64
Fe- $\text{TiO}_2$ 700°C 3 hrs	6	91.4	9	91
Fe- $\text{TiO}_2$ 300°C 8 hrs	NA	10.6	100	0
Fe- $\text{TiO}_2$ 400°C 8 hrs	NA	10.0	100	0

NA: Not Analyzed

#### 4.1.1.3 Surface area by $\text{N}_2$ adsorption-desorption isotherms

Nitrogen adsorption-desorption isotherms of Fe- $\text{TiO}_2$  calcined at 500°C and 650°C and commercial  $\text{TiO}_2$  P25 are shown in Figure 4.5. The isotherm corresponded to type IV which is characteristic of mesoporous materials. Fe- $\text{TiO}_2$  calcined at 500°C, the well defined hysteresis loop with a sloping adsorption branch and a relatively steep desorption branch belongs to H2 type while the another one belong to H3 type. The volume adsorption at low  $P/P_o$  decreased with increasing calcination temperature. The results showed the relationship between the amount of surface area and the volume adsorption. The sample calcined at 400°C gave the

highest surface area and the higher calcination temperature, the lower surface area. The insert shows the pore size distribution which insignificantly changed with increasing calcination temperature but the pore volume at the same pore size was decreased with increasing calcination temperature. The surface areas are shown in Table 4.1.

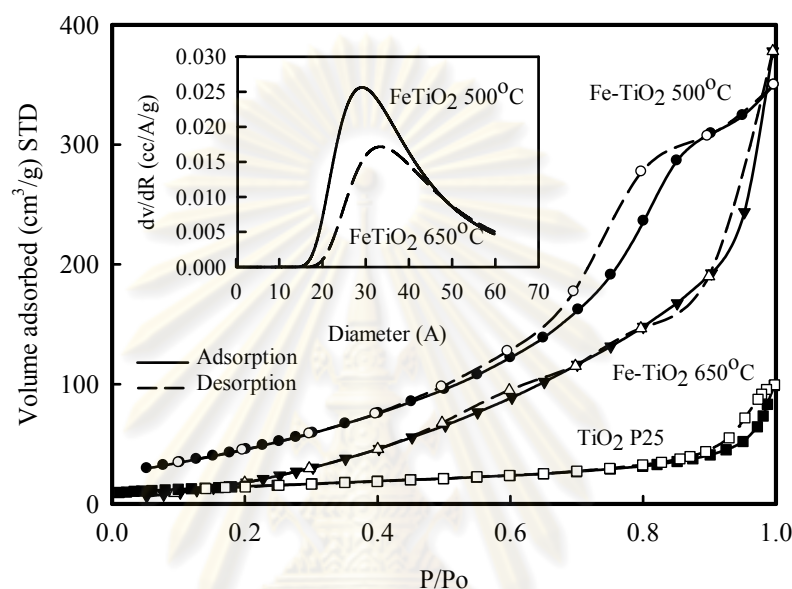


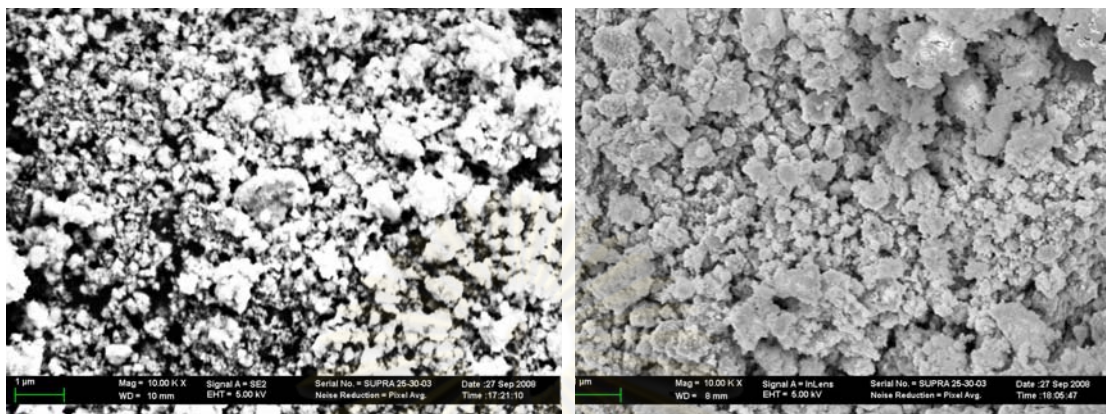
**Figure 4.5** N<sub>2</sub> adsorption and desorption isotherm of commercial TiO<sub>2</sub> P25 and Fe-TiO<sub>2</sub> calcined at 500°C and 650°C.

#### 4.1.1.4 SEM

The surface morphology of Fe-TiO<sub>2</sub> photocatalyst calcined at 500, 650, and 700°C was investigated by SEM and SEM-EDS as shown in Figure 4.6 and 4.7, respectively. It was found that the particles were aggregated with increasing of calcination temperature resulting in the increasing of particle size. The results were in agreed with the crystalline size calculated using Scherer equation (Table 4.1). The higher mesoporous could be observed from samples calcined at 500°C than that of samples calcined at 650°C and 700°C related to BET and pore size volume results.

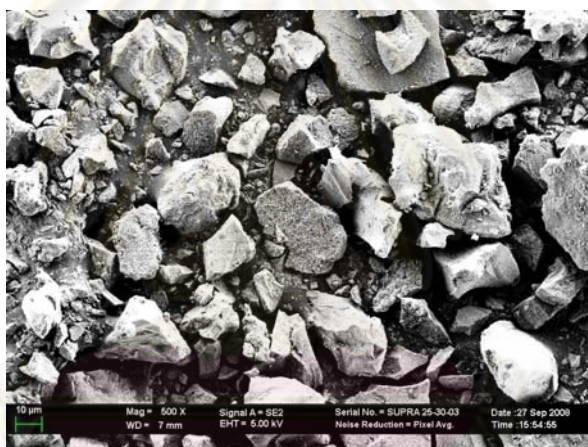
Figure 4.7 shows EDS analysis of Fe-TiO<sub>2</sub> catalyst calcined at 500°C. The EDS analysis provided useful information of the elemental distribution. The existence of dots in the element mapping images revealed the occurrence of all

investigated components (Ti, O, and Fe). The element mapping images showed that Fe specie was well dispersed throughout the bulk of Fe-TiO<sub>2</sub> photocatalyst.



(a) 500°C Magnitude 10 kX

(b) 650°C Magnitude 10 kX



(c) 700°C Magnitude 500 X

**Figure 4.6** SEM images of Fe-TiO<sub>2</sub> calcined at (a) 500°C, (b) 650°C and (c) 700°C.



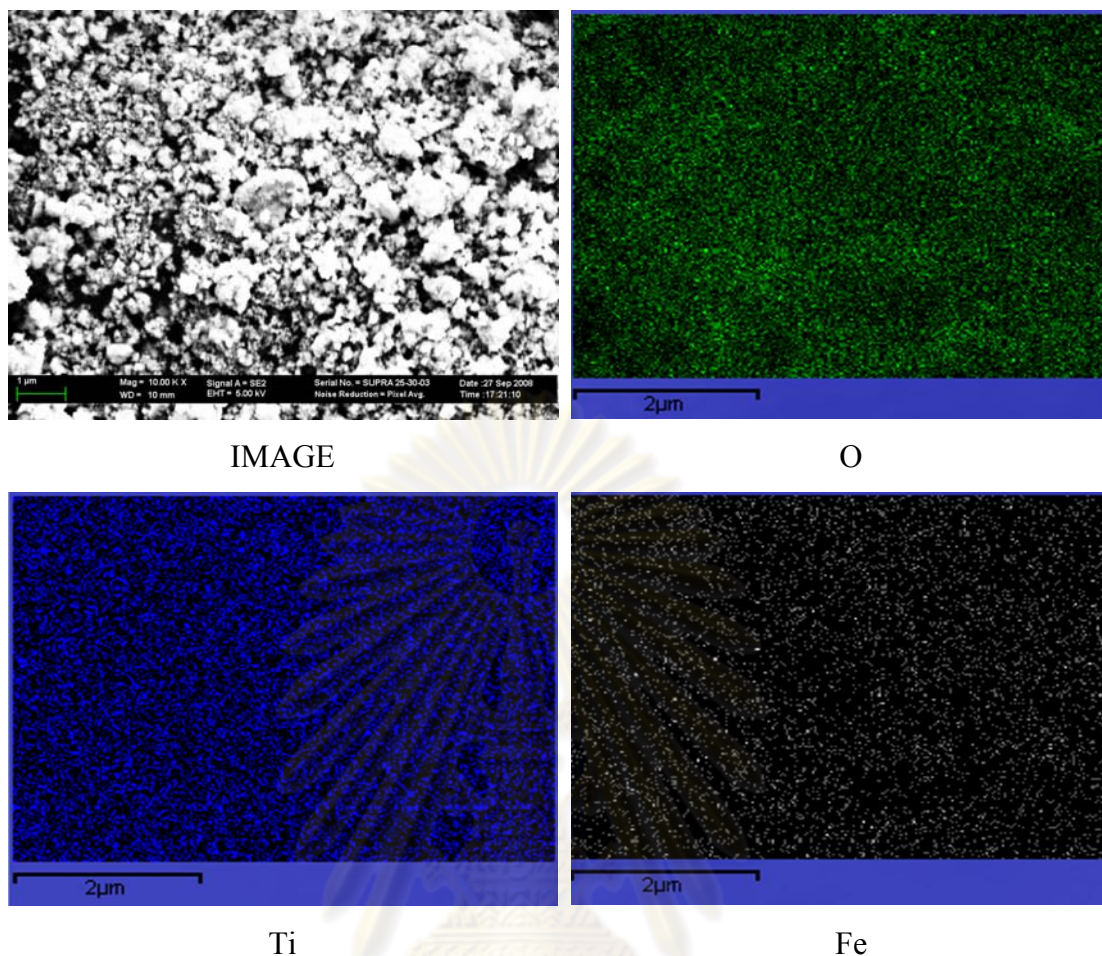


**Figure 4.7** SEM and elemental mapping of Fe-TiO<sub>2</sub> calcined at 500°C.

#### 4.1.1.5 UV-DR spectra

The UV-DRS spectra are shown in Figure 4.8. The results revealed that all Fe-TiO<sub>2</sub> samples displayed strong absorbance in ultraviolet range (250 to 350 nm) compared with the commercial TiO<sub>2</sub> P25. The sample calcined at 500°C showed the highest absorbance. The Fe<sup>3+</sup> doping induced the absorbance for visible light owing to the formation of intermediate energy levels and leading to a decrease in the band gap energy. The presence of Fe<sup>3+</sup> ions led to shift of absorption band to the visible region is called as red shift phenomena. Although the spectra of samples calcined from 300 to 700°C were different in intensity, they exhibited the same absorption band in visible light implying Fe<sup>3+</sup> doping could enhance visible light absorbance.

The absorption band around 500 nm can be attributed to d-d transition of from  ${}^2T_{2g} \rightarrow {}^2A_{2g}$  or charge transfer of Fe ions as  $Fe^{3+} + Fe^{3+} \rightarrow Fe^{2+}$  and  $Fe^{4+}$  (Zhou et al., 2006; Lui and Chen, 2009; Yu et al., 2009) Many reported that the absorption band at 415 nm assigned to charge transfer of  $Fe^{3+}$  to  $TiO_2$  conduction band according to the energy levels of 3d electron. Berrier and co-workers reported that the absorption band above 400 nm assigned to  $Fe_2O_3$  particles. Although the  $Fe^{3+}$  could not be observed from XRD, the spectrum of  $Fe^{3+}$  at wavelength about 500 nm established that some  $Fe^{3+}$  were on outer surface of catalysts. The band gap energy of the catalysts was calculated from UV-DR spectra according to Kubelka-Munk method as shown in Table 4.2. The results confirmed that the  $Fe^{3+}$ -doped  $TiO_2$  could active under visible light (Wavelength > 400 nm).

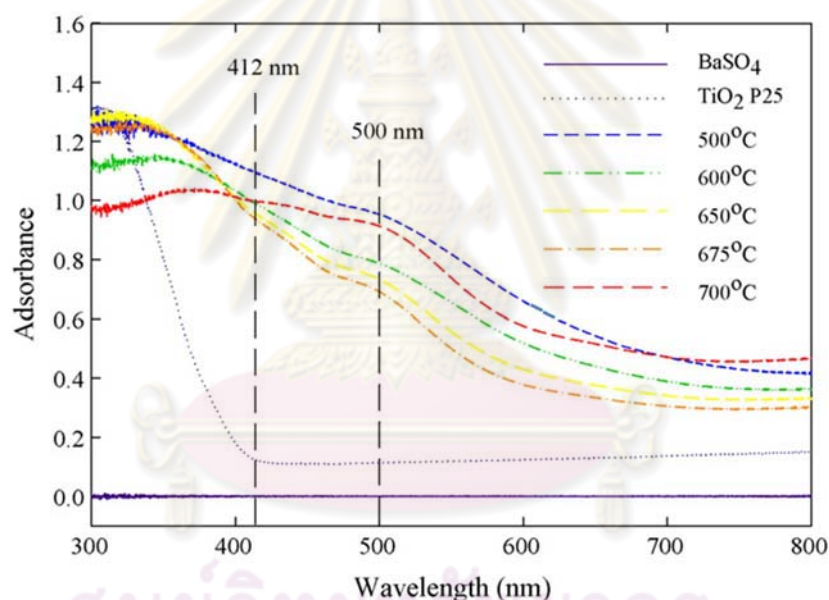


**Figure 4.8** UV-DR spectra of  $TiO_2$  P25 and  $Fe-TiO_2$  at different calcination temperatures.

**Table 4.2** Band edge wavelength and energy bandgap of materials.

Nominal composition	Band edge wavelength (nm)	Band gap energy (eV)
Commercial TiO <sub>2</sub> P25	390	3.18
Fe-TiO <sub>2</sub> 300°C	470	2.64
Fe-TiO <sub>2</sub> 400°C	476	2.61
Fe-TiO <sub>2</sub> 500°C	481	2.58
Fe-TiO <sub>2</sub> 600°C	468	2.65
Fe-TiO <sub>2</sub> 650°C	455	2.73
Fe-TiO <sub>2</sub> 675°C	444	2.79

#### 4.1.2 Fe, V, and W-doped TiO<sub>2</sub> (M/Ti mole ratio = 0.1)

##### 4.1.2.1 TEM

TEM analysis in Figure 4.9 shows that the TiO<sub>2</sub> particles as fine as several nanometers. The morphologies for these samples have no evident difference and all samples are approximately spherical particles. The change of shape and size of doped TiO<sub>2</sub> particles came from the addition of transition metals. This is in agreement with the study of Lee et al. (2006). The sizes of spheroids observed in Figure 4.9 are extremely different from the XRD calculated sizes, indicating that each spherical particle observed with TEM is not a single crystallite but the agglomerates of many single crystallites.

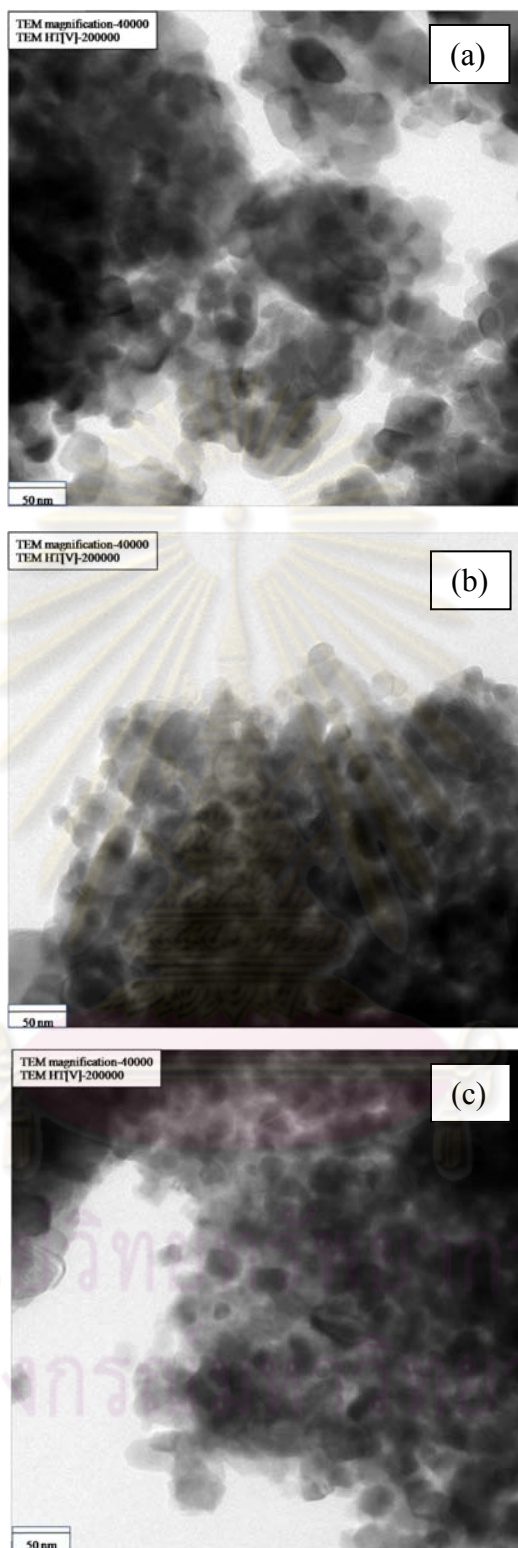


**Figure 4.9** TEM images of catalysts: (a) Fe-TiO<sub>2</sub>, (b) V-TiO<sub>2</sub> and (c) W-TiO<sub>2</sub>.



#### 4.1.2.2 SEM

The surface morphology of pristine FGC and catalyst immobilized onto FGC are shown in Figure 4.10 and Figure 4.11, respectively. The surface of FGC is slick and has the banded groove structure along the axis direction. Immobilized catalysts are fixed on the surface of FGC in the form of small clusters and the distribution is not very uniform. Although immobilized catalysts have been coated on almost all surfaces of FGC, the catalyst films on the surface of FGC are not thick and dense; therefore, the thickness of FGC varies little and they are still transparent. The weight of catalysts loaded onto FGC is  $0.33 \pm 0.06 \text{ mg/cm}^2$ .

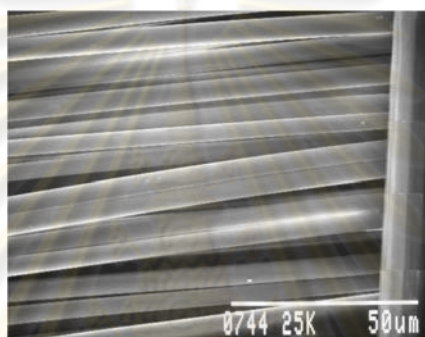


**Figure 4.10** SEM image of pristine fiberglass cloth.

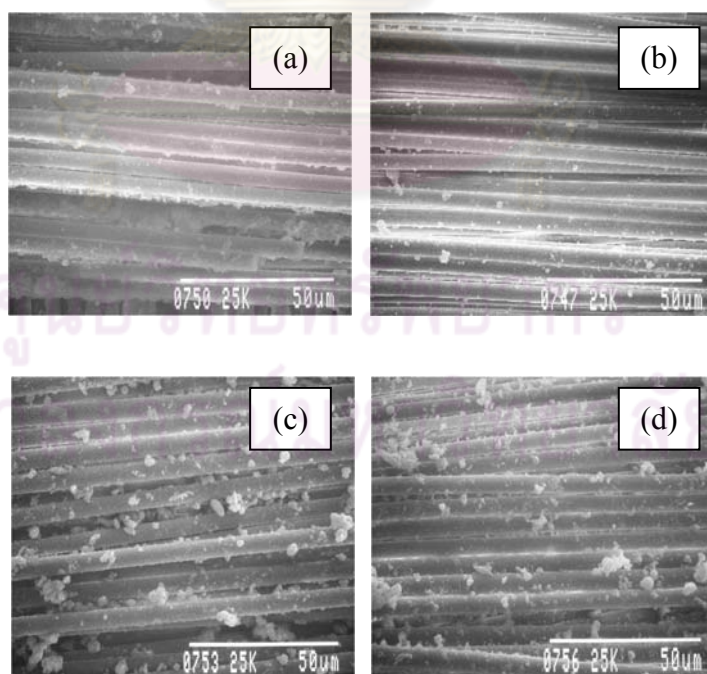


**Figure 4.11** SEM images of catalysts immobilized onto FGC: (a) TiO<sub>2</sub> P25, (b) Fe-TiO<sub>2</sub>, (c) V-TiO<sub>2</sub> and (d) W-TiO<sub>2</sub>.



#### 4.1.2.3 X-Ray Diffraction

The crystallinity of the metal-doped TiO<sub>2</sub> samples and P25 immobilized on FGC was identified by X-ray diffraction method as shown in Figure 4.12. The spectra reveal that both anatase and rutile phases exist in all samples from their dominant peaks at around 25.6° (anatase [101] plane) and 27.7° (rutile [110] plane) respectively. No new peaks associated with crystalline phases of the dopant oxides could be detected. This could be due to the fact that formation of dopant oxides is below the XRD detection limit or that the metal dopant ions are well substituted into the Ti ions due to their similar ionic radii (Ti<sup>4+</sup> = 74.5 pm, Fe<sup>3+</sup> = 78.5 pm, W<sup>6+</sup> = 74 pm, and V<sup>5+</sup> = 68 pm) (Shannon, 1976). Slight positive shift to higher angle was observed for the V- and W-doped samples which may indicate slight lattice shrinkage of some of the TiO<sub>2</sub> lattices caused by substitution of the dopants. A smaller negative shift to lower angle was also observed for the Fe-doped sample possibly due to the slightly larger ionic radii and the lower charges of the Fe<sup>3+</sup> compared to the Ti<sup>4+</sup>. The lattice deformation for the V- and W-doped samples is also in agreement with results from XANES measurements to be discussed in section 4.1.2.4.

Utilizing the Scherrer equation (Patterson, 1939), the average crystallite size of the two phases can be determined from broadening of the anatase and rutile peaks. The crystallite sizes as well as the anatase and rutile percentage are listed in Table 4.3. Our result shows that P25 contains approximately 4:1 anatase to rutile ratio in agreement with usual values cited in literature (Ohtani, Prieto-Mahaney, and Abe, 2010). The TM-doped TiO<sub>2</sub> samples were observed to have quite small crystallite sizes, suggesting that the transition metal dopants may retard the growth of TiO<sub>2</sub> crystalline phase as well as the transformation of anatase to rutile in accordance with several observations by others (Wang et al., 2003; Choi, Park, and Hoffmann, 2010). The large fraction of anatase to rutile should be beneficial to photocatalytic activity since the anatase phase has generally been shown have higher photocatalytic activity than the rutile phase (Fujishima and Zhang, 2006).

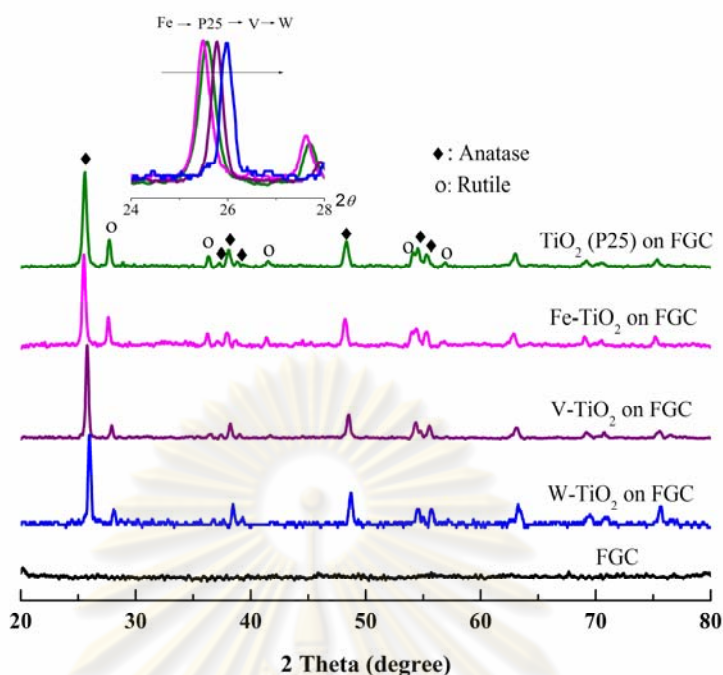


**Figure 4.12** XRD patterns (from bottom to top) of the FGC substrate, W-doped, V-doped, Fe-doped and pure TiO<sub>2</sub> (P25) immobilized on FGC. Peaks corresponding to the anatase and rutile phases of TiO<sub>2</sub> are marked by the solid diamond and open circle, respectively. The top insert plots the dominant anatase and rutile peaks from all samples on the same scale showing the V- and W-doped sample peaks to shift slightly to higher angles, while the Fe-doped sample peaks shift minimally to lower angles with respect to their corresponding peak positions in the pure TiO<sub>2</sub> (P25) sample.

**Table 4.3** Crystallite sizes and the anatase and rutile percentage of the catalysts.

Catalysts	Anatase: rutile	Crystallite size (nm) <sup>a</sup>
TiO <sub>2</sub> (P25)	83: 17	5
Fe-TiO <sub>2</sub>	81: 19	5
V-TiO <sub>2</sub>	90: 10	6
W-TiO <sub>2</sub>	87: 13	7

<sup>a</sup> determined from broadening of XRD peaks using Scherrer equation.

#### 4.1.2.4 XANES

The information about local coordination and transition states of atoms in the samples can be further gained from the X-ray absorption near-edge structure (XANES) spectra of the samples. Figure 4.5 shows the XANES spectra taken at the *K*-edge ( $s \rightarrow p$  transition) of Ti atoms.

The *K*-edge transition energies of all samples are at similar positions to that of the crystalline rutile and anatase  $\text{TiO}_2$  indicating that most Ti ions in these samples are in the same tetravalent  $\text{Ti}^{4+}$  state as that in the pure  $\text{TiO}_2$ . The pre-edge structures of the anatase and rutile phases have been attributed to the weak dipole-allowed transition of the core electrons (1s) to the hybridized 3d-4p orbital states (labelled as  $A_2$  and  $A_3$ ) or to the hybridized 4p-4s states (B), and the quadrupolar transition of 1s to 3d orbitals ( $A_1$ ) (Farges et al., 1997; Wu et al., 1997). Usually the degree of hybridization increases as the lattice loses its centre of symmetry or is distorted e.g. in going from octahedral to square pyramidal and tetrahedral lattices, resulting in higher intensity of the pre-edge structures. Previously, Farges et al. extensively categorized a range of Ti compounds for which Ti existed in various coordination states and showed that for  $\text{Ti}^{4+}$  in tetrahedral coordination ( $\text{TiO}_4$ ), the normalized intensity of the pre-edge structures was usually in the range of 0.7-1.0, while for those in the square pyramidal ( $\text{TiO}_5$ ) and octahedral ( $\text{TiO}_6$ ) coordination the pre-edge intensities were in the range of 0.4-0.7 and 0.05-0.4 respectively (Farges et al., 1997). The normalized pre-edge intensity of all samples here lie in the range of 0.1 to 0.4 signifying that the majority of Ti ions in these samples are in the  $\text{TiO}_6$  octahedral coordination.

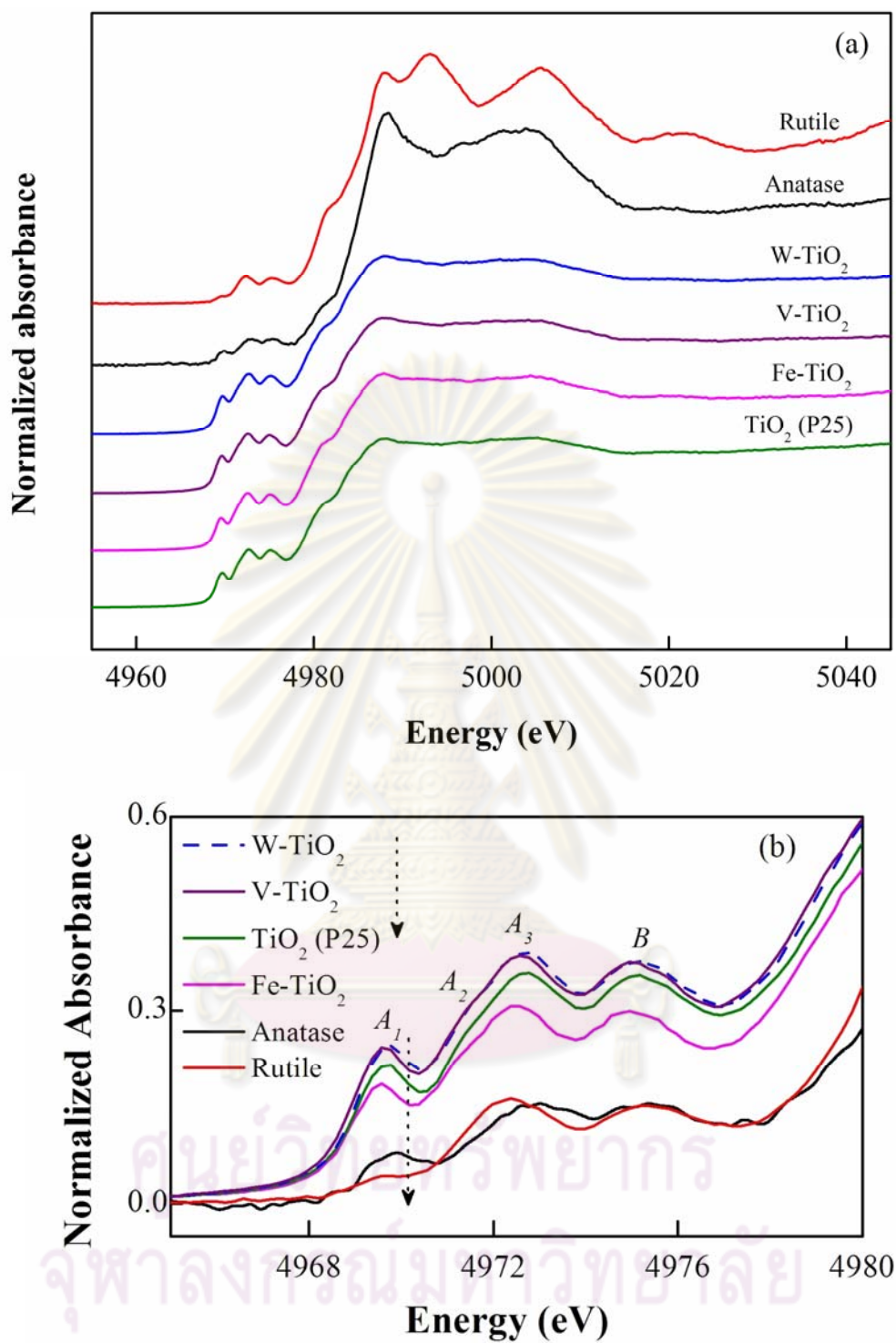


**Figure 4.13** (a) XANES spectra of the Ti K-edge in the prepared catalysts compared to those of the reference rutile and anatase TiO<sub>2</sub>, (b) Close-up of the pre-edge region in (a) overlaid on the same scale to depict changes in the pre-edge intensity. From top to bottom (indicated also by a guiding arrow): W-doped, V-doped, P25, Fe-doped, anatase and rutile TiO<sub>2</sub>.

A closer examination of the pre-edge intensities reveals that both the P25 and all TM-doped samples have higher pre-edge intensities than those of the pure anatase or rutile  $\text{TiO}_2$ . This indicates that Ti ions in the P25 and in the TM-doped samples are in the more distorted octahedral or less symmetrical environment than those in the pure crystalline rutile and anatase phases. There may be two reasons contributing to this. First, in the case of TM-doped samples, this is not surprising given that the TM dopants should cause some disorders in the  $\text{TiO}_2$  matrix especially if they are well dispersed into the  $\text{TiO}_2$  lattices and not segregated out as separate oxides. The V- and W-doped samples seem to show the highest increase in distortion in agreement with the XRD results that the two dopants caused the largest shift in the XRD peaks. The second factor is possibly due to the coexistence of both rutile and anatase phases in these samples as compared to the single rutile or anatase phase sample. It is well known that insufficient thermal treatment partially transforms the anatase into the rutile phase leading to coexistence of both the anatase and rutile phase in the same particle. This has been shown by several works on both P25 (Zhou et al., 2007), or other TM-doped  $\text{TiO}_2$  (Lee et al., 2009; Zhang et al., 2009) particles utilizing high-resolution TEM. The increased lattice disorder created at the boundary regions between the two phases should also contribute to the increase in the pre-edge intensity observed here.

The major features ( $A_1$ ,  $A_2$ ,  $A_3$  and B) of the pre-edge XANES were resulted from X-ray induced electronic transitions from the valence band to the conduction band (Hanley et al., 2002). Some researchers reported that the pre-edge of  $A_1$ ,  $A_2$ , and  $A_3$  are four ( $\text{TiO}_4$ ), five ( $\text{TiO}_5$ ), and six ( $\text{TiO}_6$ ) coordination (assigned 1s–4p transition), respectively (Luca, Djajanti, and Howe, 1998; Hsiung et al., 2006). By Gaussian–Lorentzian curve fitting, the relative compositions of  $A_1$ ,  $A_2$  and  $A_3$  for all doped sample and P25 are also given in Table 4.4. The XANES result of V- $\text{TiO}_2$  showed the highest rise to the pre-edge feature that possesses active species, indeed, a small pre-edge at  $A_2$  feature (Hsiung, Wang, and Lin, 2008). The pre-edge XANES spectra of Ti species compared between V- $\text{TiO}_2$  and  $\text{TiO}_2$  (P25) is shown in Figure 4.6.



**Table 4.4** Relative composition of A<sub>1</sub>, A<sub>2</sub>, and A<sub>3</sub> for TiO<sub>2</sub> (P25), Fe-TiO<sub>2</sub>, V-TiO<sub>2</sub>, and W-TiO<sub>2</sub>.

Catalysts	A <sub>1</sub>	A <sub>2</sub>	A <sub>3</sub>
TiO <sub>2</sub> (P25)	12	15	42
Fe-TiO <sub>2</sub>	10	20	35
V-TiO <sub>2</sub>	18	26	40
W-TiO <sub>2</sub>	19	25	38

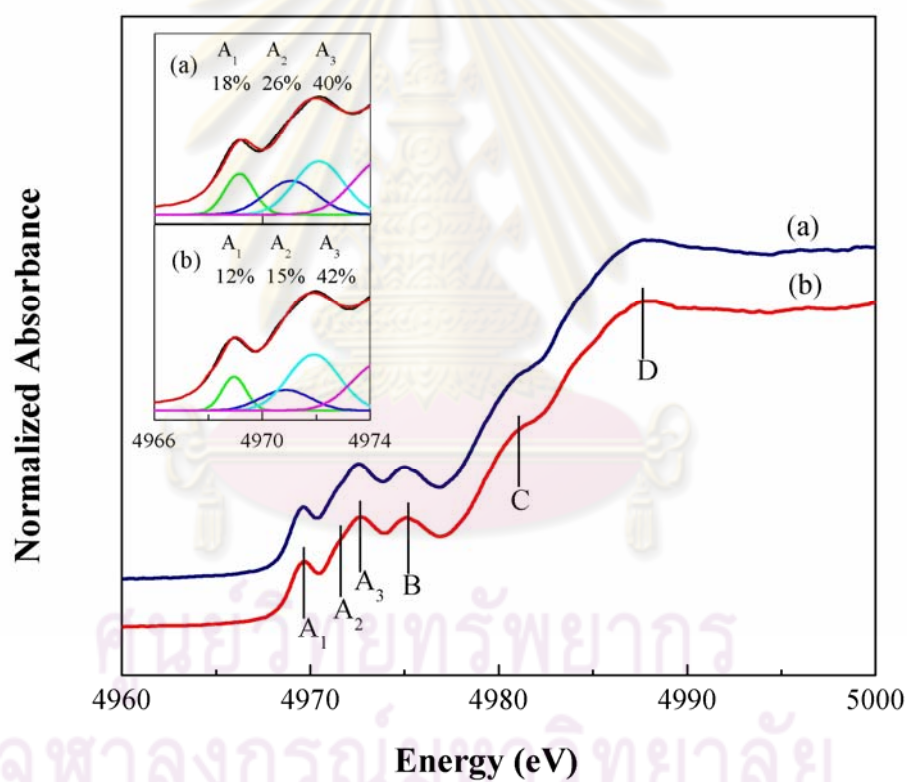


**Figure 4.14** Pre-edge XANES spectra of Ti species in the photocatalyst samples (a) V-TiO<sub>2</sub> and (b) TiO<sub>2</sub> (P25). The insert plots Gaussian-Lorentzian curve fitting of (a) and (b).

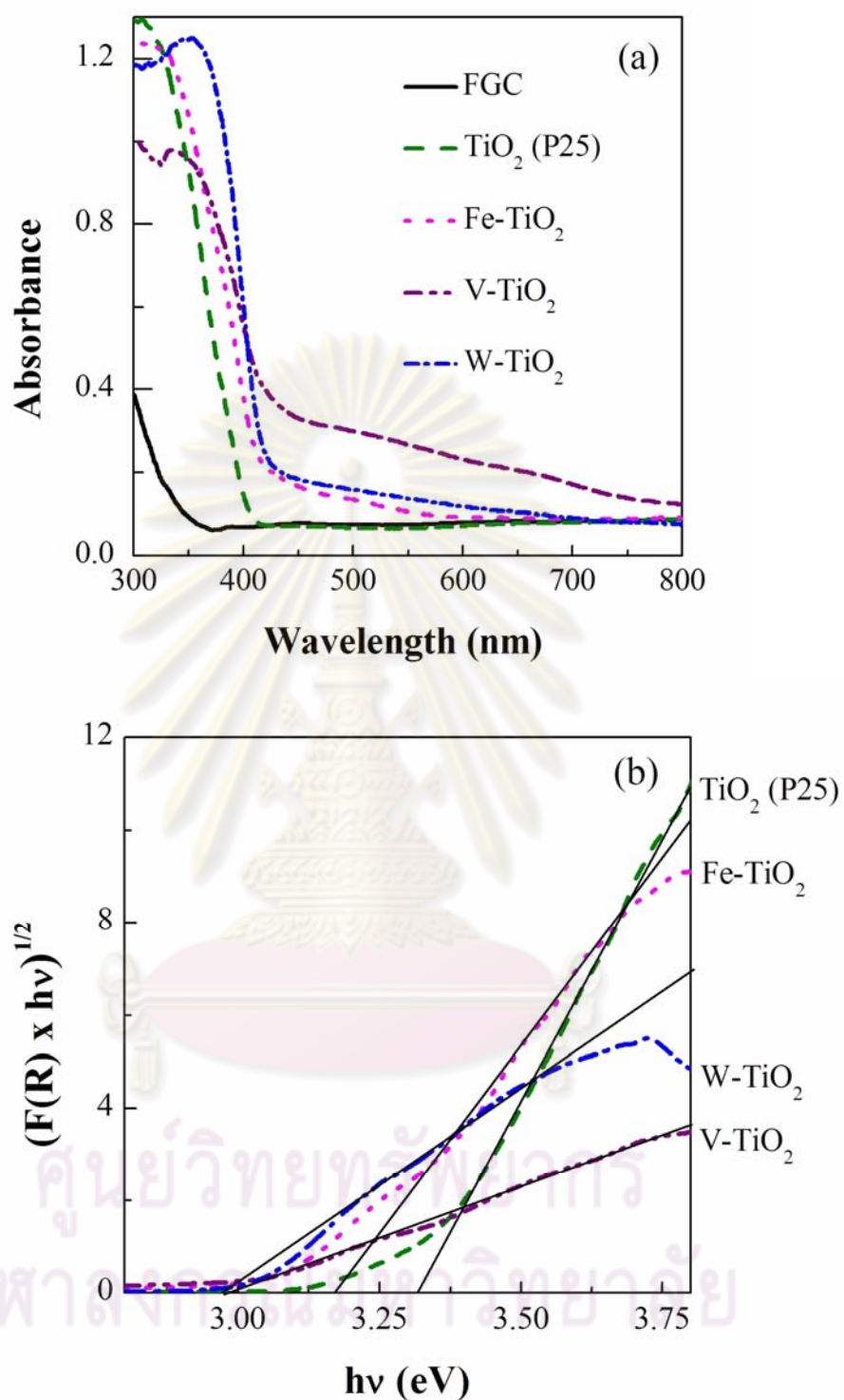
#### 4.1.2.5 UV-DRS and band gap measurement

Figure 4.15 (a) shows the UV-DRS measurement of all the TM-doped samples as well as the P25 coated onto FGC support. The absorption edges of all the doped samples are clearly shifted to the red compared to that of the pure TiO<sub>2</sub> (P25). The absorptions in the visible region ( $\lambda > 400$  nm) of all the doped samples are also higher than that of the pure TiO<sub>2</sub>. The V-doped sample shows the highest absorbance in the visible region followed by the W-doped and Fe-doped TiO<sub>2</sub> respectively. This trend correlates also with the visible-light photocatalytic performance of each catalyst discussed in the next section.

In order to determine the band-gap energy more accurately than that inferred from an absorption edge, the UV-DRS spectra were transformed using Kubelka-Munk method (Rao and Sahu, 2001). The resulting transforms are shown in Figure 4.15 (b). The intersection between the linear fit to the transformed curves and the energy axis yields the band-gap energies which correspond to 3.28, 3.14, 2.90, and 2.90 eV for the P25, Fe-, W-, and V-doped TiO<sub>2</sub> samples respectively. The band-gap energies can be used to determine the absorption edge wavelength as shown in Table 4.5. The absorption edge redshift as well as the increase in the visible region absorption of TiO<sub>2</sub> doped with transition metals is usually explained by the difference in energy levels between the dopants and the TiO<sub>2</sub> valence and conduction bands resulting in reduced photoexcitation energy and thus band-gap energy (Anpo et al., 2005).

**Table 4.5** Band-gap energy and absorption edge wavelength of the catalysts.

Catalysts	Absorption edge wavelength (nm)	Band-gap energy (eV)
TiO <sub>2</sub> (P25)	378	3.28
Fe-TiO <sub>2</sub>	395	3.14
V-TiO <sub>2</sub>	428	2.90
W-TiO <sub>2</sub>	428	2.90



**Figure 4.15** (a) UV-Vis DRS spectra of the prepared catalyst-coated FGC samples and (b) the Kubelka-Munk transformation of (a) in order to obtain band-gap energies of the prepared catalyst.

#### 4.1.2.6 PL

The PL emission spectra are useful to understand the fate of electron-hole pairs in semiconductor particles since PL emission results from the recombination of free carriers. The samples may absorb the photons with enough energy to generate electron-hole pairs, and the subsequent recombination of the photoexcited electrons and holes can release energy in the form of photoluminance (PL). Many reported that lower PL emission intensities might indicate lower recombination of electron-hole pairs (Li and Li, 2002; Cai et al., 2007). In this study, the PL emission spectra of pure  $\text{TiO}_2$  (P25) and V- $\text{TiO}_2$  are depicted in Figure 4.16. The PL emission intensities of pure  $\text{TiO}_2$  and V- $\text{TiO}_2$  exhibited peak values at approximately 425 nm corresponding 2.92 eV. Pure  $\text{TiO}_2$  sample demonstrated the highest PL emission intensity, indicating that electrons and holes were more easily recombined. The PL emission intensity was found to be decreased with the incorporation of  $\text{V}^{5+}$  into  $\text{TiO}_2$  lattice, possibly because the different redox energy levels of conduction and valence bands for V and  $\text{TiO}_2$  led to the charge transfer to inhibit the recombination of electron-hole pairs.

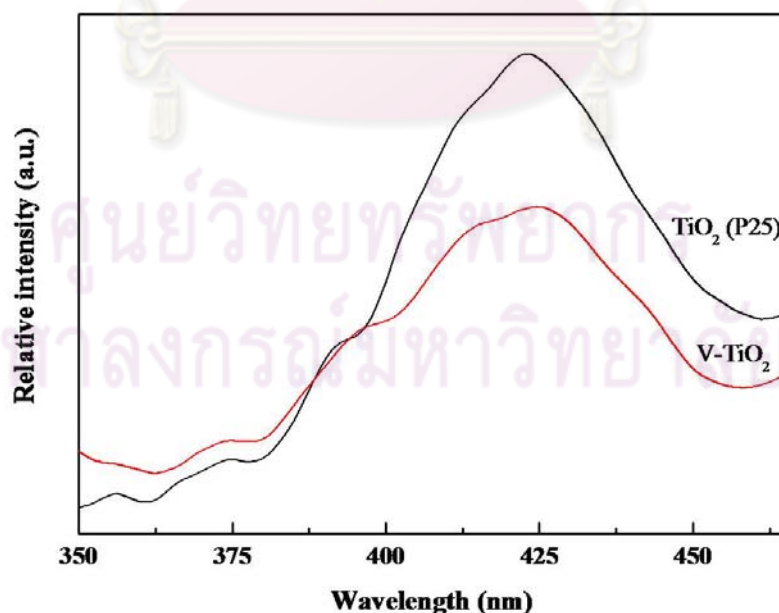


**Figure 4.16** Photoluminance spectra of pure  $\text{TiO}_2$  and V- $\text{TiO}_2$ .

## 4.2 Photocatalytic testing

### 4.2.1 Catalyst screening

The evaluation of photocatalytic activity was performed by analyzing the percentage removal of toluene under visible light at room temperature (25–27°C) in a batch reactor in order to find out for the best catalyst. The screening test was performed by analyzing the percentage removal of toluene across all the catalyst-immobilized on FGC samples. The operational condition used for all experiments were  $0.3 \pm 0.06$  mg/cm<sup>2</sup> of catalyst, 1000-1200 ppm of toluene concentration and 30% relative humidity (RH). The commercial TiO<sub>2</sub> (P25) was used as reference. It was found that the conversion of 21% was reached with the pure TiO<sub>2</sub> (P25), while the TM-doped catalysts exhibited a much higher performance. The conversion of 48%, 54% and 69% were reached with Fe-, W- and V-doped TiO<sub>2</sub> respectively. The results are shown in Figure 4.17.

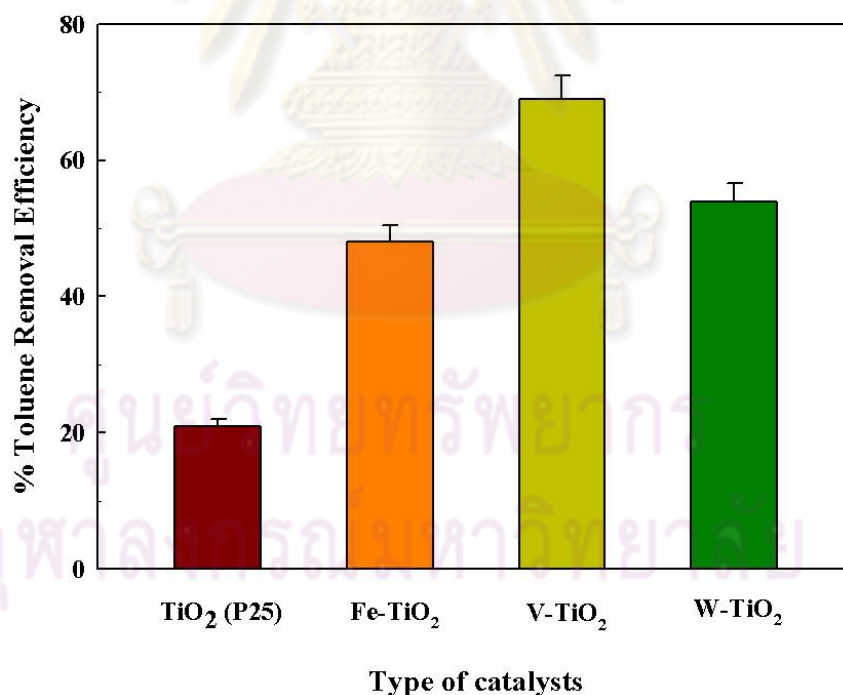


**Figure 4.17** Percent removal efficiency of gaseous toluene for each catalyst-coated FGC. After 120 minutes of visible light irradiation, the V-doped TiO<sub>2</sub> displayed the highest removal efficiency followed by the W-, Fe- and pure TiO<sub>2</sub>.



The increased catalytic activities seemed to correlate well with the order of increased visible light absorption of these catalysts (Figure 4.15) following the same order of P25 < Fe-doped < W-doped < V-doped TiO<sub>2</sub>. These TM dopants appear to increase the absorption in the visible region of TiO<sub>2</sub> and can thus better utilize photons in the visible range for photocatalytic reactions. We note that other factors such as the recombination rates (Paola et al., 2001) should also be important in deciding which dopant yields optimum performance but these are beyond our current investigation. From this result, V and W doped samples were selected for further catalytic activity study.

#### 4.2.2 Effect of W dopant on photodegradation of BTEX

For the evaluation of the photodegradation of BTEX in the air, the system was performed in continuous plug flow reactors. The W-TiO<sub>2</sub> was supplied to compare with commercial TiO<sub>2</sub> (P25). Figure 4.18 shows the photocatalytic BTEX removal as a function of time under a fluorescent day light lamp. The results revealed that the efficiency of BTEX removal over W-TiO<sub>2</sub> was higher than that of TiO<sub>2</sub>. The phenomena on removal of ethylbenzene and *o*-xylene with commercial TiO<sub>2</sub> (P25) were different from benzene and toluene. At the beginning of test; rapid removals were detected on ethylbenzene and *o*-xylene then gradually decreased with time and that after 150 min was achieved the steady state whereas benzene and toluene were fairly active at the beginning then continuously increased with time consumed toward 130 min, the reaction were reached a steady state. These results can be explained by adsorption behavior of pollutants. Ethylbenzene and *o*-xylene favor to adsorb on the active site of the surface, thus the fast observation on removal possibility due to the adsorption of ethylbenzene and *o*-xylene before degrading to final products via photocatalytic oxidation. In contrast, the phenomena on degradation of BTEX with W-TiO<sub>2</sub> were different. The degradations were increased with increasing of time (except for ethylbenzene due to nature of its) and approached to steady state at 150 min for benzene and toluene and 200 min for of ethylbenzene and *o*-xylene. This fact could suggest that the photocatalytic active site of TiO<sub>2</sub> was enhanced by W due to the retarding of electron-hole as explained in XANES result. Therefore, the photocatalytic oxidation rate of BTEX removal was listed in Table 4.6. The photocatalytic reaction rate was found in sequence of ethylbenzene > xylene > toluene > benzene.

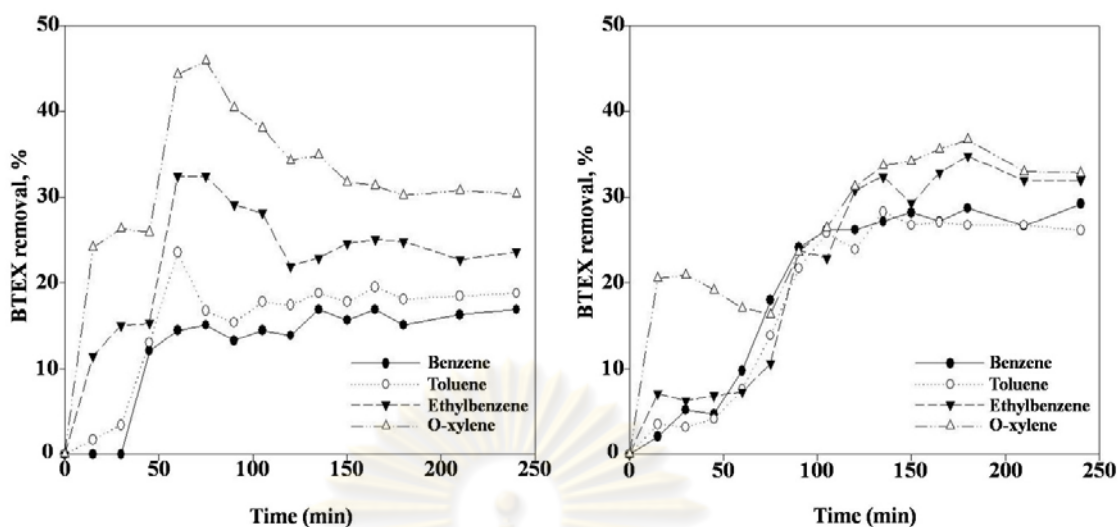


**Figure 4.18** Variation of the % BTEX removal with irradiation time using  $\text{TiO}_2$  (P25) and W- $\text{TiO}_2$ . Conditions: 30% RH, flow rate 60 ml/min, catalysts loading  $0.1 \text{ mg/cm}^2$ , day light lamp fluorescent 18 watt.

**Table 4.6** Comparison on efficiency rate of BTEX removal over W- $\text{TiO}_2$  and  $\text{TiO}_2$  (P25) immobilized on FGC.

Pollutant	Reaction rate of $\text{TiO}_2$ (P25) (ppm/g·s)*	Reaction rate of W- $\text{TiO}_2$ (ppm/g·s)*
Benzene	3	17
Toluene	7	23
Ethylbenzene	11	34
O-xylene	17	43

\* reaction rate 
$$-r_A = \frac{F_{A_0} \Delta x}{W}$$

where  $F_{A_0}$  molar feed flowrate  
 $\Delta x$  conversion difference  
 $W$  catalyst weight

#### 4.2.2.1 Effect of flow rate

The photocatalytic oxidation of BTEX over W-TiO<sub>2</sub> immobilized on FGC is shown in Figure 4.19. The reaction at flow rate 20 ml/min was achieved 100% BTEX removal whatever the pollutants due to a long residence time for reaction. The activity decreased with increasing of flow rate regarding to diffusion mass transfer (as a result at flow rate of 70 and 90 ml/min) and convective mass transfer (as a result at flow rate of 120 ml/min) phenomena (Dezhi et al., 2005). The effect of flow rate on the reaction rate of BTEX removal over W-TiO<sub>2</sub> immobilized on FGC is displayed in Table 4.7.

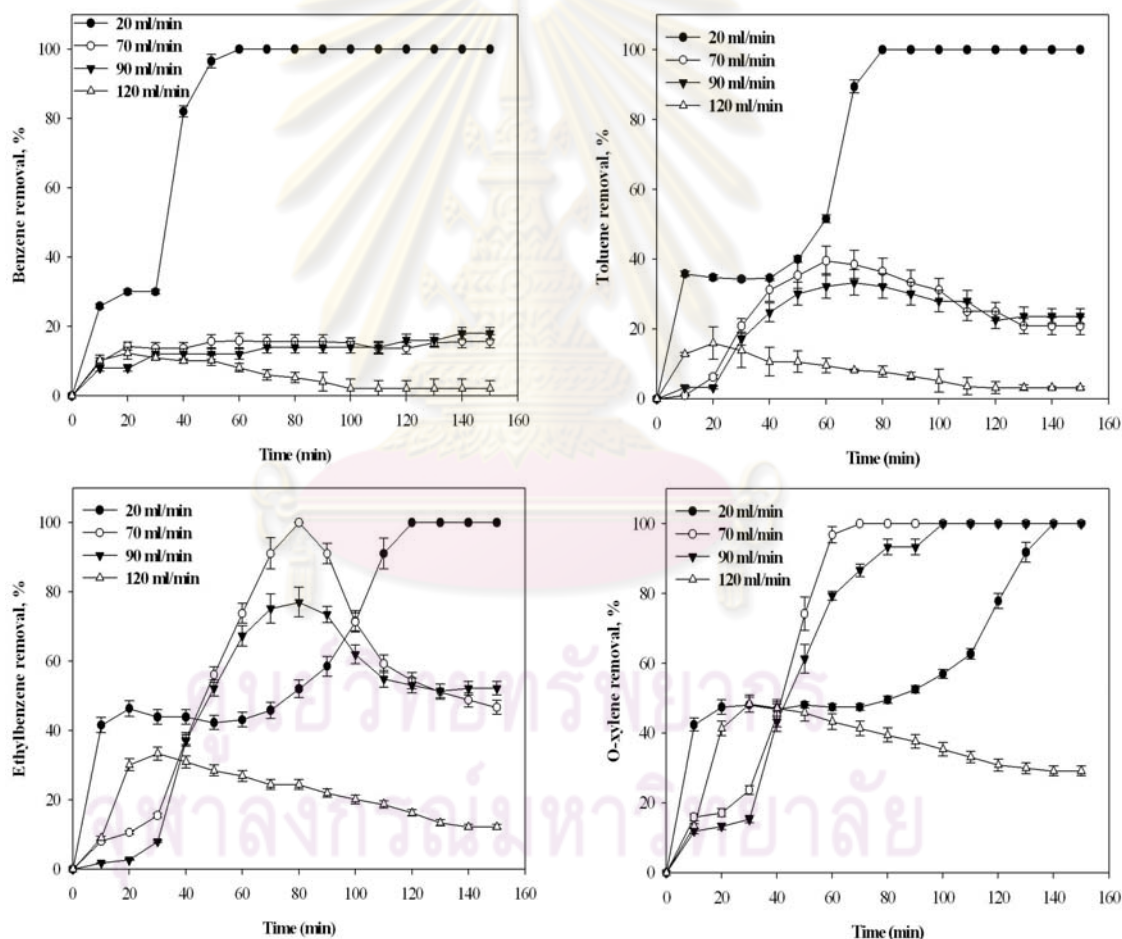


**Figure 4.19** Effect of flow rate on the % BTEX removal with irradiation time using W-TiO<sub>2</sub> immobilized on FGC. Conditions: 30% RH, catalysts loading 0.1 mg/cm<sup>2</sup>, day light lamp fluorescent 18 watt. Initial concentration: benzene = 86 ppm, toluene = 156 ppm, ethylbenzene = 168 ppm, *o*-xylene = 212 ppm.

**Table 4.7** Effect of flow rate on the reaction rate of BTEX removal over W-TiO<sub>2</sub> immobilized on FGC.

Flow rate (min/ml)	Reaction rate (ppm/g·s)			
	Benzene	Toluene	Ethylbenzene	<i>o</i> -xylene
20	0.87	1.58	1.74	2.19
70	0.49	1.31	3.00	7.60
90	0.55	1.42	3.25	9.34
120	0.10	0.30	1.28	3.61

#### 4.2.2.2 Effect of catalyst loading

The experimental data on percentage of BTEX removal for the different catalysts loading is shown in Figure 4.20. The results revealed that the efficiency of reaction was increased with increasing of catalyst loading due to the quantity of active sites of catalysts was increased. The efficiencies of reaction on photodegradation of BTEX are shown in Table 4.8. The results expressed that low catalyst loading displayed the highest catalytic ability on reaction. Suggesting that the catalyst loading affected the transparency of materials for light penetration through the system and large amount of catalysts seemed to obstruct and limit the penetration of light to all surfaces. Hence, low catalyst loading lead to high efficiency.

จุฬาลงกรณ์มหาวิทยาลัย

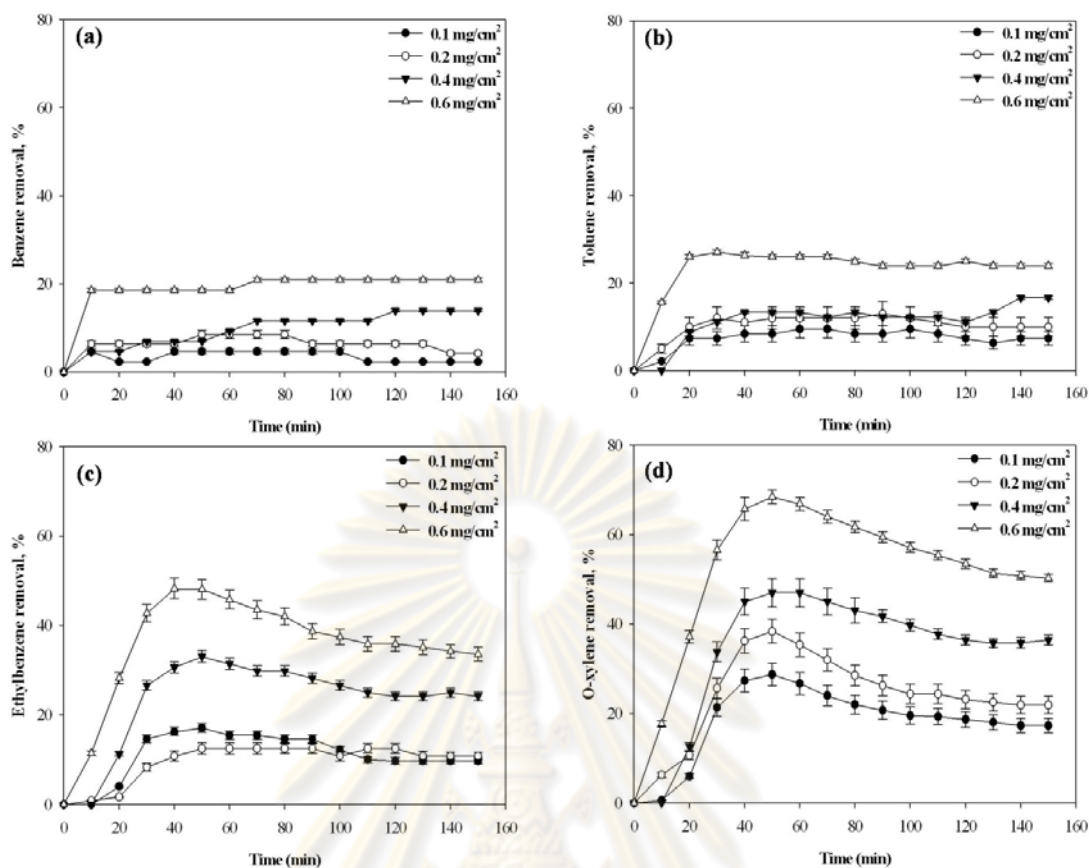


**Figure 4.20** Effect of catalyst loading on % BTEX removal with irradiation time over W-TiO<sub>2</sub>. Conditions: 30% RH, flow rate 60 ml/min, day light lamp fluorescent 18 watt. Initial concentration: benzene = 76 ppm, toluene = 156 ppm, ethylbenzene = 175 ppm, *o*-xylene = 220 ppm.

**Table 4.8** Effect of flow rate on the reaction rate of BTEX removal over W-TiO<sub>2</sub> immobilized on FGC.

Catalysts loading	Reaction rate (ppm/g·s)			
	Benzene	Toluene	Ethylbenzene	<i>o</i> -xylene
0.1 mg/cm <sup>-2</sup>	1.41	3.14	5.74	10.65
0.2 mg/cm <sup>-2</sup>	1.06	3.10	5.55	10.61
0.4 mg/cm <sup>-2</sup>	0.47	1.46	2.68	5.84
0.6 mg/cm <sup>-2</sup>	0.43	1.42	2.58	4.80



### 4.2.2.3 Effect of initial concentration

The influence of initial concentration on the degradation is shown in Figure 4.21. The results revealed two phenomena of removal. The first one was found on benzene and toluene removal and the second one was *o*-xylene and ethylbenzene. For benzene and toluene (Figure 4.21 (a) and (b), it was found that the removal was decrease with increasing initial concentration of pollutants. In contrast, for xylene and ethylbenzene, the trend of removal was increase with increasing initial concentration for a certain level and then drop at high initial concentration (Figure 4.21 (c) and (d), This trend is due to their behavior on adsorption ability. However, at a higher initial concentration the activity was drop due to the active sites were covered by an excess pollutants (Mo et al., 2009).

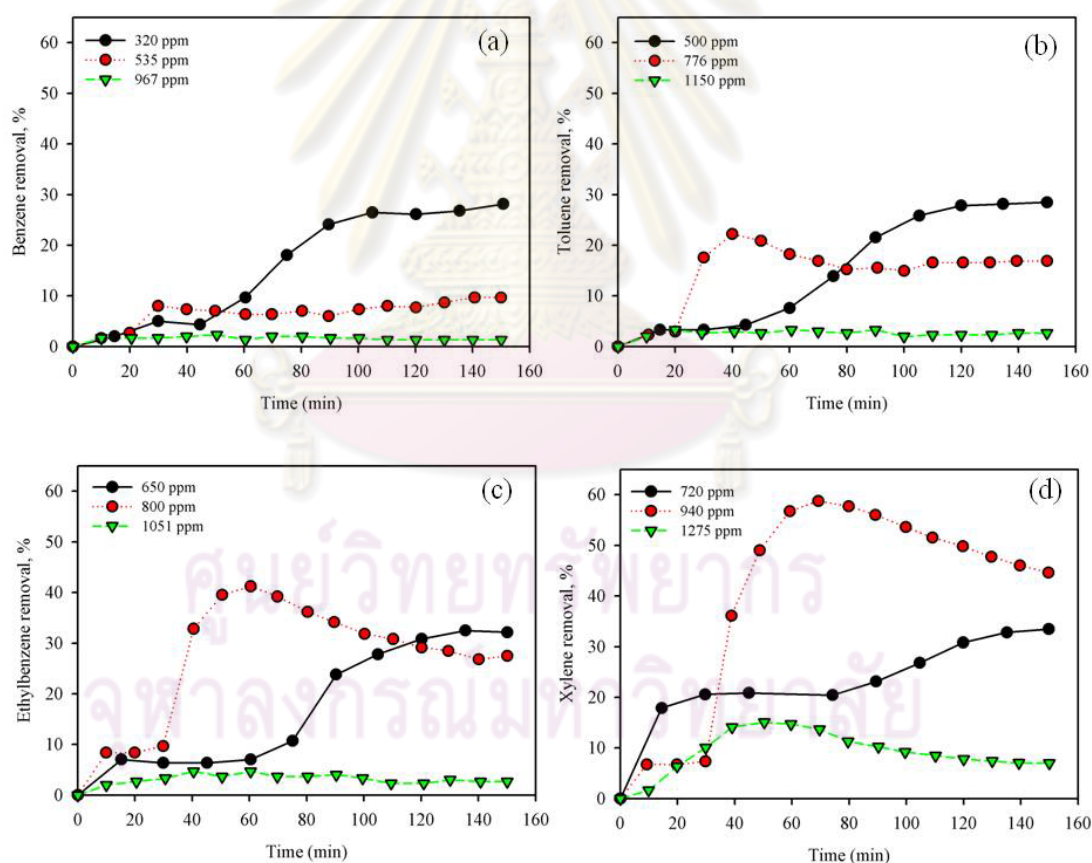


**Figure 4.21** Effect of initial concentration on the % BTEX removal with irradiation time over W-TiO<sub>2</sub> catalyst. Conditions: 30% RH, flow rate 90 ml/min, catalysts loading 0.1 mg/cm<sup>-2</sup>, day light lamp fluorescent 18 watt.

#### 4.2.2.4 Effect on relative humidity

The influence of relative humidity (RH) on the BTEX removal is shown in figure 4.22 and the reaction rate was listed in Table 4.9. The results illustrated that the BTEX removal was highest when the % RH was controlled to 30% RH. Under this condition, the reaction rate is favor to generate OH radical on the photocatalyst surface without limitation of OH radical lead to increase the reaction rate. When increasing the relative humidity to 40% or beyond, the reaction rate started to decreased due to the excess water was covered on the surface of catalyst and inhibited the adsorption of BTEX, resulting in low removal percentage (Obee and Hay, 1997).

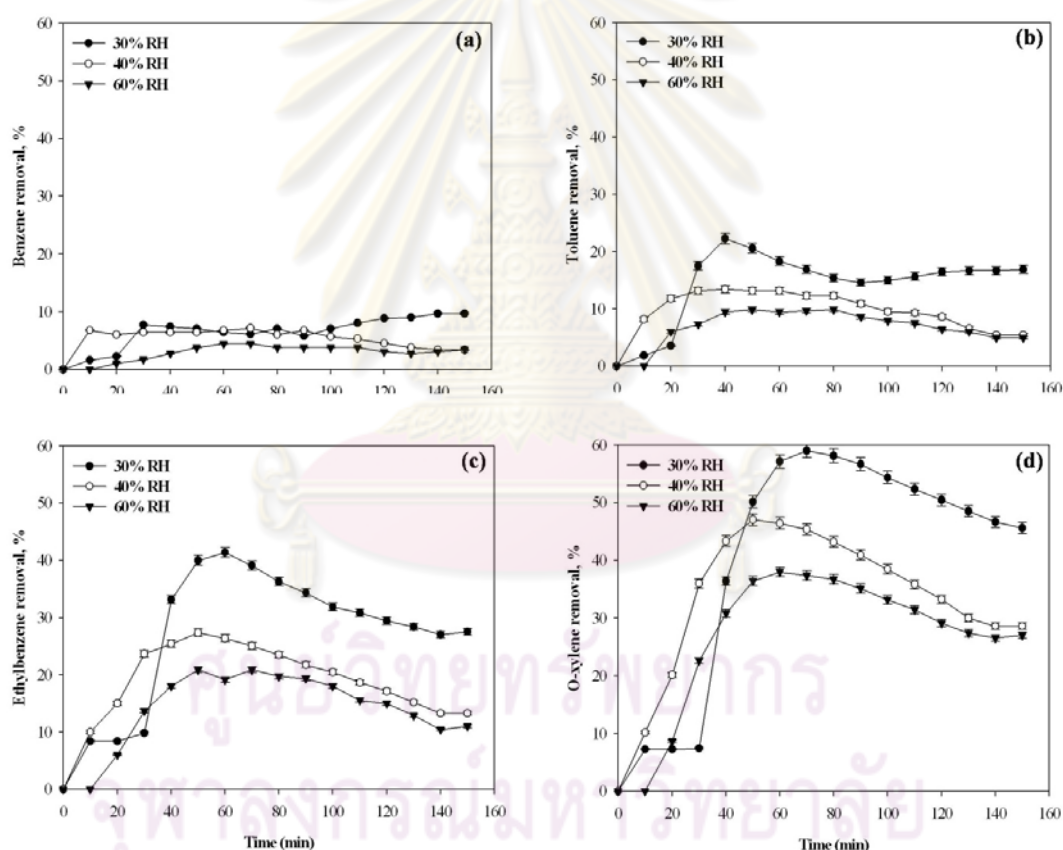


**Figure 4.22** Variation of the % BTEX removal with irradiation time using TiO<sub>2</sub> (P25) and W-TiO<sub>2</sub>. Conditions: Flow rate 90 ml/min, catalysts loading 0.1 mg/cm<sup>2</sup>, day light lamp fluorescent 18 watt. Initial concentration: benzene = 500 ppm, toluene = 760 ppm, ethylbenzene = 755 ppm, *o*-xylene = 900 ppm.

**Table 4.9** Effect of relative humidity on the reaction rate of BTEX removal over W-TiO<sub>2</sub> immobilized on FGC.

Relative humidity	Reaction rate (ppm/g·s)			
	Benzene	Toluene	Ethylbenzene	<i>o</i> -xylene
30 %RH	14.11	36.11	59.50	118.50
40 %RH	4.23	10.77	26.39	69.50
60 %RH	4.23	11.66	21.61	60.15

### 4.2.3 Effect of V dopant on photodegradation of BTEX

#### 4.2.3.1 Degradation of BTEX single compound

The V-doped TiO<sub>2</sub> was selected for degradation tests across other BTEX gases in a batch system. The removal efficiency tests of each BTEX gas by the V-doped TiO<sub>2</sub> were performed with the initial concentrations of 862±4, 1163±12, 785±6, and 965±5 ppm for the benzene, toluene, ethylbenzene, and xylene gases, respectively. The results depicted in Figure 4.23 revealed that the *o*-xylene gas was removed most efficiently followed by the ethylbenzene, the toluene and the benzene gases. This trend seems to correlate well with the gas-phase ionization potential of each BTEX gas which increases from *o*-xylene (8.56 eV) to ethylbenzene (8.77 eV) to toluene (8.83 eV) and benzene (9.24 eV). Benzene has the highest IP and thus the most difficult species to be oxidized (National Institute of Standards and Technology Chemistry WebBook: online). This is probably due to the fact that benzene structure is chemically more stable than that of others.

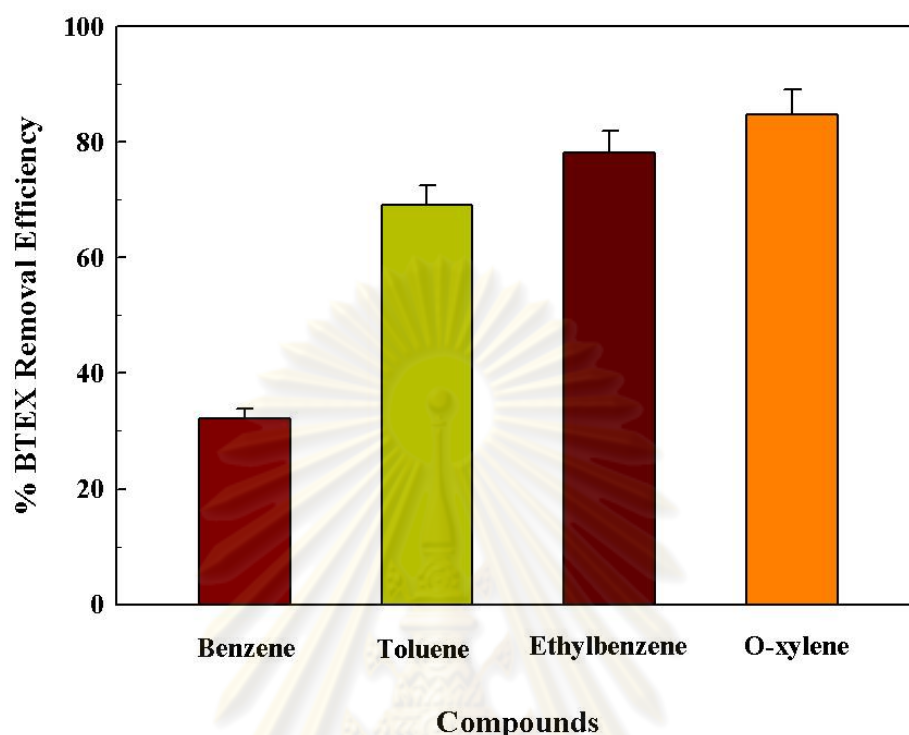


**Figure 4.23** Percent removal efficiency of each BTEX gas by the V-doped TiO<sub>2</sub>. From the lowest removal efficiency to the highest: benzene, toluene, ethylbenzene, and *o*-xylene.

#### 4.2.3.2 Degradation of mixed BTEX

Since the BTEX compounds are present as a composite mixture in environment, the extent of degradation of such a composite mixture were studied. The evaluation of photocatalytic activity of mixed BTEX contaminated air using V-TiO<sub>2</sub> was performed under the same condition as the degradation of each BTEX single pollutant separately. The commercial TiO<sub>2</sub> (P25) was also used as reference. As shown in Figure 4.24, it was found that in the absence of catalyst (uncoated FGC) about 2% of BTEX 228±47 ppm was degraded under irradiation of 120 min. In the process of decomposing by V-TiO<sub>2</sub>, only about 18% of benzene was eliminated upon 120 min-on-irradiation, suggesting that benzene was of those compounds that were difficult to be degraded through photocatalysis. And that, the addition of photocatalyst could remarkably accelerate the removal rate, more than 65% of toluene vapor and

80% of ethylbenzene and *o*-xylene were eliminated upon 120 min-on-irradiation. For TiO<sub>2</sub> (P25), the activity also followed the same trend with the conversion of 12%, 18%, 24% and 27% for benzene, toluene, ethylbenzene and *o*-xylene, respectively. This trend seems to correlate well with the gas-phase ionization potential (IP) of each BTEX gas since Benzene has the highest IP and thus the most difficult species to be oxidized. Comparing between V-TiO<sub>2</sub> and P25, the increased catalytic activities seem to correlate well with the increased visible light absorption of catalyst. In addition, it is very likely that A<sub>2</sub> contributes to the major photocatalytic activity for photodegradation of BTEX since the A<sub>2</sub> species were enriched on surfaces of V-TiO<sub>2</sub> (Table 4.4 and Figure 4.14).

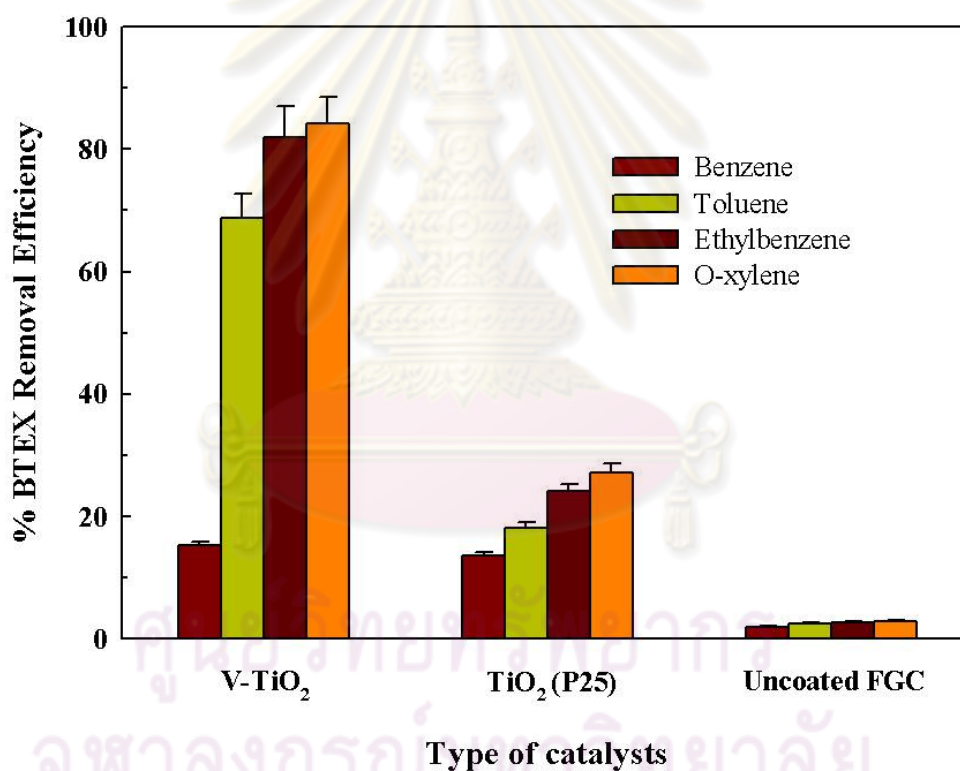


**Figure 4.24** Percent removal efficiency of mixed BTEX gases by V-TiO<sub>2</sub>, TiO<sub>2</sub> (P25) and uncoated FGC.

Due to a variety of VOCs occurring in environment, different organic compounds have been tested and they usually exhibit different photodegradation efficiency. Table 4.10 presents the results on various photocatalytic oxidation processes for BTEX. It was found the similarity that almost all studies used UV as a



light source, undoped-TiO<sub>2</sub> as the photocatalyst but the pollutant concentration and % RH were different. In this study, we enhanced photocatalytic properties of TiO<sub>2</sub> by V doping and tested for BTEX gases decomposition under visible light.

**Table 4.10** BTEX degradation on various photocatalytic oxidation processes.

Condition	Catalyst	Degradation Efficiency (%)	Reference
UV (365 nm) Dry air BTX: 15, 60, 42 ppb	TiO <sub>2</sub> 20 g m <sup>-2</sup>	B = 33 T = 75 X = 50	Pichat et al., 2000
UV (black light) 50% RH BT: 514 , 499 ppm	TiO <sub>2</sub> P25	B = 9 T = 57	Einaga et al., 2002
UV (black light) 10-80% RH BEX: 20 - 90 ppb	TiO <sub>2</sub> P25 0.5 mg.cm <sup>-2</sup>	100	Jo et al., 2002
UV (365 nm) 50-70% RH BTEX: 20 ppb	TiO <sub>2</sub> P25 on activated carbon filter	> 60	Ao et al., 2003
fluorescent day light lamp ( $\lambda_{\max} \sim 425$ nm) 30% RH BTEX: 228±47 ppm	V-TiO <sub>2</sub> 0.3 mg.cm <sup>-2</sup>	B = 15 T = 68 E = 81 X = 84	This work

The influence of operational conditions was also studied in the process of mixed BTEX degradation using V-TiO<sub>2</sub> by comparing percentage removal of mixed BTEX between low concentration (228±47 ppm) and high concentration (644±39 ppm) in the presence of water vapor. The water vapor was measured as percent relative humidity (%RH) and set into two conditions; low RH (30-40% RH) and high RH (70-80% RH). The percentage removal of mixed BTEX using V-TiO<sub>2</sub> in all experiment is shown in Table 4.11.

**Table 4.11** Percent removal efficiency of mixed BTEX gases using V-TiO<sub>2</sub> under different condition.

Compound	Experimental condition		
	Low RH	High RH	
Low concentration (228±47 ppm)	Benzene	15.19±0.61	6.12±2.45
	Toluene	68.75±4.03	17.28±4.2
	Ethylbenzene	81.94±5.12	15.25±3.33
	O-xylene	84.25±4.21	23.20±2.1
High concentration (644±39 ppm)	Benzene	6.36±1.07	3.11±0.9
	Toluene	49.09±3.28	7.67±2.44
	Ethylbenzene	59.40±4.93	20.92±4.67
	O-xylene	66.66±3.69	23.68±1.75

#### 4.2.3.3 Effect of initial concentration

The photocatalytic activity of V-TiO<sub>2</sub> with different initial concentrations was studied under two conditions of relative humidity. The results as shown in Figure 4.25 revealed that the lower initial mixed BTEX concentration results in a higher removal efficiency of V-TiO<sub>2</sub>. The efficiency followed the same trend for both low and high initial concentration however, was more significant than that observed in high relative humidity (70-80% RH). From the lowest to the highest are benzene, toluene, ethylbenzene, and *o*-xylene, respectively. The higher catalytic activities of low initial concentration seemed to correlate with the active sites on the catalyst surface. It was observed that the increase of initial concentration cause a decrease of photocatalytic activity of V-TiO<sub>2</sub>. This can be explained by the adsorption

ability of the remaining constant of active sites on V-TiO<sub>2</sub> surface (Obee and Brown, 1995; Yu and Brouwers, 2009).

#### 4.2.3.4 Effect of relative humidity

The effect of water vapor on the removal efficiency of mixed BTEX was investigated by applying the different %RH to a fixed concentration of mixed BTEX. The humidity could enhance or reduce the photocatalytic activity depending on the reactant and the H<sub>2</sub>O concentration range (Jacoby et al., 1995). In general, the presence of water vapor in photocatalytic reactions is considered to be essential because water molecules react with the holes to produce hydroxyl radicals (OH<sup>•</sup>).

In this study, high RH (70-80% RH) negatively affected the photocatalytic removal efficiency of mixed BTEX. At low RH (30-40% RH) condition, it seems to be a sufficient source of OH<sup>•</sup>. Therefore, the BTEX removal efficiency of V-TiO<sub>2</sub> at low RH condition was higher than that of high RH condition either at low or high initial concentration. The results are shown in Figure 4.24. Similar effect for BTEX mixture compounds (Ao et al., 2003; Ao and Lee, 2004) and toluene (Fresno et al., 2008; Kuo, Wu, and Hsu, 2009) has been reported. In addition, the conversion of xylene increased when the feed gas contained a sufficient amount of H<sub>2</sub>O (Tseng et al., 2009). This finding can be explained by considering that under higher RH the water molecules might compete with the BTEX molecules on the catalyst surface sites during adsorption (Wang et al., 1998) and gradual accumulation of water vapor molecule on the surface of catalyst can block BTEX adsorption sites. Therefore, the BTEX removal efficiency of V-TiO<sub>2</sub> decreased with increasing water vapor (Pichat, 2010).

จุฬาลงกรณ์มหาวิทยาลัย

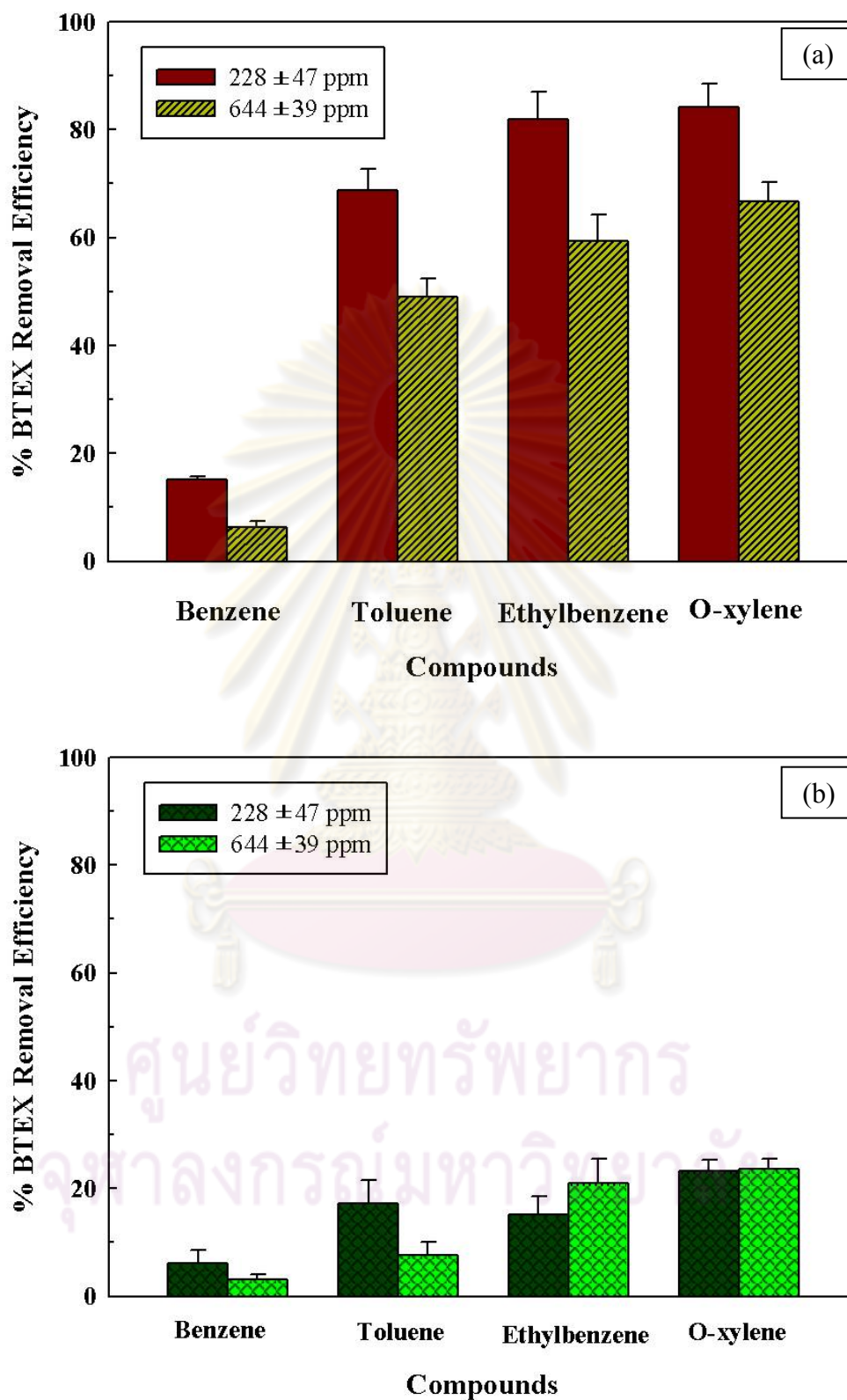


**Figure 4.25** Percent removal efficiency of low and high concentration mixed BTEX by the V-TiO<sub>2</sub> under (a) 30-40 %RH and (b) 70-80 %RH.

Based on the results of the photocatalytic degradation of BTEX, the BTEX photodegradation mechanism under the visible light irradiation in the presence of water molecules can be proposed. The mechanism included four pathways, as shown in Figure 4.26. The electrons in V-TiO<sub>2</sub> valence band were excited by the visible light and moved to conduction band. Path 1 shows H<sub>2</sub>O on the surface of V-TiO<sub>2</sub> reacted with the holes and formed hydroxyl radicals (OH<sup>•</sup>), the main cause of the photodecomposition of BTEX (Hoffmann et al., 1995). Path 2 displays electrons in the conduction band reacted with the surface adsorbing O<sub>2</sub> molecules to yield O<sub>2</sub><sup>•-</sup> radicals. Subsequently, the O<sub>2</sub><sup>•-</sup> radicals also reacted with H<sub>2</sub>O on the surface resulting in forming of OH<sup>•</sup> (Gaya and Abdullah, 2008). Path 3 the V<sup>5+</sup> on the surface of TiO<sub>2</sub> acted as electron trap (Choi et al., 1994). The photogenerated electrons could be transferred to the lower-lying conduction band of V<sup>5+</sup> becoming V<sup>4+</sup> species. While the positive holes moved toward the valence band of TiO<sub>2</sub> and accumulated there involving in path 1 and resulting in reduction of the electron-hole recombination. The V<sup>4+</sup> could transfer an electron to oxygen molecules to yield O<sub>2</sub><sup>•-</sup> radicals turned to V<sup>5+</sup>. Consequently, path 4 photocatalytic activity of BTEX occurred by OH<sup>•</sup>.

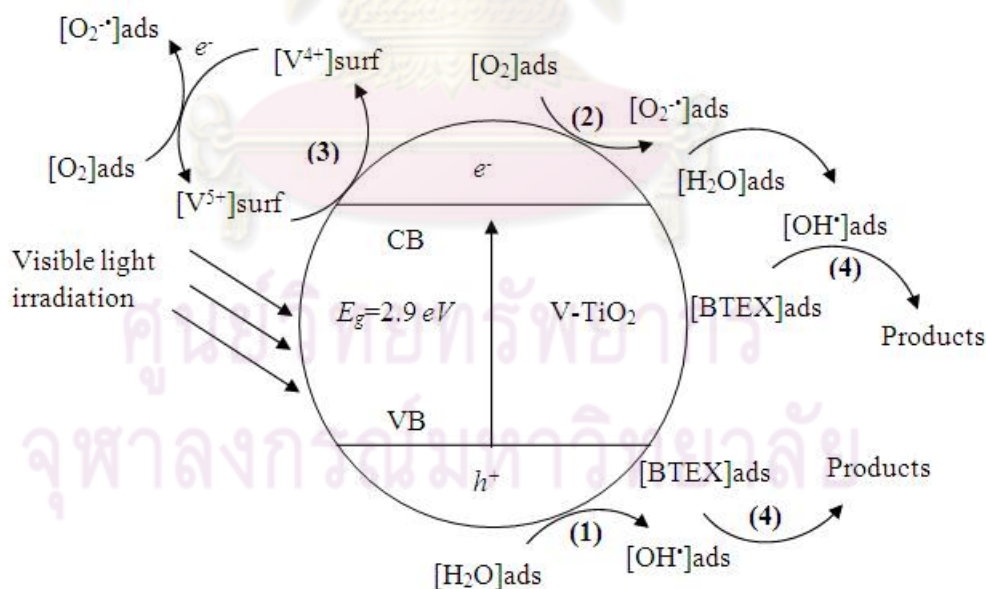


**Figure 4.26** proposed mechanism of BTEX decomposition over V-TiO<sub>2</sub> photocatalyst under visible light irradiation.



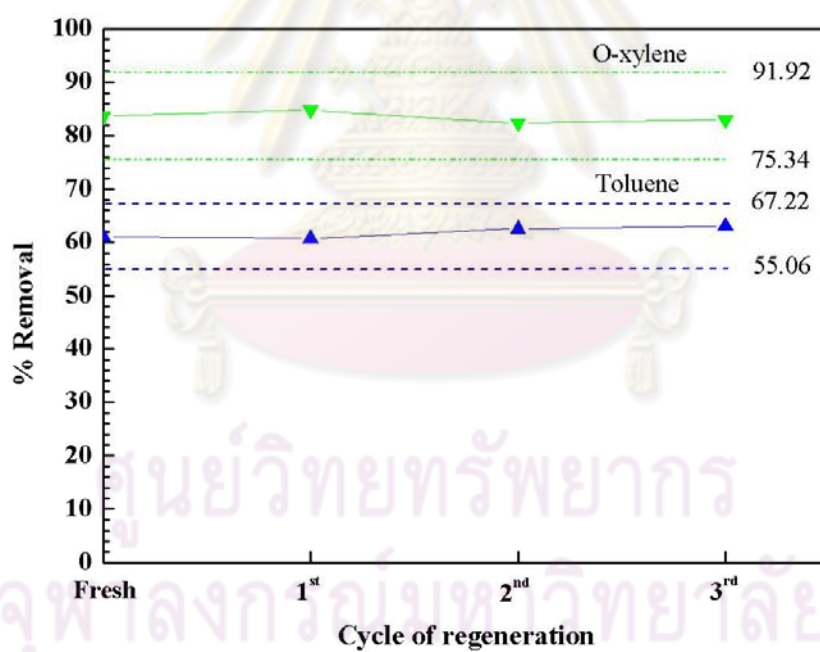
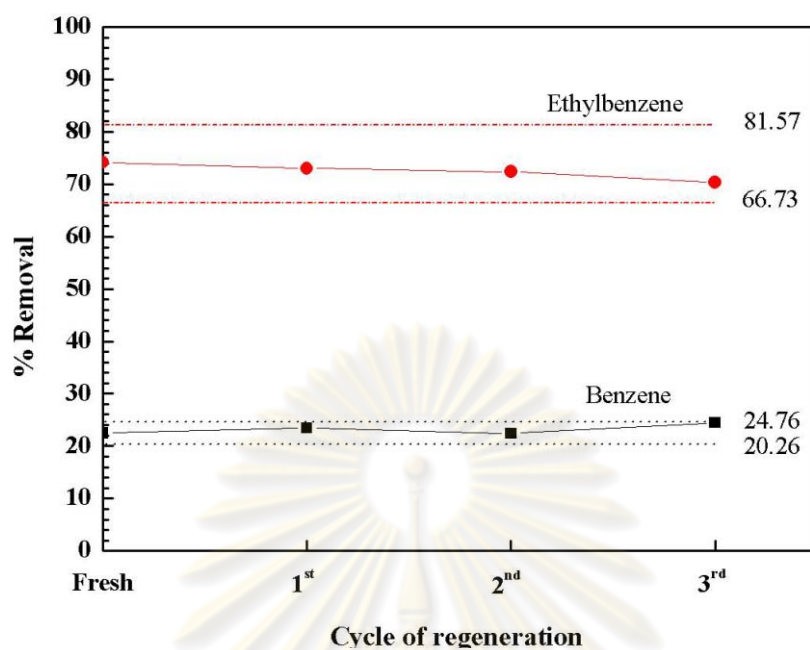
#### 4.2.3.5 Reliability of V-TiO<sub>2</sub>

In order to test the reliability of catalyst, the used V-TiO<sub>2</sub> on FGC was reused twice. Before the reuse, it was regenerated by the calcination at 450°C for an hour and 100 hours with the heating rate of 2°C/min, respectively. For comparing the regenerated catalyst ability, the regenerated catalysts were used to treat BTEX under the same conditions, except the testing time. The cycles of regeneration were presented in a diagram as shown in Figure 3.4. The calcination temperature was set in longer period of time in order to prove the severe condition. As well as the reaction time was set longer to 10 hours. Since the deactivation on photocatalytic reaction is difficult to be observed, the severe test was carried out in order to reduce the time consuming for a long period of time. The system was set up similar to Nagel et al. (2004). The authors also used the severe condition to accelerate the life testing.

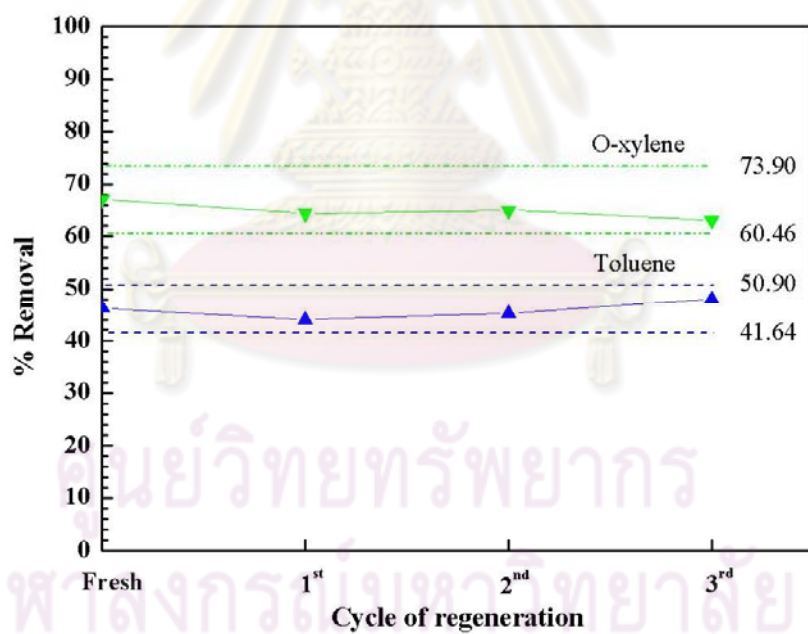
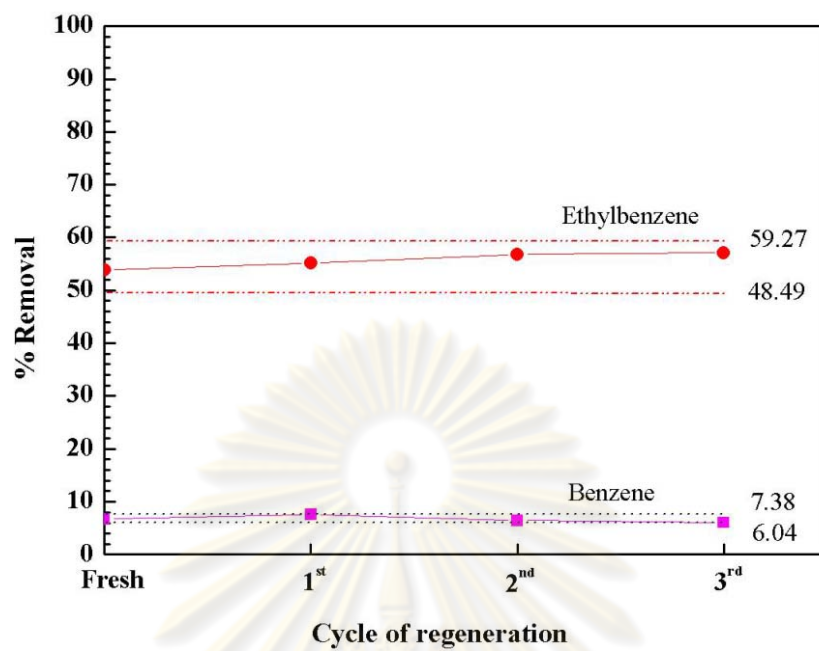
In this study, the acceptable conversion (BTEX removal efficiency) level was set  $\pm 10\%$  from the original performance. However, the setup level may not be applicable to the original low conversion, since it will provide small room for the fluctuation.

Figure 4.27 and 4.28 are the performance of reused catalysts, respected to single substance in feed and mixed gas in feed, respectively. According to the results showing of each BTEX (Figure 4.27), the % removals on each cycle were still within  $\pm 10\%$  the acceptable range from the original fresh performance. The highest range (up to 8%) belongs to benzene, while other chemicals presented their differences in  $\pm 5\%$ . This was due to low conversion for the fresh performance on benzene as explained previously.

ศูนย์วิทยทรัพยากร  
จุฬาลงกรณ์มหาวิทยาลัย



**Figure 4.27** Performance of reused catalysts for single BTEX in feed.



**Figure 4.28** Performance of reused catalysts for mixed BTEX in feed.

From the appearance of used V-TiO<sub>2</sub> on FGC as shown in Figure 4.29, it was no evidence of carbonaceous deposit on the supported catalyst. The V-TiO<sub>2</sub> immobilized on FGC could be repeated in the process at least three times. In conclusion, reliability is acceptable, resulting in the feasibility of using the prepared catalysts.

The study on the catalyst reliability was investigated further on the mixed-compounds of BTEX. The results as shown in Table 4.12 are reasonably acceptable to the catalyst durability. Variations on most tests (-6.45 – +5.63 %) were not excluded from the acceptable range ( $\pm 10\%$  compared to fresh catalyst performance). Only the test on benzene degradation was out of the specific range. The variation was of high ( $\pm 11\%$ ). This was due to a low initial concentration of benzene being used. Repeatedly, there was no black spot on the V-TiO<sub>2</sub>/FGC, referring to no carbonaceous deposition. The degradation of spent catalyst was not observed in both agglomeration of hydrocarbons and sintering from high temperature during the catalyst regeneration.

**Table 4.12** Percent removal of mixed BTEX gases using the regenerated V-TiO<sub>2</sub> and percent variation of each cycle.

Compound (ppm)	Fresh	% removal of each cycle (% variation)		
		1 <sup>st</sup>	2 <sup>nd</sup>	3 <sup>rd</sup>
Benzene (297 $\pm$ 3)	6.71	7.56 (+11.29)	6.43 (-4.37)	6.01 (-11.63)
Toluene (516 $\pm$ 15)	46.27	44.03 (-5.07)	45.23 (-2.30)	48.07 (+3.75)
Ethylbenzene (557 $\pm$ 8)	53.88	55.14 (+2.28)	56.82 (+5.16)	57.10 (+5.63)
O-xylene (508 $\pm$ 15)	67.18	64.42 (-4.28)	65.02 (-3.32)	63.11 (-6.45)



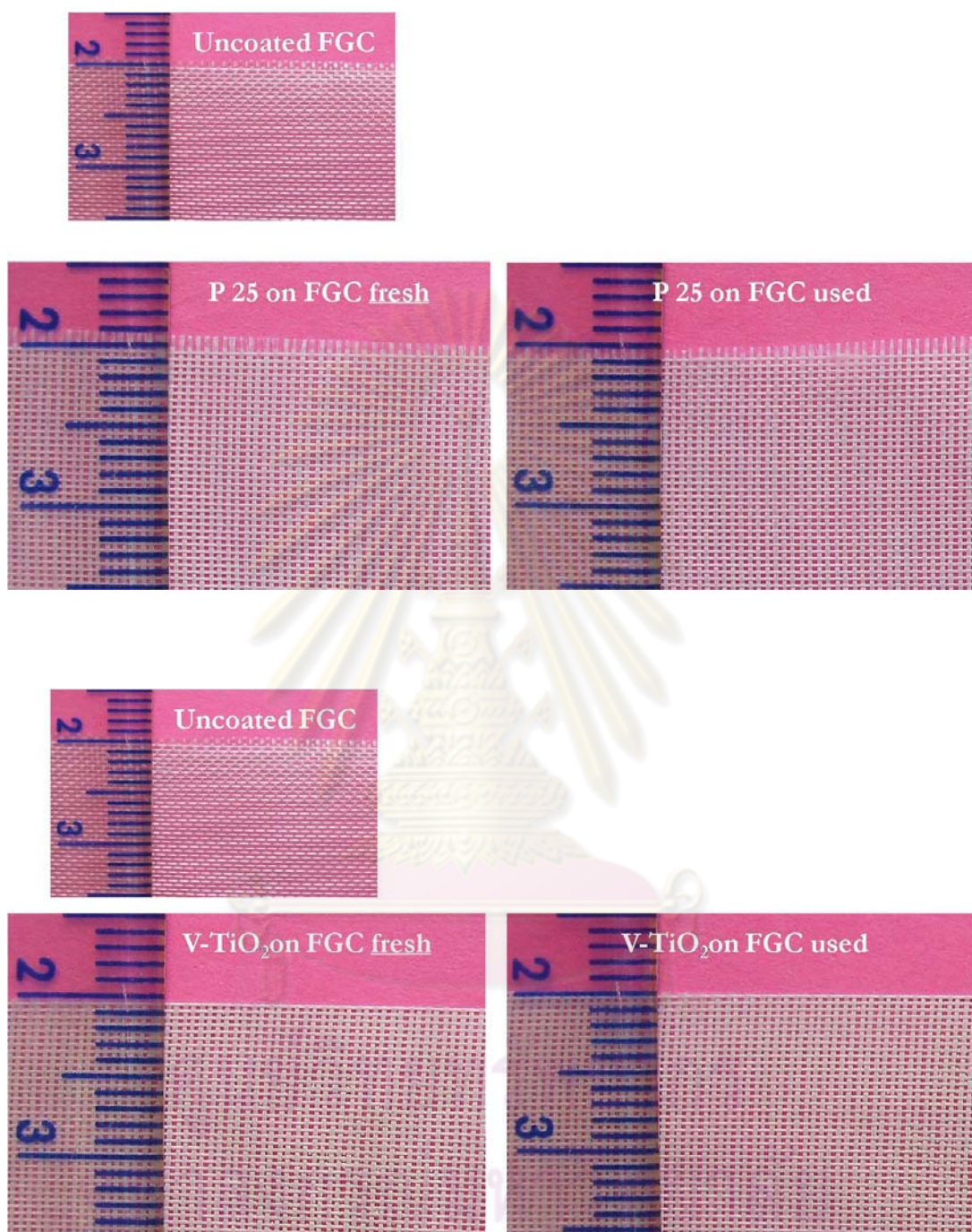


**Figure 4.29** Fresh and spent catalyst supports.



### 4.3 Current

The photodegradation is an electric-energy-intensive process. Accordingly, a figure-of-merit of the process based on electric energy consumption should be evaluated. Reactor efficiencies can be evaluated for the photocatalytic conversion of both water and air pollutants using a number of efficiency factors such as the Electrical Energy per Order ( $E_{EO}$ ), the quantum yield, the quantum efficiency and the photocatalytic thermodynamic efficiency factor.

For quantum yield and quantum efficiency, they are two parameters of significant value in photocatalysis. In principle, these parameters should be defined with the photons absorbed by the mesh-TiO<sub>2</sub> system. In cases where there is no available data of back-reflected and forward-scattered photons, an apparent Electrical Energy per Order (EE/O) may be considered. Recently the IUPAC has proposed the parameter for advanced oxidation processes (AOP) on the use of electrical energy. For the case of low pollutant concentration, the electrical energy per order ( $E_{EO}$ ) is defined as the amount of electricity (kWh) required minimizing the concentration of a pollutant by 1<sup>st</sup> order of magnitude in every 1 m<sup>3</sup> of contaminated water. The  $E_{EO}$  (kWh/m<sup>3</sup>/order) can be calculated from the following Eq. 4.1:

$$E_{EO} = \frac{Pt1000}{V \log\left(\frac{C_o}{C}\right)} \quad (4.1)$$

The Eq. 4.1 can be arranged in linear form as follows in Eq. 4.2.

$$\log\left(\frac{C}{C_o}\right) = -\frac{1}{E_{EO}} \frac{Pt1000}{V} \quad (4.2)$$

where  $P$  is the power (kW) to the AOP system,  $t$  is the irradiation time (hour),  $V$  is the volume (L) of the contaminated air in the reactor,  $C_o$  and  $C$  are the initial and final contaminated air concentrations.  $E_{EO}$  can be calculated from the negative inverse slopes of the plot of  $\frac{C}{C_o}$  versus visible dose  $\left(\frac{Pt1000}{V}\right)$  in the semilog scale that corresponded to Eq. 4.2 as shown in Figure 4.30. The results show that  $E_{EO}$  increased with lowering initial alachlor concentrations.  $E_{EO}$  increased from 12.50 to 26.32 kWh/m<sup>3</sup>/order when alachlor concentrations increased from 2.5 to 19 ppm.

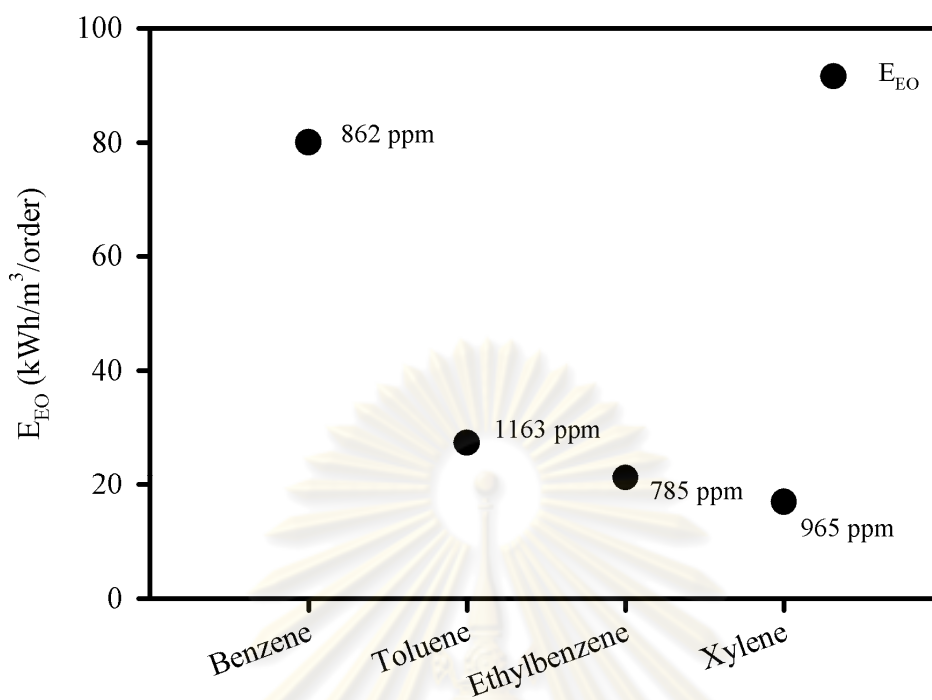


**Figure 4.30** Involved current under different chemicals.

$E_{EO}$  has been not widely reported. Only few can be tracked and tabulated in Table 4.13. This work reports the similar  $E_{EO}$  values used for decomposing BTEX in gas phase to that in the decomposition of BTEX in liquid solution. More reaction potential should be addressed based on the suspension and immobilization of the catalyst to the decomposition.

ศูนย์วิทยทรัพยากร  
จุฬาลงกรณ์มหาวิทยาลัย

**Table 4.13** Electrical energy per order reported for the current.

Catalysts	The electrical energy per order (kWh/m <sup>3</sup> /order)	Reference
TiO <sub>2</sub> on glass plates Liquid phase UV lamp (15W) C <sub>C.I. Acid Orange 10</sub> 30 ppm C <sub>C.I. Acid Orange 12</sub> 30 ppm C <sub>C.I. Acid Orange 8</sub> 30 ppm Catalyst loading: Six glass slides (5cm×28cm each) pH 3.0	70.67 (C.I. Acid Orange 10) 85.65 (C.I. Acid Orange 12) 98.04 (C.I. Acid Orange 8)	Khataee et al., 2009
Fe-TiO <sub>2</sub> Liquid phase Xenon lamp (58 mW/cm <sup>2</sup> ) (400 nm cut-off)+30 mM H <sub>2</sub> O <sub>2</sub> C <sub>Alachlor</sub> 2.5-19 ppm Catalyst loading 250 mg/L pH 3.0	12.50 – 26.32	Wantala et al., 2011
V-TiO <sub>2</sub> Gas phase Daylight lamp (58 W/m <sup>2</sup> ) C <sub>Benzene</sub> 862 ppm C <sub>Toluene</sub> 1163 ppm C <sub>Ethylbenzene</sub> 785 ppm C <sub><i>o</i>-Xylene</sub> 965 ppm Catalyst loading 0.33 mg/cm <sup>2</sup>	80 (Benzene) 27 (Toluene) 21 (Ethylbenzene) 17 ( <i>o</i> -Xylene)	This work

ศูนย์วิทยทรัพยากร  
จุฬาลงกรณ์มหาวิทยาลัย

## CHAPTER V

### CONCLUSION AND RECOMMENDATIONS

#### 5.1 Conclusion

In this study, transition metals (Fe, V, and W; abbreviated as TM) -doped TiO<sub>2</sub> catalysts were successfully synthesized using solvothermal method. It was immobilized onto flexible fiberglass cloth for the treatment of BTEX gases. Several techniques were used to understand the relevance of transition metals on physico-chemical properties of the obtained catalysts. The photocatalytic activities were investigated to determine a suitable catalyst for the degradation of BTEX contaminated in air and the selected catalyst was tested for its reliability. Important findings from this study can be summarized as follows;

The obtained catalysts exhibited mixed rutile-anatase phases. All dopants appeared to be well dispersed in the TiO<sub>2</sub> matrix and no new peaks associated with dopant oxides could be detected in the XRD spectra. The V and W dopants caused the XRD peaks of TiO<sub>2</sub> to shift slightly to higher angles, while the Fe dopant caused a small negative shift indicating that a certain fraction of TiO<sub>2</sub> lattices was deformed by introduction of the dopant atoms. This is in good agreement with the results from XANES measurements showing that the TM dopants caused the increase in pre-edge intensity suggesting for the less symmetrical octahedral environment around the Ti atoms. The refined pre-edge XANES spectra showed that A<sub>2</sub> corresponded to 1s-4p transitions for five-(TiO<sub>5</sub>) seem to be the main active species in the photocatalytic degradation of BTEX. All TM-doped samples increased visible absorption compared to that of the pure TiO<sub>2</sub> with the V-doped TiO<sub>2</sub> showing the highest increase followed by the W- and Fe-doped TiO<sub>2</sub>.

For photocatalytic degradation of gaseous toluene, V-doped TiO<sub>2</sub> showed the highest efficiency followed by W-, Fe- and the un-doped TiO<sub>2</sub> (69%, 54%, 48%, and 21% respectively). This was by the effect of the highest increase in the visible light absorption and also the smallest crystal size among the doped samples of the V-doped TiO<sub>2</sub>. Among BTEX single component, o-xylene displayed the highest removal efficiency followed by ethylbenzene, toluene, and benzene correlating with the trend

in their ionization potentials (increasing from o-xylene to benzene). The degradation of mixed BTEX using V-TiO<sub>2</sub> also showed the same trend in the degradation of BTEX single compound with the highest conversion of 15, 68, 81, and 84 % for 228±48 ppm of BTEX mixture compounds, respectively. The initial concentration and relative humidity negatively affected the photocatalytic activity; the higher initial concentration or the higher relative humidity, the lower BTEX removal efficiency. Our results show that V-doped TiO<sub>2</sub> immobilized on flexible fiberglass cloth is suitable for applications in photocatalytic treatment of gaseous BTEX under visible light.

## 5.2 Recommendations for future study

In this study, addition of dopants into TiO<sub>2</sub> matrix significantly increased its photocatalytic treatment of gaseous BTEX under visible light. Although positive results were obtained, more and in depth work must be conducted to answer questions that have arisen through the work.

- In order to understand the relationship between the catalytic behavior and the composition and structure of the catalyst clearly the study on chemical state and local atomic structure of catalyst before and after reaction test should be considered.
- From the reliability test, only three loops in the same conditions were carried out. It is recommended that in the last loop, longer reaction time (example is 100 hours or more) should be tested. Further than that, catalyst characterizations (examples are carbon content and high resolution microscope) of longer spent catalyst should be verified.
- Since the mechanistic studies on the photocatalytic oxidation of VOCs using TiO<sub>2</sub> have well established the intermediates and products of the reaction could be identified. Therefore, in depth study of intermediates should also be carried out.
- The optimization of all parameters should be evaluated.



- For further research in indoor air, catalyst in this configuration should be explored the test in any real situation;
  1. The effects of catalytic set up including the distance from the sources, and the intensity of bulb service, should be carried out.
  2. Humidity inside the room should be studied.
  3. Design of experiment could be one of ideas to optimize all parameters simultaneously.



ศูนย์วิทยทรัพยากร  
จุฬาลงกรณ์มหาวิทยาลัย

## REFERENCES

- Agency for Toxic Substances and Disease Registry. 2000. Toxicological profile for toluene [Online]. Available from: <http://www.atsdr.cdc.gov/ToxProfiles/tp>. [2010, October 8]
- Agency for Toxic Substances and Disease Registry. 2007. Toxicological profile for xylene [Online]. Available from: <http://www.atsdr.cdc.gov/ToxProfiles/tp>. [2010, October 8]
- Alberici, R. M., and Jardim, W. F. Photocatalytic destruction of VOCs in the gas phase using titanium dioxide. Applied Catalysis B: Environmental 14 (1997): 55-68.
- Anchez, B. S., Coronado, J. M., Candal, R., Portela, R., Tejedor, I., and Anderson, M. A. Preparation of TiO<sub>2</sub> coatings on PET monoliths for the photocatalytic elimination of trichloroethylene in the gas. Applied Catalysis B: Environmental 66 (2006): 295-301.
- Anpo, M., Dohshi, S., Kitano, M., Hu, Y., Takeuchi, M., and Matsuoke, M. The preparation and characterization of highly efficient titanium oxide-based photofunctional materials. Annual Review of Materials Science 35 (2005): 1-27.
- Ao, C. H., and Lee, S. C. Enhancement effect of TiO<sub>2</sub> immobilized on activated carbon filter for the photodegradation of pollutants at typical indoor air level. Applied Catalysis B: Environmental 44 (2003): 191-205.
- Ao, C. H., and Lee, S. C. Combination effect of activated carbon with TiO<sub>2</sub> for the photodegradation of binary pollutants at typical indoor air level. Journal of Photochemistry and Photobiology A: Chemistry 161 (2004): 131-140.
- Ao, C. H., and Lee, S. C. Indoor air purification by photocatalyst TiO<sub>2</sub> immobilized on an activated carbon filter installed in an air cleaner. Chemical Engineering Science 60 (2005): 103-109.

- Ao, C. H., Lee, S. C., Mak, C. L., and Chan, L. Y. Photodegradation of volatile organic compounds (VOCs) and NO for indoor air purification using TiO<sub>2</sub>: promotion versus inhibition effect of NO. Applied Catalysis B: Environmental 42 (2003): 119-129.
- Bahnemann, D., Photocatalytic water treatment: solar energy applications. Solar Energy 77 (2004): 445-459.
- Belver, C., López-Muñoz, M. J., Coronado, J. M., and Soria, J. Palladium enhanced resistance to deactivation of titanium dioxide during the photocatalytic oxidation of toluene vapors. Applied Catalysis B: Environmental 46 (2003): 497-509.
- Bosc, F., Edwards, D., Keller, N., Keller, V., and Ayrál, A. Mesoporous TiO<sub>2</sub>-based photocatalysts for UV and visible light gas-phase toluene degradation. Thin Solid Films 495 (2006): 272-279.
- Cai, T.J., Yue, M., Wang, X.W., Deng, Q. Zhenshan, P., Wenhui, Z. Preparation, characterization, and photocatalytic performance of NdPW<sub>12</sub>O<sub>40</sub>/TiO<sub>2</sub> composite catalyst. Chinese Journal of Catalysis 28 (2007):10-16.
- Carp, O., Huisman, C. L., and Reller, A. Photoinduced reactivity of titanium dioxide. Progress in Solid State Chemistry 32 (2004): 33-177.
- Chatterjee, D., and Dasgupta, S. Visible light induced photocatalytic decomposition of organic pollutants. Journal of Photochemistry and Photobiology C: Photochemistry Reviews 6 (2005): 186-205.
- Chen, X., and Mao, S. S. Titanium dioxide nanomaterials: synthesis, properties, modifications, and applications. Chemical Reviews 107 (2007): 2891-2959.
- Choi, J., Park, H., and Hoffmann, M. R. Effects of single metal-ion doping on the visible-light photoreactivity of TiO<sub>2</sub>. Journal of Physical Chemistry B 114 (2010): 783-392.
- Choi, W., Termin, A., and Hoffmann, M. R. The role of metal ion dopants in quantum-sized TiO<sub>2</sub>: correlation between photoreactivity and charge carrier recombination dynamics. Journal of Physical Chemistry 98 (1994): 13669-13679.

- Collins, C., Laternus, F., and Nepovim, A. Remediation of BTEX and trichloroethene - Current knowledge with special emphasis on phytoremediation. Environmental science and pollution research international 9 (2002): 86-94.
- De Groot, F. High-resolution X-ray emission and X-ray absorption spectroscopy Chemical Reviews 101 (2001): 1779-1808.
- Demeestere, K., Dewulf, J., Witte, B. D., Beeldens, A., and Langenhove, H. V. Heterogeneous photocatalytic removal of toluene from air on building materials enriched with TiO<sub>2</sub>. Building and Environment 43 (2008): 406-414.
- Dezhi, S., Sheng, C., Chung, J.S., Xiaodong, D., and Zhibin, Z. Photocatalytic degradation of toluene using a novel flow reactor with Fe-doped TiO<sub>2</sub> catalyst on porous nickel sheets. Photochemistry and Photobiology 81 (2005): 352-357.
- Dong, Y., Bai, Z., Liu, R., Wang, X., Yan, H., and Zhu, T. Heterogeneous decomposition of indoor ammonia in a photoreactor with TiO<sub>2</sub>-finished cotton fabrics. Environmental Technology 27 (2006): 705-714.
- Dong, Y., Bai, Z., Liu, R., and Zhu, T. Decomposition of indoor ammonia with TiO<sub>2</sub>-loaded cottonwoven fabrics prepared by different textile finishing methods. Atmospheric Environment 41 (2007): 3182-3192.
- Einaga, H., Futamura, S., and Ibusuki, T. Heterogeneous photocatalytic oxidation of benzene, toluene, cyclohexene and cyclohexane in humidified air: comparison of decomposition behaviour on photoirradiated TiO<sub>2</sub> catalyst. Applied Catalysis B: Environmental 38 (2002): 215-225.
- Farges, F., Brown, Jr. G. E., and Rehr, J. J. Ti K-edge XANES studies of Ti coordination and disorder in oxide compounds: Comparison between theory and experiment. Physical Review B 56 (1997):1809-1819.
- Fresno, F., Hernandez-Alonso, M. D., Tudela, D., Coronado, J. M., and Soria, J. Photocatalytic degradation of toluene over doped and coupled (Ti,M)O<sub>2</sub> (M = Sn or Zr) nanocrystalline oxides: Influence of the heteroatom distribution on deactivation. Applied Catalysis B: Environmental 84 (2008): 598-606.

- Fujishima, A., and Zhang, X. Titanium dioxide photocatalysis: Present situation and future approaches. Comptes Rendus Chimie 9 (2006): 750-760.
- Gaya, U. I., and Abdullah, A. H. Heterogeneous photocatalytic degradation of organic contaminants over titanium dioxide: A review of fundamentals, progress and problems. Journal of Photochemistry and Photobiology C: Photochemistry Reviews 9 (2008): 1-12.
- Geng, Q., Guo, Q., Cao, C., and Wang, H. Investigation into photocatalytic degradation of gaseous benzene in a circulated photocatalytic reactor (CPCR). Chemical Engineering Technology 31 (2008): 1023-1030.
- Gracia, F., Holgado, J. P., Caballero, A., and Gonzalez-Eliphe, A. R. Structural, optical, and photoelectrochemical properties of  $M^{n+}$  TiO<sub>2</sub> model thin film photocatalysts. Journal of Physical Chemistry B 108 (2004): 17466-17476.
- Herrmann, J. M. Heterogeneous photocatalysis: state of the art and present applications. Topics in Catalysis 34 (2005): DOI 10.1007/s11244-005-3788-2.
- Hoffmann, M. R., Martin, S. T., Choi, W., and Bahnemann, D. W. Environmental applications of semiconductor photocatalysis. Chemical Reviews 95 (1995): 69-96.
- Horikoshi, S., Watanabe, N., Onishi, H., Hidaka, H., and Serpone, N. Photodecomposition of a nonylphenol polyethoxylate surfactant in a cylindrical photoreactor with TiO<sub>2</sub> immobilized fibreglass cloth. Applied Catalysis B: Environmental 37 (2002): 117-129.
- Hsiung, T. L., Wang, H. P., and Lin, H. P. Chemical structure of photocatalytic active sites in nanosize TiO<sub>2</sub>. Journal of Physics and Chemistry of Solids 69 (2008): 383-385.
- Hsiung, T. L., Wang, H. P., and Wang, H. C. XANES studies of photocatalytic active species in nano TiO<sub>2</sub>-SiO<sub>2</sub>. Radiation Physics and Chemistry 75 (2006): 2042-2045.
- Huang, H. J., Wang, H. P., and Lee, J. F. Speciation of copper in ZSM-48 during NO reduction. Applied Catalysis B: Environmental 40 (2003): 111-118.



- Hurum, D. C. Agrios, A. G., and Gray, K. A. Explaining the enhanced photocatalytic activity of degussa P25 mixed-phase TiO<sub>2</sub> using EPR. Journal of Physical Chemistry B 107 (2003): 4545-4549.
- Jacoby, W. A., and others. Heterogeneous Photocatalysis for Control of Volatile Organic Compounds in Indoor Air. Journal of Air & Waste Management Association 46 (1996): 891-898.
- Jeong, J., Sekiguchi, K., Wookeun Lee, W., and Sakamoto, K. Photodegradation of gaseous volatile organic compounds (VOCs) using TiO<sub>2</sub> photoirradiated by an ozone-producing UV lamp: decomposition characteristics, identification of by-products and water-soluble organic intermediates. Journal of Photochemistry and Photobiology A: Chemistry 169 (2005): 279-287.
- Jing, D., and others. Efficient solar hydrogen production by photocatalytic water splitting: From fundamental study to pilot demonstration. International Journal of Hydrogen Energy (2010). In press.
- Jo, W.K., and Kim, J.T. Application of visible-light photocatalysis with nitrogen-doped or unmodified titanium dioxide for control of indoor-level volatile organic compounds. Journal of Hazardous Materials 164 (2009): 360-366.
- Jo, W. K., Park, J. H., and Chun, H. D. Photocatalytic destruction of VOCs for in-vehicle air cleaning. Journal of Photochemistry and Photobiology A: Chemistry 148 (2002): 109-19.
- Jothiramalingam, R., and Wang, M. K. Synthesis, characterization and photocatalytic activity of porous manganese oxide doped titania for toluene decomposition. Journal of Hazardous Materials 147 (2007): 562-569.
- Karakitsou, K. E., and Verykios, X. E. Effects of altrivalent cation doping of TiO<sub>2</sub> on its performance as a photocatalyst for water cleavage. Journal of Physical Chemistry 97 (1993): 1184-1189.

- Khataee, A.R., Pons, M.N., and Zahraa, O. Photocatalytic degradation of three azo dyes using immobilized TiO<sub>2</sub> nanoparticles on glass plates activated by UV light irradiation: Influence of dye molecular structure. Journal of Hazardous Materials 168 (2009): 451-457.
- Khemthong, P., Klysubun, W., Prayoonpokarach, S., and Wittayakun, J. Reducibility of cobalt species impregnated on NaY and HY zeolites. Materials Chemistry and Physics 121 (2010): 131-137.
- Kim, S. B., and Hong, S. C. Kinetic study for photocatalytic degradation of volatile organic compounds in air using thin film TiO<sub>2</sub> photocatalyst. Applied Catalysis B: Environmental 35 (2002): 305-315.
- Kim, S. B., Lee, J. Y., Jang, H. T., Cha, W. S., and Hong, S. C. Enhanced photocatalytic activity of TiO<sub>2</sub> by metal doping for degradation of VOCs in air. Journal of Industrial and Engineering Chemistry 9 (2003): 440-446.
- Klysubun, W., and others. Commission and performance of x-ray absorption beamline at the Siam photon Laboratory. Nuclear Instruments and Methods in Physics Research Section A 582 (2007): 87-89.
- Kuo, H. P., Wu, C. T., and Hsu, R. C. Continuous reduction of toluene vapours from the contaminated gas stream in a fluidised bed photoreactor. Powder Technology 195 (2009): 50-56.
- Ku, Y., Ma, C., and Shen, Y. Decomposition of gaseous trichloroethylene in a photoreactor with TiO<sub>2</sub>-coated nonwoven fiber textile. Applied Catalysis B: Environmental 34 (2001): 181-190.
- Lee, B. I., Kaewgun, S., Kim, W., Choi, W., Lee, J. S., and Kim, E. Visible light photocatalytic properties of polymorphic brookite titania. Journal of Renewable Sustainable Energy 1 (2009): 23101-23107.
- Lee, K., Lee, N. H., Shin, S. H., Lee, H. G., and Kim, S. J. Hydrothermal synthesis and photocatalytic characterizations of transition metals doped nano TiO<sub>2</sub> sols. Materials Science and Engineering B 129 (2006): 109-115.

- Li, F.B., and Li, X.Z. The enhancement of photodegradation efficiency using Pt–TiO<sub>2</sub> catalyst. Chemosphere 48 (2002): 1103-1111.
- Li, S., Chen, S., Zhua, L., Chen, X., Yao, C., and Shen, X. Concentrations and risk assessment of selected monoaromatic hydrocarbons in buses and bus stations of Hangzhou, China. Science of the Total Environment 407 (2009): 2004-2011.
- Luca, V., Djajanti, S., and Howe, R. F. Structural and electronic properties of sol gel titanium oxides studied by X-ray absorption spectroscopy. Journal of Physical Chemistry B 102 (1998): 10650-10657.
- Maira, A. J., and others. Gas-phase photo-oxidation of toluene using nanometersize TiO<sub>2</sub> catalyst. Applied Catalysis B: Environmental 29 (2001): 327-336.
- Martra, G., and others. The role of H<sub>2</sub>O in the photocatalytic oxidation of toluene in vapour phase on anatase TiO<sub>2</sub> catalyst – A FTIR study. Catalysis Today 53 (1999): 695-702.
- Misook, K. Synthesis of Al, Bi, and Fe-Ti binary metal oxide nanometer-sized particles using a solvothermal method and their super-hydrophilicities. Journal of Industrial and Engineering Chemistry 13 (2007): 143-152.
- Mo, J., Zhang, Y., Xu, Q., Lamson, J. J., and Zhao, R. Photocatalytic purification of volatile organic compounds in indoor air: A literature review. Atmospheric Environment 43 (2009): 2229-2246.
- Mo, S. D., and Ching, W. Y. Electronic and optical properties of three phases of titanium dioxide: Rutile, anatase, and brookite. Physical Review B 51 (1995): 13023–13032.
- Nagaveni, K., Hegde, M. S., and Madras, G. Structure and photocatalytic activity of Ti<sub>1-x</sub>M<sub>x</sub>O<sub>2±δ</sub> (M = W, V, Ce, Zr, Fe, and Cu) synthesized by solution combustion method Journal of Physical Chemistry B 108 (2004): 20204-20212.
- National Institute of Standards and Technology. 2010. Chemistry WebBook [Online]. Available from: <http://webbook.nist.gov/chemistry/>. [2011, January 12]
- Niskanen, A., Arstila, K., Leskelä, M., and Ritala, M. Radical Enhanced atomic layer deposition of titanium dioxide. Chemical Vapor Deposition 13 (2007): 152-157.

- Obee, T. N., and Brown, R. T. TiO<sub>2</sub> Photocatalysis for indoor air applications: effect of humidity and trace contaminant levels on the oxidation rates of formaldehyde, toluene, and 1,3-butadiene. Environment Science Technology 29 (1995): 1223-1231.
- Obee, T. N., and Hay, S. O. Effects of moisture and temperature on the photooxidation of ethylene on titania. Environmental Science & Technology 31 (1997): 2034-2038.
- Ohno, T., Akiyoshi, M., Umabayashi, T., Asai, K., Mitsui, T., and Matsumura, M. Preparation of S-doped TiO<sub>2</sub> photocatalysts and their photocatalytic activities under visible light. Applied Catalysis A: General 265 (2004): 115-121.
- Ohtani, B., Prieto-Mahaney, O. O., and Abe, D. L. R. What is Degussa (Evonik) P25? Crystalline composition analysis, reconstruction from isolated pure particles and photocatalytic activity test. Journal of Photochemistry and Photobiology A: Chemistry 216 (2010): 179-182.
- Paola, A. D., Ikeda, S., Marci, G., Ohtani, B., and Palmisano, L. Transition metal doped TiO<sub>2</sub>: physical properties and photocatalyst behaviour. International Journal of Photoenergy 3 (2001): 171-176.
- Patterson, A. L. The Scherrer Formula for X-Ray Particle Size Determination. Physical Review 56 (1939): 978-982.
- Pichat, P. Some views about indoor air photocatalytic treatment using TiO<sub>2</sub>: Conceptualization of humidity effects, active oxygen species, problem of C<sub>1</sub>-C<sub>3</sub> carbonyl pollutants. Applied Catalysis B: Environmental 99 (2010): 428-434.
- Pichat, P., Disdier, J., Hong-Van, C., Goutailler, G., and Gaysse, C. Purification/deodorization of indoor air and gaseous effluents by TiO<sub>2</sub> photocatalysis. Catalysis Today 63 (2000): 363-369.
- Ramirez, A.M., Demeestere, K., Belie, N.D., Mantyla, T., and c, Levanen, E. Titanium dioxide coated cementitious materials for air purifying purposes: Preparation, characterization and toluene removal potential. Building and Environment 45 (2010): 832-838.

- Rao, G. R., and Sahu, H. R. XRD and UV-Vis diffuse reflectance analysis of CeO<sub>2</sub>-ZrO<sub>2</sub> solid solutions synthesized by combustion method. Proceedings of the Indian Academy of Sciences: Chemical Science 113 (2001): 651-658.
- Ravel, B., and Newville, M. ATHENA, ARTEMIS, HEPHAESTUS: data analysis for X-ray absorption spectroscopy using IFEFFIT. Journal of Synchrotron Radiation 12 (2005): 537-541.
- Ruiz-Lopez, M. F., and Munoz-Paez, A. A theoretical study of the XANES spectra of rutile and anatase Journal of Physics: Condensed Matter 3 (1991): 8981-8990.
- Shannon, R. D. Revised effective ionic radii and systematic studies of interatomic distances in halides and chalcogenides. Acta Crystallographica Section A 32 (1976): 751-767.
- Sleiman, M., Conchon, P., Ferronato, C., and Chovelon, J. M. Photocatalytic oxidation of toluene at indoor air levels (ppbv): Towards a better assessment of conversion, reaction intermediates and mineralization. Applied Catalysis B: Environmental 86 (2009): 159-165.
- Soriano, L., Fuentes, G. G., Quiros, C., Trigo, J. F., and Sanz, J. M. Crystal-field effects at the TiO<sub>2</sub>-SiO<sub>2</sub> interfaces as observed by X-ray absorption spectroscopy. Langmuir 16 (2000): 7066-7069.
- Strini, A., Cassese, S., and Schiavi, L. Measurement of benzene, toluene, ethylbenzene and o-xylene gas phase photodegradation by titanium dioxide dispersed in cementitious materials using a mixed flow reactor. Applied Catalysis B: Environmental 61 (2005): 90-97.
- Tseng, H. H., Wei, M. C., Hsiung, S. F., and Chiou, C. W. Degradation of xylene vapor over Ni-doped TiO<sub>2</sub> photocatalysts prepared by polyol-mediated synthesis. Chemical Engineering Journal 150 (2009): 160-167.
- Wang, C.Y., Bottcher, C., Bahnemann, D.W., and Dohrmann, J. K. A. Comparative study of nanometer sized Fe(III)-doped TiO<sub>2</sub> photocatalysts: Synthesis, characterization and activity. Journal of Materials Chemistry 13 (2003): 2322-2329.



- Wang, K. H., Tsai, H. H., and Hsieh, Y. H. The kinetics of photocatalytic degradation of trichloroethylene in gas phase over TiO<sub>2</sub> supported on glass bead. Applied Catalysis B: Environmental 17 (1998): 313-320.
- Wang, W., and Ku, Y. Photocatalytic degradation of gaseous benzene in air streams by using an optical fiber photoreactor. Journal of Photochemistry and Photobiology A: Chemistry 159 (2003): 47-59.
- Wang, X. H., and others. T. Pyrogenic iron(III)-doped TiO<sub>2</sub> nanopowders synthesized in RF thermal plasma: phase formation, defect structure, band gap, and magnetic properties. Journal of the American Chemical Society 127 (2005): 10982-10990.
- Wantala, K., Khemthong, P., Wittayaun, J., and Grisdanurak, N. Visible light-irradiated degradation of alachlor on Fe-TiO<sub>2</sub> with assistance of H<sub>2</sub>O<sub>2</sub>, Korean Journal of Chemical Engineering Accepted (2011-04-10).
- Wong, Y. C., Sin, D. W., and Yeung, L. L. Assessment of the air quality in indoor car parks. Indoor Built Environment 11 (2002): 134-145.
- Wu, Z. Y., Ouvrard, G., Gressier, P., and Natoli, C. R. Ti and O K edges for titanium oxides by multiple scattering calculations: Comparison to XAS and EELS spectra. Physical Review B 55 (1997): 10382-10391.
- Yang, G. J., Li, C. J., and Wang, Y. Y. Phase formation of nano-TiO<sub>2</sub> particles during flame spraying with liquid feedstock. Journal of Thermal Spray Technology 14 (2005): 480-486.
- Yang, P., Lu, C., Hua, N., and Du, Y. Titanium dioxide nanoparticles Codoped with Fe<sup>3+</sup> and Eu<sup>3+</sup> ions for photocatalysis. Materials Letters 57 (2002): 794-801.
- Yu, K.P, and Lee, G.W.M. Decomposition of gas-phase toluene by the combination of ozone and photocatalytic oxidation process (TiO<sub>2</sub>/UV, TiO<sub>2</sub>/UV/O<sub>3</sub>, and UV/O<sub>3</sub>). Applied Catalysis B: Environmental 75 (2007): 29-38.
- Yu, Q. L., and Brouwers, H. J. H. Indoor air purification using heterogeneous photocatalytic oxidation. Part I: Experimental study. Applied Catalysis B: Environmental 92 (2009): 454-461.

- Zaleska, A. Doped-TiO<sub>2</sub>: A review. Recent Patents on Engineering 2 (2008): 157-164.
- Zhang, L., Eastmond, D. A., and Smith, M. T. The nature of chromosomal aberration detected in humans exposed to benzene. Critical Reviews in Toxicology 32 (2002): 1-42.
- Zhang, Y., Wei, S., Zhang, H., Liu, S., Nawaz, F., and Xiao, F. S. Nanoporous polymer monoliths as adsorptive supports for robust photocatalyst of Degussa P25. Journal of colloid and interface science 339 (2009): 434-438.
- Zhou, J., Takeuchi, M., Rayc, A. K., Anpo, M., and Zhao, X. S. Enhancement of photocatalytic activity of P25 TiO<sub>2</sub> by vanadium-ion implantation under visible light irradiation. Journal of Colloid and Interface Science 311 (2007): 497-501.
- Zuo, G. M., Cheng, Z. X., Chen, H., Li, G. W., and Miao, T. Study on photocatalytic degradation of several volatile organic compounds. Journal of Hazardous Materials B 128 (2006): 158-163.



ศูนย์วิทยทรัพยากร  
จุฬาลงกรณ์มหาวิทยาลัย



**APPENDICES**

ศูนย์วิทยทรัพยากร  
จุฬาลงกรณ์มหาวิทยาลัย

## APPENDIX A

### Calculation

#### A.1 Calculation to convert VOCs volume ( $\mu\text{l}$ ) to VOCs concentration (ppm)

The calculation used below is to convert the VOCs volume ( $\mu\text{l}$ ) to VOCs concentration (ppm). In dealing with gases, one part per million refers to one part by volume in 1 million volume units of the whole. Example shown is to convert 2  $\mu\text{l}$  toluene.

2  $\mu\text{l}$  toluene in 1000 ml air is 0.002/1000 ml (toluene in air)

The weight of toluene in 1000 ml air can be calculated from the value of toluene's density, which is 0.87 g/ml.

$$(0.002 \text{ ml}) \times (0.87 \text{ g/ml}) = 0.00174 \text{ g}$$

$$\text{or} = 0.00174 \text{ g toluene} / 1000 \text{ ml air}$$

1 mol of toluene is 92 g, therefore 0.00174 g is equivalent to  $1.89 \times 10^{-5}$  mol toluene.

At Standard Temperature Pressure (STP),

1 mol toluene gas has a volume of 24.79 L.

Therefore the volume of  $1.89 \times 10^{-5}$  mol toluene is:

$$24.79 \text{ Lmol}^{-1} \times 1.89 \times 10^{-5} \text{ mol} = 4.69 \times 10^{-4} \text{ L}$$

Therefore, the concentration of toluene in ppm is equivalent to:

$$4.69 \times 10^{-4} \times 10^6 = 469 \text{ ppm}$$

## A.2 Calculation of reaction rate

The calculation used below is to calculate the reaction rate in ppm/g·s. Example shown is to calculate the reaction rate from inlet toluene concentration of 500 ppm, flow rate 100 ml/min, catalyst loading of 0.5 mg, and toluene concentration at steady state (outlet) of 100 ppm.

$$\text{reaction rate } -r_A = \frac{F_{Ao} \Delta x}{W}$$

where  $F_{Ao}$  molar feed flow rate  
 $\Delta x$  conversion difference  
 $W$  catalyst weight

Molar feed flow rate of 500 ppm and flow rate 100 ml/min is:

$$F_{Ao} = (500 \text{ ppm}) \times (100 \text{ ml/min}) = 50 \text{ ppm/min or } 50 \text{ ppm/60s}$$

Conversion difference of inlet concentration 500 ppm and outlet concentration 100 ppm is:

$$\text{Conversion} = ((500-100)/500) \times 100 = 80 \%$$

$$\text{Therefore, conversion difference; } \Delta x = 0.8$$

Reaction rate at catalyst loading of 0.5 mg or 0.005 g is:

$$\left( \frac{50 \text{ ppm}}{60 \text{ s}} \times 0.8 \right) / 0.005 \text{ g} = 133.33 \text{ ppm/g}\cdot\text{s}$$

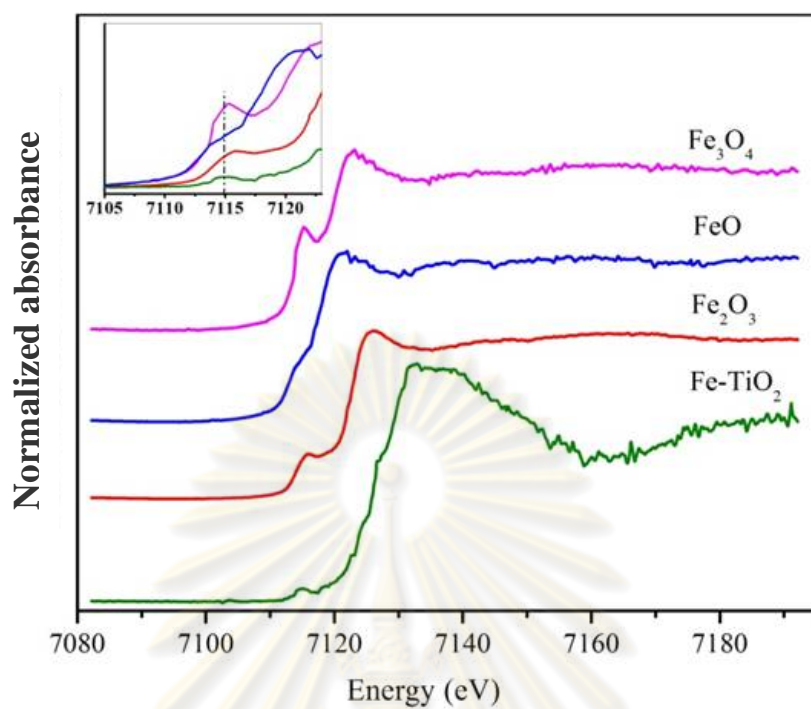


## APPENDIX B

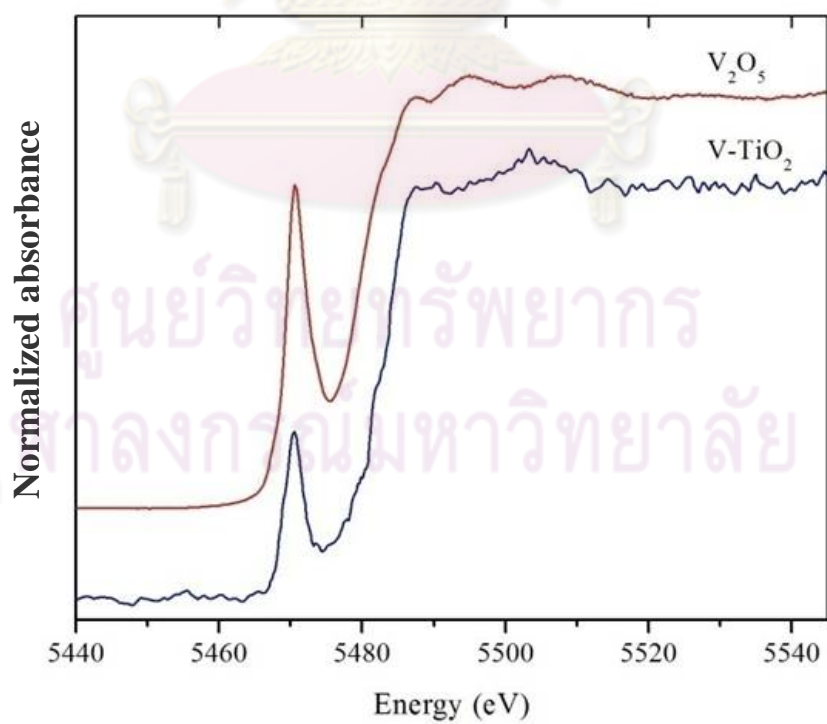
### K-edge XANES spectra

Figure B.1 shows the normalized XANES at Fe *K*-edge of Fe compounds. The comparison of sample with standard compound as FeO, Fe<sub>3</sub>O<sub>4</sub>, and Fe<sub>2</sub>O<sub>3</sub> provide a way to access their chemical environment of samples. FeO contains metal in regular octahedral site while Fe<sub>2</sub>O<sub>3</sub> and Fe<sub>3</sub>O<sub>4</sub>, contain the metal atoms in octahedral and both tetrahedral and octahedral sites. The XANES spectrum of Fe doped TiO<sub>2</sub> photocatalyst shows a weak pre-edge peak at 7117 eV between FeO and Fe<sub>2</sub>O<sub>3</sub> which correspond to Fe<sub>3</sub>O<sub>4</sub> compound. This pre-edge feature is assigned to the electronic transition from 1s to bound Fe 3d molecular orbital that is forbidden by dipole selection rules. Although this peak show the same position to that of the bulk Fe<sub>3</sub>O<sub>4</sub> but the intensity is different due to trace amount of metal doping indicate that Fe species were displayed a mixed valence of Fe<sup>2+</sup> and Fe<sup>3+</sup> species as confirmed by the visible white line peak at 7130 eV which is the contribution of 1s to 4p transition and referred to the mixed valence of Fe<sup>2+</sup> and Fe<sup>3+</sup> species. It is different from XANES spectra for V doped TiO<sub>2</sub> compared with V<sub>2</sub>O<sub>5</sub> as shown in Figure B.2. The pre-edge observed at 5465 eV is assigned to dipole forbidden electronic transitions between the 1s and 3d orbital due to the distortion of the VO<sub>5</sub> square pyramids permits partial overlapping and mixing of 3d states with the oxygen and vanadium p states. Based on this, it has been indicated that vanadium sites show significant V<sup>5+</sup> species.

ศูนย์วิจัยทรัพยากร  
จุฬาลงกรณ์มหาวิทยาลัย



**Figure B.1** K-edge XANES spectra of Fe-TiO<sub>2</sub>.



**Figure B.2** K-edge XANES spectra of V-TiO<sub>2</sub>.

## APPENDIX C

### Experimental set up

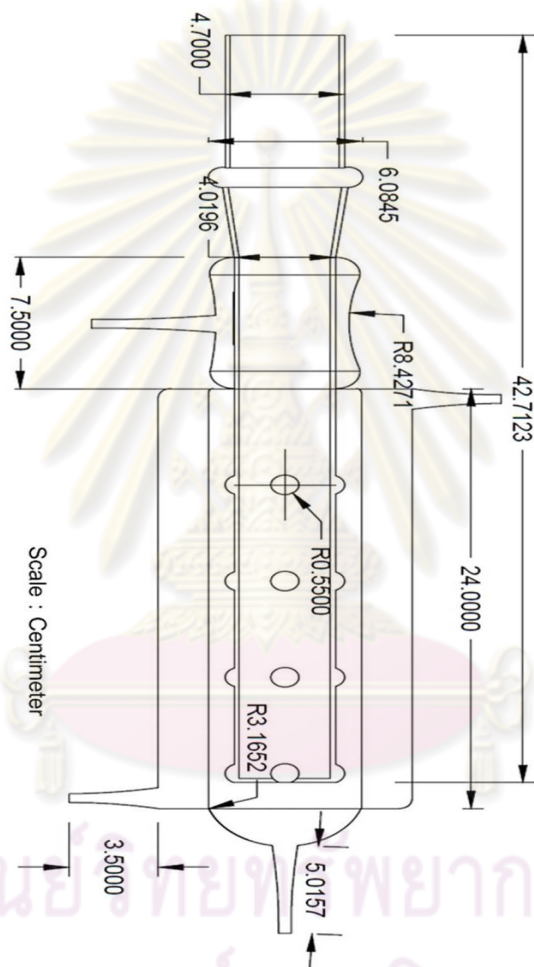


Figure C.1 Drawing of reactor vessel.

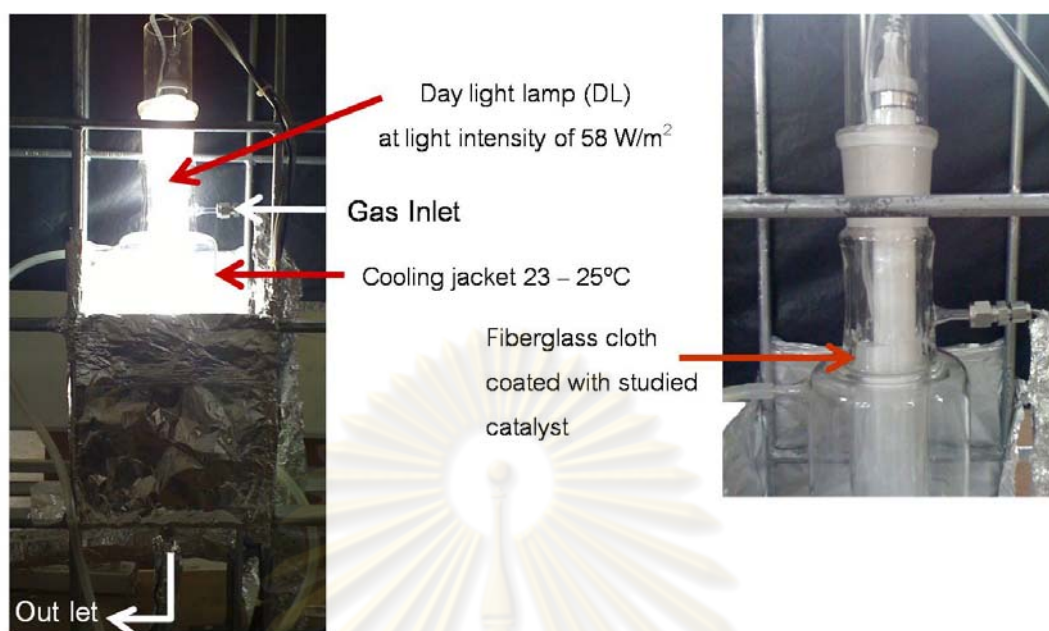


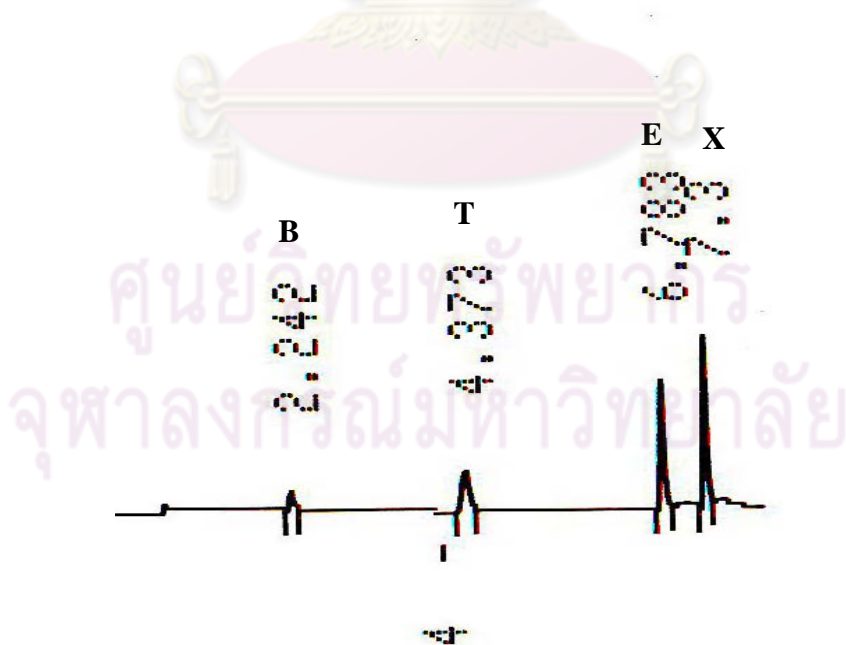
Figure C.2 Reactor set up in laboratory.



Figure C.3 Saturators for preparation of BTEX vapor.



**Figure C.4** Gas chromatograph (GC 14A, Shimadzu Co. Ltd.).



**Figure C.5** Chromatogram of mixed BTEX; B: benzene, T: toluene, E: ethylbenzene, X: *o*-xylene.



## APPENDIX D

### Experimental data

**Table D.1** Degradation of gaseous toluene for each catalyst-coated FGC after 120 minutes of visible light irradiation.

Catalyst	Test 1 <sup>st</sup>		Test 2 <sup>nd</sup>		Test 3 <sup>rd</sup>	
	Peak area	ppm	Peak area	ppm	Peak area	ppm
TiO <sub>2</sub> (P25)	498	819.07	489	804.27	502	825.65
Fe-TiO <sub>2</sub>	359	590.46	342	562.50	375	616.77
V-TiO <sub>2</sub>	250	411.18	204	335.52	218	358.55
W-TiO <sub>2</sub>	336	552.63	356	585.52	320	526.31

**Note:** 0.3±0.06 mg/cm<sup>2</sup> of catalyst, 1000-1200 ppm of toluene initial concentration and 30% RH.

**Table D.2** Degradation of each BTEX gas by the V-doped TiO<sub>2</sub> after 120 minutes of visible light irradiation.

Compound	Test 1 <sup>st</sup>		Test 2 <sup>nd</sup>		Test 3 <sup>rd</sup>	
	Peak area	ppm	Peak area	ppm	Peak area	ppm
Benzene	334	575.86	344	593.10	328	565.51
Toluene	200	328.94	218	358.55	245	402.96
Ethylbenzene	104	145.86	118	165.49	140	196.35
<i>o</i> -xylene	90	123.28	110	150.68	148	202.73

**Note:** 0.3±0.06 mg/cm<sup>2</sup> of catalyst, 30% RH and initial concentrations of 862±4, 1163±12, 785±6, and 965±5 ppm for the benzene, toluene, ethylbenzene, and xylene gases, respectively.

**Table D.3** Degradation of mixed BTEX gases by V-TiO<sub>2</sub>, TiO<sub>2</sub> (P25) and uncoated FGC.

Compound	Test 1 <sup>st</sup>		Test 2 <sup>nd</sup>		Test 3 <sup>rd</sup>	
	Peak area	ppm	Peak area	ppm	Peak area	ppm
<b>V-TiO<sub>2</sub></b>						
Benzene	89	153.44	88	151.72	90	155.17
Toluene	38	62.50	32	52.63	42	69.07
Ethylbenzene	30	42.07	48	67.32	31	43.47
<i>o</i> -xylene	31	42.46	36	49.31	24	32.87
<b>TiO<sub>2</sub> (P25)</b>						
Benzene	92	158.62	91	156.89	90	155.17
Toluene	99	162.82	97	159.53	98	161.18
Ethylbenzene	150	210.37	147	206.17	149	208.97
<i>o</i> -xylene	138	189.04	136	186.30	140	191.78
<b>Uncoated FGC</b>						
Benzene	107	184.48	106	182.75	106	182.75
Toluene	119	195.72	119	195.72	118	194.07
Ethylbenzene	191	267.88	193	270.68	194	272.08
<i>o</i> -xylene	180	246.57	177	242.46	179	245.20

**Note:** 0.3±0.06 mg/cm<sup>2</sup> of catalyst, 30% RH, initial concentrations of 228±47 ppm BTEX and irradiation time of 120 min.

**Table D.4** Degradation of mixed BTEX gases by V-TiO<sub>2</sub> under 30-40% RH.

Compound	Test 1 <sup>st</sup>		Test 2 <sup>nd</sup>		Test 3 <sup>rd</sup>	
	Peak area	ppm	Peak area	ppm	Peak area	ppm
<b>Low concentration (228±47 ppm)</b>						
Benzene	89	153.44	88	151.72	90	155.17
Toluene	38	62.50	32	52.63	42	69.07
Ethylbenzene	30	42.07	48	67.32	31	43.47
<i>o</i> -xylene	31	42.46	36	49.31	24	32.87
<b>High concentration (644±39 ppm)</b>						
Benzene	319	550.00	326	562.06	322	555.17
Toluene	190	312.50	202	332.23	177	291.11
Ethylbenzene	204	286.11	185	259.46	222	311.36
<i>o</i> -xylene	159	217.80	180	246.57	145	198.63

**Note:** 0.3±0.06 mg/cm<sup>2</sup> of catalyst and irradiation time of 120 min.

ศูนย์วิทยทรัพยากร  
จุฬาลงกรณ์มหาวิทยาลัย

**Table D.5** Degradation of mixed BTEX gases by V-TiO<sub>2</sub> under 70-80% RH.

Compound	Test 1 <sup>st</sup>		Test 2 <sup>nd</sup>		Test 3 <sup>rd</sup>	
	Peak area	ppm	Peak area	ppm	Peak area	ppm
<b>Low concentration (228±47 ppm)</b>						
Benzene	98	168.96	100	172.41	95	163.79
Toluene	101	166.11	94	154.60	104	171.05
Ethylbenzene	155	217.39	167	234.22	164	230.01
<i>o</i> -xylene	153	209.58	149	204.10	145	198.63
<b>High concentration (644±39 ppm)</b>						
Benzene	336	579.31	340	586.20	335	577.58
Toluene	353	580.59	349	574.01	334	549.34
Ethylbenzene	404	566.61	365	511.92	385	539.97
<i>o</i> -xylene	378	517.80	368	504.10	373	510.95

**Note:** 0.3±0.06 mg/cm<sup>2</sup> of catalyst and irradiation time of 120 min.

ศูนย์วิทยทรัพยากร  
จุฬาลงกรณ์มหาวิทยาลัย

## BIOGRAPHY

Laksana Laokiat is originally Thai. In 1990, she obtained her Bachelor degree in Nursing Science from Khon-Kaen University, Thailand. Four years later, she graduated Master of Science (Public Health) in Industrial Hygiene Program from Mahidol University, Thailand. After that she started working as a lecturer at the Department of Health Science (Faculty of Public Health in 2005), Faculty of Science, Thammasat University, Thailand. In 2000, she was promoted to an assistant professor. She has a lot of experiences related to occupational health impact assessment and pollution prevention. She is particularly interested in researching about air pollution both indoor and outdoor environment.



ศูนย์วิทยทรัพยากร  
จุฬาลงกรณ์มหาวิทยาลัย